Title
Far-field Superresolution Detection of Plasmonic Near-fields

Author
Boutelle, Robert Charles

Publication Date
2017

UNIVERSITY OF CALIFORNIA

Los Angeles

Far-Field Superresolution Detection of Plasmonic Nearfields

A dissertation submitted in partial satisfaction of the
requirements for the degree Doctor of Philosophy
in Chemistry

by

Robert Charles Boutelle

2017

ABSTRACT OF THE DISSERTATION

Far-Field Superresolution Detection of Plasmonic Near-Fields

by

Robert Charles Boutelle

Doctor of Philosophy in Chemistry

University of California, Los Angeles, 2017

Professor Daniel Neuhauser, Chair

Surface plasmons, the coupling of photons to charges at metal interfaces, are widely used to improve efficiency of sensing, energy transfer, and catalysis. There has been much effort to optimize plasmonic systems and exploit their field enhancement property. However, the system structure, resonance frequencies, and field enhancement are all coupled, making characterization difficult. While Maxwell finite-domain time-difference (FDTD) simulations can handle ideal systems, measurement and characterization of realistic (imperfect) experimental systems is desired.

Recently, we developed a novel single molecule superresolution method to characterize plasmonic nanostructures. We use the field strength sensitivity of stochastic blinking in quantum dots (QDs) as an indirect measurement of the local field strength, allowing measurement of the localized plasmonic near-field with a far-field reporter. Using traditional confocal excitation with a wide field capture EMCCD camera, in conjunction with Maxwell FDTD simulations, metallic nanostructures were mapped out with high spatial and local field intensity precision. Our approach offers advantages such as low-cost, high-throughput, and superresolved mapping of localized plasmonic fields.

The dissertation of Robert Charles Boutelle is approved.

Diana Huffaker

Shimon Weiss

Daniel Neuhauser, Committee Chair

University of California, Los Angeles

2017

LIST OF FIGURES

Curriculum Vitae

Robert C. Boutelle

GOALS: To broaden my skillset and knowledgebase and apply myself in a postdoc/professorship that encourages self-motivated projects and finding scientific solutions to engineering problems.

EDUCATION

2011 - 2017 **University of California, Los Angeles – Los Angeles, CA**
PhD Candidate, Chemistry
Advisor: Daniel Neuhauser and Shimon Weiss
Thesis: Far-field Superresolution Detection of Plasmonic Near-fields.

2007 - 2011 **Wesleyan University – Middletown, CT**
Bachelor of Arts, Chemistry with High Honors

ACADEMIC AWARDS

Physical Division PhD Thesis Award: to a graduate student who illustrates outstanding and creative research during his or her PhD career (2017)

George Gregory Research Award: to an outstanding graduate student in the department who shows impactful and creative research (2016)

National Science Foundation (NSF) Fellowship Honorary Mention (2012)

Bradley Prize: to the senior who excels in chemistry and particularly in special original work (2011)

Scholarship from ACS Physical Division Workshop for Undergraduate Students: to attend the August 2010 Boston ACS meeting and present a poster (2010)

Hughes Scholarship for Research (2010)

RESEARCH EXPERIENCE

Sept 2011 - Present **University of California, Los Angeles – Los Angeles, CA**
Department of Chemistry and Biochemistry
Theoretical Chemistry Division: Daniel Neuhauser
Computationally modeled plasmonic and emitter dipole coupling to both help better understand experimental results and help deconvolve superresolved images. Developed theory for near-field intensity and sensitivity in stochastic blinking of quantum dots.

Sept 2011 - Present **Physical Chemistry Division: Shimon Weiss**
Established a new technique for measuring plasmonics fields (and fields maps) on the nanoscale, using far-field detection. Experimentally showed near-field intensity sensitivity in stochastic blinking of quantum dots. This new method is invariant to the major problems that other methods have for molecules near a metal surface, such as enhancement, quenching, and point spread function distortion in close proximity to a metallic surface. Additionally, this technique can be superresolved using Superresolution Optical Fluctuation Imaging (SOFI).

Jun 2014 - Oct 2014 **Hughes Research Lab – Malibu, CA**
IR Nanomaterial Research
Sensors & Materials Division: Adam Gross
Fabricated and tested key technical elements of a scalable, solution processed, quantum dot based negative luminescence device. My role was to synthesize and measure semiconductor quantum dot nanoparticles with bandgaps in midwave infrared and longwave infrared. Photoluminescence and photoconductivity measurements were used to determine efficacy of synthesized quantum dots in a negative luminescence device.

Oct 2009 - May 2011 **Wesleyan University – Middletown, CT**
Department of Chemistry: Brian H. Northrop Lab
Computationally and spectroscopically investigated cycloadditions involving furan and maleimide derivatives to (i) better understand the reactivity of substituted analogues and (ii) optimize their dynamic behavior for use in the synthesis of new organic materials.

PUBLICATIONS

“Far-field Superresolution Detection of Plamonic Near-fields,” **R. C. Boutelle**, D. Neuhauser, S. Weiss, *ACS Nano 10* (8), 7955-7962 (2016)

“Photon-HDF5: An Open File Format for Timestamp-Based Single-Molecule Fluorescence Experiments.” A. Ingargiola, T. Laurence, **R. C. Boutelle**, S Weiss, *Biophysical Journal* 110.1: 26-33 (2016)

“Nanodentures and mechanical electrodynamics: 3D relative orientation of plasmonic nanoarches from absorption spectra,” **R. C. Boutelle**, Y. Gao, C. A. Arntsen and D. Neuhauser, *J. Phys. Chem. C*, 117, 9381-9385 (2013)

“Substituent Effects on the Reversibility of Furan-Maleimide Cycloadditions” **R. C. Boutelle**, B. H. Northrop *J. Org. Chem. 76*, 7994-8002 (2011)

PRESENTATIONS

Apr 2017 **ACS Physical Chemistry Oral Presentation**
“Far-Field Superresolution Detection of Plasmonic Near-fields.” **Robert C. Boutelle**, Daniel Neuhauser, Shimon Weiss. PHYS: Plasmonic Nanomaterials: From Physical Chemistry Fundamentals to Societal Impacts. Divisadero - Parc 55 in San Francisco, CA

Mar 2016 **ACS Physical Chemistry Oral Presentation**
“Far-Field Superresolution Detection of Plasmonic Near-fields.” **Robert C. Boutelle**, Daniel Neuhauser, Shimon Weiss. PHYS: Physical Principles in Functional Nanoscience: Symposium in honor of Mostafa A. El-Sayed. San Diego Convention Center in San Diego, CA

Mar 2016 **BPS Poster Presentation**
“Photon-HDF5: An Open File Format for Timestamp-Based Single-Molecule Fluorescence Data.” Antonio Ingargiola, Ted Laurence, **Robert C. Boutelle**, Shimon Weiss. Biophysical Society Poster Session. Staples Center in Los Angeles, CA

Aug 2010 **ACS Physical Chemistry Poster Session**
“Computational and Spectroscopic Investigations of Reversible Furan-Maleimide Cycloadditions: Parent Reaction and Derivatized Analogues.” **Robert C. Boutelle**, Brian H. Northrop. PHYS Poster Session. Boston Convention Center in Boston, MA

Aug 2009 **Hughes Poster Presentation**
“Computational and Spectroscopic Investigations of Reversible Furan-Maleimide Cycloadditions: Parent Reaction and Derivatized Analogues.” **Robert C. Boutelle**, Brian H. Northrop. Wesleyan University in Middletown, CT

Aug 2008 **Scientific Computing and Informatics Center Poster Presentation**
“A New Angle on Density Functional Theory” **Robert C. Boutelle**, Ericka Barnes, George A. Petersson. Wesleyan University in Middletown, CT

CHAPTER I: Introduction

1.1. Background and Motivation

Plasmonics is a growing field with a lot of realized and potential impacts in chemistry. This is due to the enormous local-field enhancements near metal structures, which affect biological sensors [1-4], dyes' fluorescence [5-7], and tip-enhanced Raman spectroscopy [8-11]. Further, waveguides with sub-diffraction light-bending properties have been devised [12-14], and coupling of plasmonic circuits to optical circuits is a promising avenue [15-17]. There has been much effort to optimize plasmonic systems and exploit their field enhancement property. However, the system structure, resonance frequencies, and field enhancement, are all coupled – making characterization difficult.

Many of the applications of plasmonics would benefit from knowledge of the near-field distribution around the plasmonic device. This information is normally only accessible via finite difference time domain (FDTD) simulations, which solve Maxwell's equations for a modeled optical structure, or through expensive and complex electron microscopy techniques [19]. It is experimentally complex to get a physical confirmation of the simulations, as advanced fabrication methods have driven down the size of structures to the nanoscale regime, which in turn produce extremely small field structures, which cannot be resolved by conventional optical microscopy. Additionally, what is fabricated or synthesized experimentally often times does not match our ideal modeled structures. This leads to long iterations of modeling and fabrication trying to optimize plasmonic systems.

With the development of plasmonics-based devices and circuits, there is a growing need for methods for efficient detecting and characterizing plasmonic effects. The common approach for measuring plasmonic fields is near field scanning optical microscope (NSOM) [25-31], which is slow due to a feedback loop. Alternates, such as two-photon luminescence imaging [34], electron energy loss spectroscopy [35, 36], photoemission electron microscopy [37], cathode-luminescence spectroscopy [38], and bleach-image plasmon propagation (BlIPP) [39], are still diffraction limited, costly, and have low throughput.

Single-molecule superresolution methods, such as PALM and STORM, have better resolution than conventional optical microscopy.[40-42] Dye emission intensity had been previously used in an attempt to characterize the plasmonic near-field of metallic structures and mapped using far-field superresolution techniques. The simplest superresolution approach for measuring plasmonic fields uses a polymer layer doped with fluorescent molecules close to a planar metal layer.[24, 43, 44] Such emitters could be localized at high precision and their emission intensity should be measured (assuming that it is proportional to the plasmonic excitation field). However, characterization of plasmonic near-fields using an emitter's fluorescent intensity has many complications. Fluorescence enhancement and quenching effects cause the fluorescence intensity to vary non-monotonically as function of the probe distance less than 30 nm from the metal.[24, 45] Additionally, the point-spread function (PSF) of an emitter placed within 100 nm of a metallic surface is distorted due to strong electromagnetic coupling of the emitter's dipole to the nearby metallic structure. The superposition of scattered light PSF from the metal surface and dipole emitter PSF causes an erroneous localization of the far-field PSF away from the true location of the probe.[20, 33, 46, 47] When within several nanometers of a metallic structure, a distance of particular interests for nanoparticle plasmonics, the underlying structure can completely distort an emitter's PSF to non-Gaussian shapes making localization difficult without knowing the underlying structure.[46] Lastly, the relation between excitation and emission is non-linear at strong fields due to saturation.

This thesis will explore methods to increase throughput of characterizing plasmonic systems computationally and experimentally. The availability of a combined simulation effort and wide-field imaging experiments naturally raises a speculative direction, whereby we can look at enhanced interactions, propagation, and control of plasmons in "dirty systems," such as circuits that are self-assembled bottom up and hence lack the *a priori* knowledge of their detailed structure. The thesis will take first steps in exploring the possibility of solving the inverse problem of mapping such *a priori* unknown circuits. Results obtained here will allow in the long term (beyond the scope of the work illustrated here) to eventually generate enough constraints for the solution of the inverse problem.

1.2. Thesis Overview

This thesis begins with an introduction to plasmonics in Chapter 2, covering surface plasmon polaritons and localized surface plasmon resonances to enable a better understanding of plasmonics and EM hotspots. Additionally, emitter dipole interaction with plasmonic surfaces will be introduced to outline difficulties for single molecule localization in plasmonics. Later chapters will illustrate methods to overcome single molecule localization difficulties. Chapter 3 covers a new method for efficiently calculating plasmonic near-fields for small systems. This method, dubbed Nearfield, will be applied to a highly asymmetric system to illustrate its efficiency and utility. Experimental methods for far-field superresolution detection of plasmonic near-fields are discussed in Chapter 4. An orthogonal approach using stochastic blinking in quantum dots will be used as a far-field reporter of plasmonic near-fields. This new method is invariant to the major problems that other methods have for molecules near a metal surface, such as enhancement, quenching, and point spread function distortion in close proximity to a metallic surface. Chapter 5 looks at using polarization and resonance modulation to back-calculate emitter positions without any *a priori* knowledge of emitter location, towards solving the inverse problem. Finally, in Chapter 6, high throughput analysis of plasmonic systems will be looked at using superresolution techniques, specifically Superresolution Optical Fluctuation Imaging (SOFI).

CHAPTER II: Plasmonics

2.1. Introduction to Plasmonics

Plasmonics is the study of the interaction between electromagnetic fields and free electrons in a metal. A plasma oscillation in a metal is a collective longitudinal excitation of the conduction electron gas. A plasmon is a quantum of plasma oscillation; free electrons in metals can be excited by passing an electron through a thin metallic film or by reflecting an electron off a metallic film. This is the principle Electron Energy-Loss Spectroscopy (EELS) uses to characterize plasmonic nanostructures [48] The reflected or transmitted electron will show an energy loss equal to integral multiples of the plasmon energy. However, the most common method of plasmon excitation is by coupling or reflecting a photon from a film. The charge of the electron couples with the electrostatic field fluctuations. These induced collective oscillations are called plasmons.

What makes plasmonics a powerful tool is its ability to preserve the properties of a photon, such as polarization, yet can be concentrated below the diffraction limit of light.[49] Many areas of optical physics and devices can benefit from such extreme light concentration and manipulation. In any dielectric structures, such as dielectric optical cavities, the wavevector components (k) must all be real in at least one region of space. Thus the available k values are bound by the relation $k_x^2 + k_y^2 + k_z^2 = k_0^2\epsilon$. By the property of Fourier transform, or uncertainty principle, this results in a minimal spatial bound of $(\lambda/2n)^3$, where λ is the wavelength of light and n is the refractive index. This is the diffraction limit. However, SPPs existing in metal structures are evanescent waves such that in all space regions at least one wavevector component is imaginary. For argument sake, we will define k_x is a metal layer located at x = constant. There is no bound to wavevector k, because $k_y^2 + k_z^2 - |k_x^2| = k_0^2\epsilon$ consequently there is no limit to the mode size reduction and thus light coupled to a plasmon mode can be confined below the diffraction limit.

In the visible region of light, the dielectric condition for plasmon excitation, negative real and small positive imaginary dielectric constant, is met by coinage metals such as gold, silver and more recently aluminum and copper, due to improved control over oxide formation.[50, 51] In the near IR, doped semiconductors such as aluminum-doped zinc oxide and tin-doped indium oxide have recently emerged as a new class of plasmonic materials, indicating the diversity of materials capable of supporting plasmons.[52-56] Plasmons are typically separated into two categories, localized surface plasmons and propagating surface plasmons (or SPP), based on the dimensions of the underlying structures (Figure 2.1.). When light interacts with these plasmon oscillations and are confined to the interface between a metal and dielectric, the photons and electron density oscillations form quasiparticales, which are known as Surface Plasmon Polaritons (SPP). Propagating plasmons are excited in materials with at least one dimension smaller than the wavelength of light and another larger than the wavelength of light (for example, a thin metal film or a micron-length nanowire), such that the electron density wave travels along the extended dimension of the structure over distances much longer than the

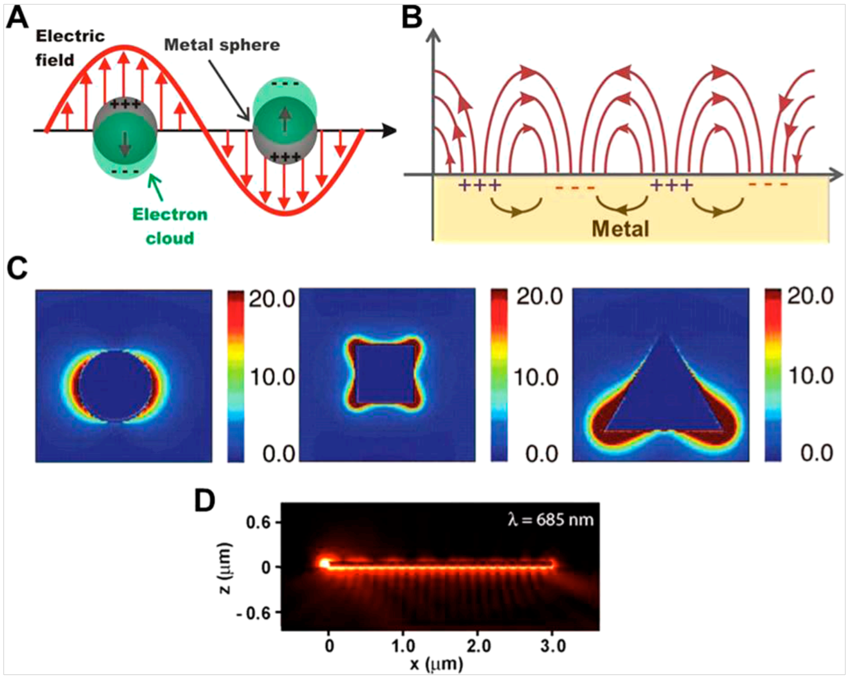

Figure 2.1. (A) Schematic of a localized surface plasmon (LSPR) showing the displacement and resulting response of the surface conduction electrons in response to an oscillating electric field. (B) Schematic of a surface plasmon polariton (SPP), illustrating propagation of a charge density wave down thin metal film. (C) Calculated electromagnetic near-field intensity distribution around plasmonic nanostructures of varying shapes (sphere, cube, and triangle). All structures filled the same volume with the left sphere having radius of 50nm.The color scale represents the intensity of the local electromagnetic field relative to the incident intensity. Adapted with permission from ref [22]. (D) Electric field distribution of a propagating plasmon along a nanowire at an interface. Adapted from ref [32].

wavelength of light (Figure 2.1.B). If we move from a continuous surface, like a metallic film, to a shaped material, such as a nanoparticle (NP), these SPPs can form standing waves much like that of ripples along the surface of a pond. These SPP standing waves are known as Localised Surface Plasmon Resonances (LSPR). Localized surface plasmons are excited on nanoparticles with dimensions smaller than the wavelength of the excitation light and can be thought of as standing electron density waves trapped near the surface of the nanoparticle (Figure 2.1.A). [22, 32, 57]. Both cases will be talked about in detail in the sections below. The concentration of electrons is tightly confined in regions near the nanostructure surface leading to highly localized enhanced electromagnetic fields (Figure 2.1.C and D).[32] The intensity of the enhanced electromagnetic fields can exceed $10^4 - 10^9$ of the incident field intensity, yet these regions of enhanced fields are confined to volumes much smaller than the diffraction limit of light, as shown in Figure 2.1.C and D.[32, 58-60]

2.2. Surface Plasmon Polaritons

Surface plasmon polaritons are electromagnetic excitations propagating at the interface between a dielectric and a conductor, evanescently confined in the perpendicular direction. These electromagnetic surface waves arise via the coupling of the electromagnetic fields to oscillations of the conductor's electron plasma. When trying to understand the nature and properties of SPPs it can be helpful to consider the dispersion relationship for a SPP propagating at the interface between a metal slab and a dielectric such as air, as shown in Figure 2.2. Full derivations can be found in a review texts [18]. The slabs are made up of a metal in the $z < 0$ region that is described via a dielectric function $\epsilon_1(\omega)$, where $Re[\epsilon_1] < 0$, which is a requirement of metallic properties and a dielectric slab in the $z > 0$ region with a positive real dielectric constant of ϵ_2.

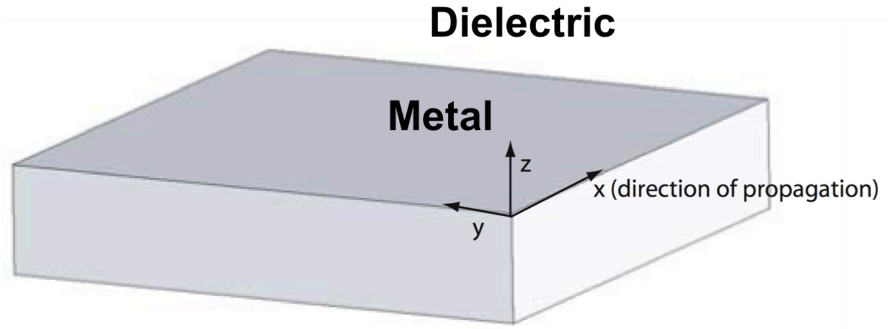

Figure 2.2. Schematic of a metal-dielectric interface for a SPP along the *x*-axis. Adapted with permission from ref. [18]

We start with the solution equations to the transverse magnetic (TM) mode for $z > 0$:

$$H_y(z) = A_2 e^{i\beta x} e^{-k_2 z}$$

$$E_x(z) = iA_2 \frac{1}{\omega\epsilon_0\epsilon_2} k_2 e^{i\beta x}\, e^{-k_2 z}$$

$$E_z(z) = -A_1 \frac{\beta}{\omega\epsilon_0\epsilon_2} e^{i\beta x}\, e^{-k_2 z}$$

for $z < 0$:

$$H_y(z) = A_1 e^{i\beta x} e^{k_1 z}$$

$$E_x(z) = -iA_1 \frac{1}{\omega\epsilon_0\epsilon_1} k_1 e^{i\beta x}\, e^{k_1 z}$$

$$E_z(z) = -A_1 \frac{\beta}{\omega\epsilon_0\epsilon_1} e^{i\beta x}\, e^{k_1 z}$$

Here, β is the propagation constant or the wave traveling in the x-direction. $k_i \equiv k_{z,i} (i = 1, 2)$ is the component of the wave vector perpendicular to the interface in the two media. Its reciprocal value, $\hat{z} = 1/|k_z|$, defines the evanescent decay length of the fields perpendicular to the interface, which quantifies the confinement of the wave. Continuity of H_y and $\epsilon_i E_z$ at the interface requires that $A_1 = A_2$ and

$$\frac{k_2}{k_1} = -\frac{\epsilon_2}{\epsilon_1}$$

Note that with our convention of the signs in the exponents, confinement to the surface demands $Re[\epsilon_1] < 0$ if $\epsilon_2 > 0$ – the surface waves exist only at the interfaces between materials with opposite signs of the real part of their dielectric permittivity, i.e. between a conductor and an insulator. The expression for H_y further has to fulfill the TM wave equation

$$\frac{\delta^2 H_y}{\delta z^2} + (k_0^2 \epsilon - \beta^2) H_y = 0 \quad \textbf{(2.1)}$$

yielding:

$$k_1^2 = \beta^2 - k_0^2 \epsilon_1 \quad \textbf{(2.2)}$$

$$k_2^2 = \beta^2 - k_0^2 \epsilon_2 \quad \textbf{(2.3)}$$

This leads us to the central result: the dispersion relation of SPPs propagation at the interface between the two half spaces (Figure 2.3.):

$$\beta = k_0 \sqrt{\frac{\epsilon_1 \epsilon_2}{\epsilon_1 + \epsilon_2}} \quad \textbf{(2.4)}$$

Only the TM wave is important which will be briefly shown below. Using the solved Tranverse Electric polarized modes for $z > 0$:

$$E_y(z) = A_2 e^{i\beta x} e^{-k_2 z} \quad \textbf{(2.5)}$$

$$H_x(z) = iA_2 \frac{1}{\omega \epsilon_0 \epsilon_2} k_2 e^{i\beta x} e^{-k_2 z} \quad \textbf{(2.6)}$$

$$H_z(z) = -A_1 \frac{\beta}{\omega \epsilon_0 \epsilon_2} e^{i\beta x} e^{-k_2 z} \quad \textbf{(2.7)}$$

for $z < 0$:

$$E_y(z) = A_1 e^{i\beta x} e^{k_1 z} \quad \textbf{(2.8)}$$

$$H_x(z) = -iA_1 \frac{1}{\omega \epsilon_0 \epsilon_1} k_1 e^{i\beta x} e^{k_1 z} \quad \textbf{(2.9)}$$

$$H_z(z) = -A_1 \frac{\beta}{\omega \epsilon_0 \epsilon_1} e^{i\beta x} e^{k_1 z} \quad \textbf{(2.10)}$$

Similar to TM, continuity of E_y and H_x at the interface leads to the condition

$$A_1(k_1 + k_2) = 0 \quad \textbf{(2.11)}$$

since confinement to the surface requires $Re[k_1] > 0$ and $Re[k_2] > 0$, this condition is only fulfilled if $A_1 = 0$, so that also $A_1 = A_2 = 0$. *Thus, no surface modes exist for TE polarization.*

Some additional properties of the surface charge interaction with the EM field are of significant importance. The field perpendicular to the interface decays exponentially with distance from the surface, leading to reduced mode volume size for the propagating wave when compared to its free space counterpart. This reduced mode volume concentrates the light, increasing the field density giving higher field strengths than illumination used. Once generated, these SPP loose energy into the metal via electron-electron scattering and phonon generation, giving the SPPs short propagation distances when compared to purely optical modes. This

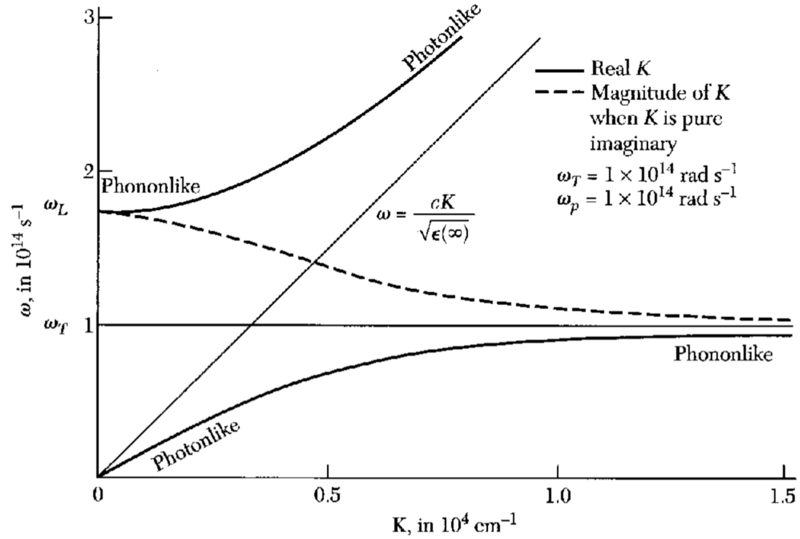

Figure 2.3. Coupled modes of photons and transverse optical phonons in an ionic crystal. The fine horizontal line represents oscillators of frequency ω_T in the absence of coupling to the electromagnetic field, and the fine line labeled $\omega = cK/\sqrt{\epsilon(\infty)}$ corresponds to electromagnetic waves in the crystal, but uncoupled to the lattice oscillator ω_T. The heavy lines are the dispersion relations in the presence of coupling between the lattice oscillators and the electromagnetic wave. One effect of the coupling is to create the frequency gap between ω_L (photon frequency) and ω_T: within this gap the wavevector is imaginary in magnitude given by the broken line in the figure. In the gap the wave attenuates as $\exp(-|K|x)$, and we see from the plot that the attenuation is much stronger near ω_T than near ω_L. The character of the branches varies with K; there is a region of mixed electric-mechanical aspects near the nominal crossover. This figure is adapted with permission from ref. [21].

engineering challenge is one of the difficulties faced in the miniaturization of optical components using plasmonics. The nature of SPPs means they are well suited to the applications of sub wavelength optics and light manipulation on small scales. The field enhancements due to mode compression also make them ideal for development of next-generation, low-power, all-optical switches and all-optically-tunable plasmonic devices. Such concepts have numerous applications ranging from standalone photonic components, optical sensors, and quantum computing.[61-63]

2.3. Localized Surface Plasmon Resonances

SPPs are propagating, dispersive electromagnetic waves coupled to the electron plasma of a conductor at a dielectric interface. Localized surface plasmons (LSPRs) on the other hand are non-propagating excitations of the conduction electrons of metallic nanostructures coupled to the electromagnetic field. The curved surface of the particle exerts an effective restoring force on the driven electrons, so that a resonance can arise, leading to field amplification both inside and in the near-field zone outside the particle. This resonance is called the localized surface plasmon or short localized plasmon resonance. Another consequence of the curved surface is that plasmon resonances can be excited by direct light illumination, in contrast to propagating SPPs, where the phase-matching techniques, such as Bragg diffraction grattings, must be employed.

LSPRs can massively change the optical properties that a material has in its bulk form. This change can be controlled via the shape and size of the structures fabricated. For example, gold is yellow in bulk, but it can appear red to violet when in a colloidal form, for gold nanoparticle sizes 5-90nm. These properties are the result of a resonant interaction between specific wavelengths of light with the nanostructures. To understand this resonant behavior, we

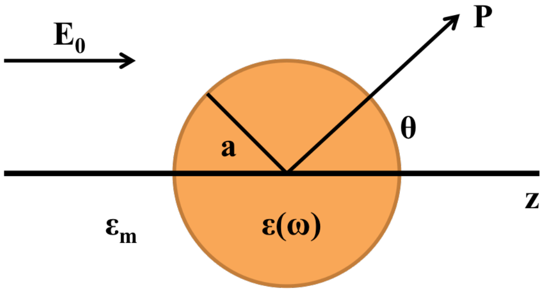

Figure 2.4: Sketch of a homogeneous sphere placed in an electrostatic field.

can look at a small sub-wavelength particle shown in Figure 2.4, located at the origin, subject to an electric field $\boldsymbol{E}$. For a sub-wavelength size sphere where $a \ll \lambda$ we can use a quasi-static approximation as, for a harmonically oscillating electric field, the phase over the small particle will be approximately constant. Therefore the static electric field $\boldsymbol{E} = E_0\hat{\boldsymbol{x}}$ will be used.

In the electrostatic approach, we are interested in a solution of the Laplace equation for the potential, $\nabla^2\Phi = 0$, from which we will be able to calculate the electric field $E = -\nabla\Phi$. The equations for the potential Φ inside and outside the sphere are derived in [64] and can be written as:

$$\Phi_{in} = -\frac{3\epsilon_m}{\epsilon + 2\epsilon_m} E_0 r\cos(\theta) \tag{2.12}$$

$$\Phi_{out} = -E_0 rcos(\theta) + \frac{\epsilon - \epsilon_m}{\epsilon + 2\epsilon_m} E_0 a^3 \frac{\cos(\theta)}{r^2} \tag{2.13}$$

By examining Φ_{out} (Equation 2.13), it is possible to see that it is made up of the electrostatic field applied at point P in the first term of the equation and the field produced by a dipole located at the origin in the center of the particle as the second term of the equation:

$$\Phi_{out} = \Phi_{Applied} + \Phi_{dipole} \tag{2.14}$$

Where the dipole potential can be written as:

$$\Phi_{dipole} = \frac{p}{4\pi\epsilon_0\epsilon_m}\frac{\cos(\theta)}{r^2} \quad \textbf{(2.15)}$$

where p is the dipole moment generated at the origin. By equating this dipole moment and the second term of Φ_{out} (Equation 2.13) then rearranging, it is found that the dipole moment for this system can be written as:

$$\boldsymbol{p} = 4\pi\epsilon_0\epsilon_m a^3 \frac{\epsilon - \epsilon_m}{\epsilon + 2\epsilon_m}\boldsymbol{E_0} \quad \textbf{(2.16)}$$

Plugging in equation 2.16 into 2.13 gets:

$$\Phi_{out} = -E_0 r\cos(\theta) + \frac{\boldsymbol{p}\cdot\boldsymbol{r}}{4\pi\epsilon_0\epsilon_m} \quad \textbf{(2.17)}$$

If we define polarizability α to be $\boldsymbol{p} = \epsilon_0\epsilon_m\alpha\boldsymbol{E_0}$, the equation 2.17 simplifies to:

$$\alpha = 4\pi a^3 \frac{\epsilon - \epsilon_m}{\epsilon + 2\epsilon_m} \quad \textbf{(2.18)}$$

Polarizability is a measure of how easily a field $\boldsymbol{E_0}$ induces a dipole moment inside the sphere. From equation 2.18, as the denominator approaches 0, α diverges. This is the Fröhlich criterion and means that a small change in field $\boldsymbol{E_0}$ can lead to a large induced dipole moment. This is resonance behaviour and at these resonant wavelengths the induced fields are very large.

As one can readily see from the derived equations, antenna size, geometry, and material composition can have a large effect on the behavior of a LSPR. This will be discussed in greater detail in section 2.5. This kind of optical response engineering has already found many applications, such as Surface-Enhanced Raman Scattering (SERS) spectroscopy [33]. LSPR use the sensitivity in peak shift due to environmental changes in biological and chemical sensing.

2.4. Introduction to FDTD Modeling of Plasmonic Systems

Finite-Difference Time-Domain method (FDTD) is the most widely used and most effective numerical method in the study of metamaterials. The method effectively is a Maxwell's equation solver. FDTD offers a simple yet straightforward way to model complex periodic structures. This section will give a brief overview of how FDTD methods model plasmonic systems and briefly describe its shortcomings.

As was said before, FDTD is a Maswell's equation solver. Specifically:

$$\frac{\delta \vec{B}}{\delta t} = -\nabla \times \vec{E} - \sigma^{*} \vec{H} \tag{2.19}$$

$$\frac{\delta \vec{D}}{\delta t} = -\nabla \times \vec{H} - \sigma \vec{E} \tag{2.20}$$

$$\nabla \cdot \vec{D} = 0 \tag{2.21}$$

$$\nabla \cdot \vec{B} = 0 \tag{2.22}$$

Where σ^{*} is equivalent magnetic loss, σ is electric conductivity, $\vec{E}$ is the electric field (or electric flux density), $\vec{H}$ is the magnetic field strength, $\vec{D}$ is the electric displacement field, and $\vec{B}$ is the magnetic field (or magnetic flux density) where:

$$\vec{D} = \epsilon \vec{E} = \epsilon_0 \epsilon_r \vec{E} \tag{2.23}$$

$$\vec{B} = \mu \vec{H} = \mu_0 \mu_r \vec{H} \tag{2.24}$$

When you solve these equations, you get:

$$\frac{\delta E_x}{\delta t} = -\frac{1}{\epsilon}\left[\frac{\delta H_z}{\delta y} - \frac{\delta H_y}{\delta z}\right] - \frac{\sigma}{\epsilon} E_x \tag{2.25}$$

$$\frac{\delta E_y}{\delta t} = -\frac{1}{\epsilon}\left[\frac{\delta H_x}{\delta y} - \frac{\delta H_z}{\delta z}\right] - \frac{\sigma}{\epsilon}E_y \tag{2.26}$$

$$\frac{\delta E_z}{\delta t} = -\frac{1}{\epsilon}\left[\frac{\delta H_y}{\delta y} - \frac{\delta H_x}{\delta z}\right] - \frac{\sigma}{\epsilon}E_z \tag{2.27}$$

Immediately a problem is seen. The electric fields are dependent on the magnetic fields and the magnetic fields are dependent on the magnetic fields in time. Luckily, we can solve these with Yee grids (Figure 2.5).[65] The Yee grids simultaneously deals with both electric and magnetic fields in time and space using the coupled form of Maxwell's curl equations, rather than by solving the wave equation for either the electric field (or the magnetic field alone). Yee's algorithm positions its $\vec{E}$ and $\vec{H}$ components at the centers of the grid lines and surfaces such that each $\vec{E}$ component is surrounded by four $\vec{H}$ components, and vice versa. This provides an elegant yet simple picture of three-dimensional space being filled by interlinked arrays of Faraday's law and Ampere's law contours. Utilizing Yee's spatial gridding scheme, the partial spatial derivatives can be solved using a leap-frog approach. For the electric part, and example equation becomes:

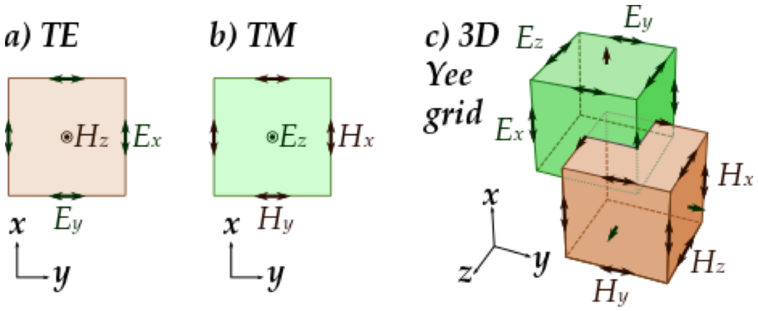

Figure 2.5. Illustration of computationally discretize electromagnetic fields in space and interleaving the fields components for higher precision. (a) and (b) are a two-dimensional case with the magnetic field and electric field along the axis respectively (perpendicular to the screen). (c) In the general case, the interleaving Yee grid is used.

$$\frac{\delta E_y}{\delta z}\Big|_{i+\frac{1}{2},j,k} \approx \frac{E_y\left(i+\frac{1}{2},j,k+\frac{1}{2}\right) - E_y\left(i+\frac{1}{2},j,k,k-\frac{1}{2}\right)}{\Delta z} \qquad \textbf{(2.28)}$$

which consequently becomes:

$$\frac{\delta H_x\left(i+\frac{1}{2},j,k\right)}{\delta t} + \frac{1}{\mu\left(i+\frac{1}{2},j,k\right)} \cdot \sigma^*\left(i+\frac{1}{2},j,k\right) H_x\left(i+\frac{1}{2},j,k\right) = -\frac{1}{\mu\left(i+\frac{1}{2},j,k\right)}$$

$$\cdot \left[\frac{E_z\left(i+\frac{1}{2},j,k+\frac{1}{2}\right) - E_z\left(i+\frac{1}{2},j,k,k-\frac{1}{2}\right)}{\Delta y} - \frac{E_y\left(i+\frac{1}{2},j,k+\frac{1}{2}\right) - E_y\left(i+\frac{1}{2},j,k,k-\frac{1}{2}\right)}{\Delta z}\right] \qquad \textbf{(2.29)}$$

The leap-frog scheme, as shown in Figure 2.6, uses all of the $\vec{E}$ components in the modeled space are computed and stored in memory by using the previously computed values of $\vec{E}$ and the newly updated $\vec{H}$ field data. At the next step, $\vec{H}$ is recomputed based on the previously obtained $\vec{H}$ and

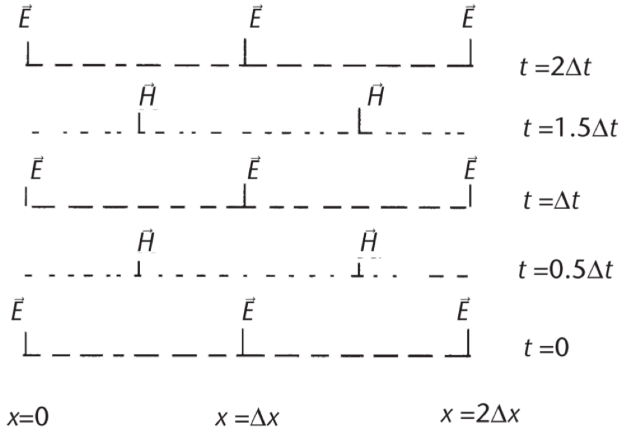

Figure 2.6. Leap-frog scheme. This graphical representation helps illustrate when and where the electric and magnetic fields are updated.

the newly obtained $\vec{E}$.

Already, limitations readily appear. In order to obtain accurate convergence, grid sizes on the order of $\lambda/20$ or $\lambda/30$ are required. This means that the step size must be very small in accordance with the Courant-Friedrich-Levy stability condition. This leads to very long simulation times, especially for small nanoplasmonic systems. Chapter III will discuss a method to circumvent this issue.

2.5 Review Current Challenges of Single Molecule Localization and Superresolution Imaging in Plasmonics

Super-resolution imaging has largely been recognized for its contributions to biological imaging, as demonstrated by the 2014 Nobel Prize in Chemistry [66], but the technique is quickly gaining popularity for addressing problems in materials science, finding utility in studying polymer dynamics, catalysis, and plasmonics.[67-74] Super-resolution microscopy is the name of a collection of techniques that allow imaging on scales beyond the diffraction limit faced by conventional optical microscopy. Plasmonics and super-resolution imaging naturally compliment each other, given that plasmonics provides a simple strategy to achieve subdiffraction excitation volumes using a far-field excitation source. Additionally, plasmonic nanostructures are by their very nature nanoscale in dimension, requiring subdiffraction-limited imaging tools to explore many of the subtle relationships between structure and function. The plasmon resonance is extremely sensitive to the shape, size, and composition (Figure 2.7) as well as its local environment, which is the basis of localized surface plasmon resonance (LSPR) sensing in which spectral shifts are measured as a function of the local dielectric environment.[57, 75, 76] Thus begets the question: Can superresolution imaging characterize

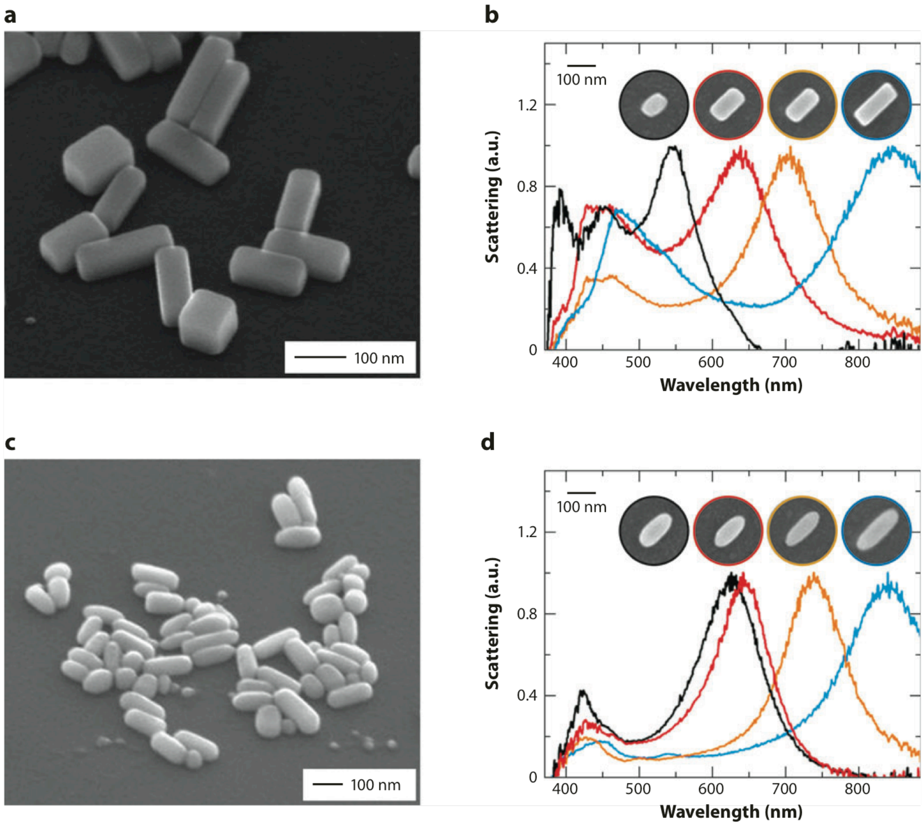

Figure 2.7. Scanning electron micrographs of (a) Ag nanobars and (c) Ag nanorice (45° tilt). (b) and (d) correspond to the dark-field scattering spectra of the different sized Ag nanobars and nanorice respectively. Figure was adapted and modified with permission from ref. [19].

plasmonic systems? To answer this question, we must first understand how superresolution imaging works.

The Rayleigh criterion tells us that two emitters spaced by less than $0.61\lambda/N.A.$ cannot be resolved as individual objects, where λ is wavelength and $N.A.$ is the numerical aperture of the imaging optic. The result is a lack of resolution when imaging subwavelength structures, leading to limited information regarding the true size/shape of a single emitter and an inability to discriminate multiple emitters within a diffraction-limited spot. For visible light, the resolution of a typical far-field optical image is ~250−300 nm. However, by introducing super-resolution imaging techniques, scientists regularly overcome this resolution limitation and routinely achieve resolution in the 5−20 nm range.[77-81]

Far-field super-resolution imaging can be broadly separated into two main classes, one based on tailoring the emission properties of single emitters and one based on tailoring the properties of the excitation field. The latter is applicable to devices such as Near-field Scanning Optical Microscopy (NSOM) [82] and stimulated emission depletion (STED)[83]. There are many great review articles on these subjects[82-85] but detailed explanation on these techniques will be excluded as it is beyond the scope of this thesis. For the former class, individual emitters are controllably modulated between emissive ("on") and non-emissive ("off") states such that only a single emitter is "on" within a diffraction limited spot at a given time.[79, 86, 87] The diffraction limited emission from that single emitter is then fit to a 2D-Gaussian. Localization is based on finding the peak of the fitted emitter point spread function. The fitting process is repeated multiple times as different molecules are switched between the "on" and "off" states, allowing the position of each emitter to be independently localized. Superimposing the positions of the individual emitters creates a composite reconstructed image. This approach to super-resolution imaging has many associated acronyms (STORM, PALM, PAINT, and GSDIM), typically distinguished by the mechanism with which molecules are modulated between emissive and non-emissive states.

To summarize, the principle of localization-based super-resolution imaging is a combination of two processes: (1) modulating the emission of a collection of emitters such that only a single emitter is active within a diffraction-limited spot at a given time and (2) localizing each emitter by fitting its diffraction-limited emission to a model function, such as a 2D

Gaussian. When applied to plasmonic nanostructures, dye emission intensity is typically used as a far-field reporter of the near-field intensity. Due to the strong electric field near the plasmonic nanostructure, the dye has enhanced emission when the excitation or emission frequency matches the plasmon resonance. Unfortunately there are detrimental problems with both emitter localization and probing the near-field intensity with dyes, as explained below.

2.5.1. Plasmonic Mislocalization

A fundamental approximation in localization-based superresolution imaging is that the position of a single emitter can be determined by fitting its diffraction-limited emission to a model function and assuming that the position of the fit peak matches the position of the emitter. In the case of a 2D Gaussian model, the diffraction-limited emission is fit to the following expression:

$$I(x,y) = z_0 + I_0 \exp\left(-\frac{1}{2}\left[\left(\frac{x-x_0}{\sigma_x}\right)^2 + \left(\frac{y-y_0}{\sigma_y}\right)^2\right]\right) \qquad \textbf{(2.30)}$$

Here, $I(x,y)$ represents the measured diffraction-limited emission across the (x,y) pixels, z_0 is the background intensity, I_0 is the peak emission intensity; σ_x and σ_y are the width of the distribution, and x_0 and y_0 are the location of the peak of the intensity distribution. This model has several limitations leading to localization errors in the calculated positions of single emitters relative to their true positions. These localization errors are further exacerbated when the molecule is in proximity to a plasmonic nanostructure. The diffraction limited emission is affected via a combination of mechanisms, including plasmon-molecule coupling, point spread function distortions, and image dipole formation.

Because plasmonic nanostructures effectively behave as nanoantennae for light, emission from single molecules (or any other emissive probe such as quantum dots or nanodiamonds) may couple into various plasmon modes of the nanostructure, leading to emission originating from the plasmonic nanostructure, rather than the emitter source. Haran and co-workers illustrated this principle by studying polarized SERS emission from single molecules adsorbed to silver nanoparticle dimers and found that the emission was polarized along the long axis of the dimer, rather than along the orientation of the molecule.[88] This suggests that the radiation originates from a highly coupled system, involving both the molecule, which generates the SERS signal, and the plasmonic nanostructure, which radiates that signal into the far-field. The high degree of coupling possible between a single molecule and a plasmonic nanostructure implicates a diffraction limited convolution between the two sources, such that localizing the emission does not produce the true position of the molecule nor the plasmonic nanoparticle. Thus, when localization-based super-resolution imaging techniques are used to probe the positions of molecules relative to a plasmonic nanostructure, significant localization error occurs. Biteen and co-workers illustrated this principle using a diffusion-based PAINT approach by localizing single molecule emission from Cy5.5 molecules diffusing to the surface of gold nanodisks with varying diameter.[20] In most cases, the authors localized the bulk of the emission events to the center of the disks (Figure 2.8), even though there was no capture chemistry to promote specific adsorption of the dye to the gold surface. This result suggests that the emission was not localized to the true position of each Cy5.5 molecule but was being coupled out through the plasmon modes of the gold disk, causing the position of the emission events to appear towards the center of the nanodisks.

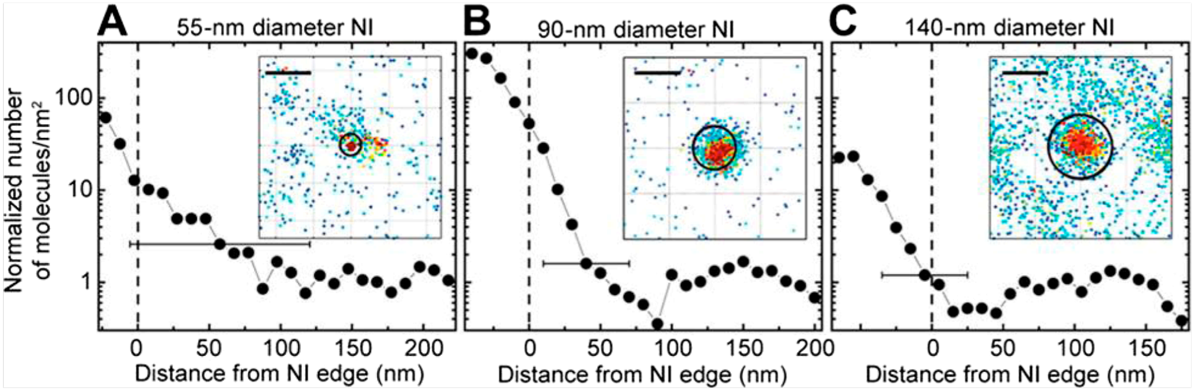

Figure 2.8. Normalized number of localized Cy5.5 molecules as a function of distance from the nearest edge of three different sized gold nanodisks with diameters of (A) 55, (B) 90, and (C) 140 nm. The dashed vertical line represents the edge of the nanodisk. The majority of the events are localized at the center of the disk, and a "depletion zone" with fewer-than expected events is located ~20-50 nm from the nanodisk edge. The insets show the scatter plot of the positions of the localized emission. The perimeter of the nanodisk is represented as a black circle. Scale bars: 100 nm. This figure is adapted with permission from ref. [20].

A major challenge with extracting the true position of a single molecule in this highly coupled plasmonic system is the number of variables that impact the coupling strength and therefore the extent of the localization error; these include the distance of the probe from the surface, the position of the probe relative to the nanoparticle surface, the orientation of the probe relative to the nanoparticle surface, and the spectral overlap between the probe and the plasmon resonance. While the molecule-particle distance is the easiest parameter to control by using spacer layers such as DNA, polyelectrolyte layers, and silica,[24, 89-91] the other parameters offer distinct experimental challenges.

Formation of image dipoles in a metallic structure also affect the emission pattern from a nearby emitter. When a dipole is placed near a plasmonic nanoparticle, it induces a dipole in the metallic structure called an image dipole. The image dipole serves as a secondary source of emission that will either interfere constructively or destructively with the emission from the original dipole, based on its orientation relative to the metallic surface (Figure 2.9.a).[33] This interference effect will shift the localized emission of the dipole away from its true position, as shown in the FDTD calculations in Figure 2.9.b. In the case when the dipole is oriented perpendicular to the nanowire surface, the dipole and image dipole interfere constructively, and the emission is localized between the two emission sources, closer to the nanowire surface (Figure 2.9.b, top). However, when the dipole is oriented parallel to the nanowire surface, it interferes destructively with the image dipole, shifting the localized emission further from the nanowire surface and away from the true position of the molecular emitter (Figure 2.9.b, bottom). The former case will lead to smaller-than-expected reconstructed images, while the latter will result in larger-than expected reconstructed images relative to the actual size of the nanowire substrate.

While the effect of variations in the local dielectric environment is typically neglected for single molecule emitters due to their small size (~1−3 nm), we cannot ignore this additional source of error for plasmonic nanostructures, which have dimensions in the tens of nanometers and therefore a significant possibility of sampling local environmental variations. However, if we are able to understand and capitalize on the emitter-plasmon coupling, the true localization of the emitter can be back calculated. A demonstration of this will be illustrated in Chapter V of this thesis.

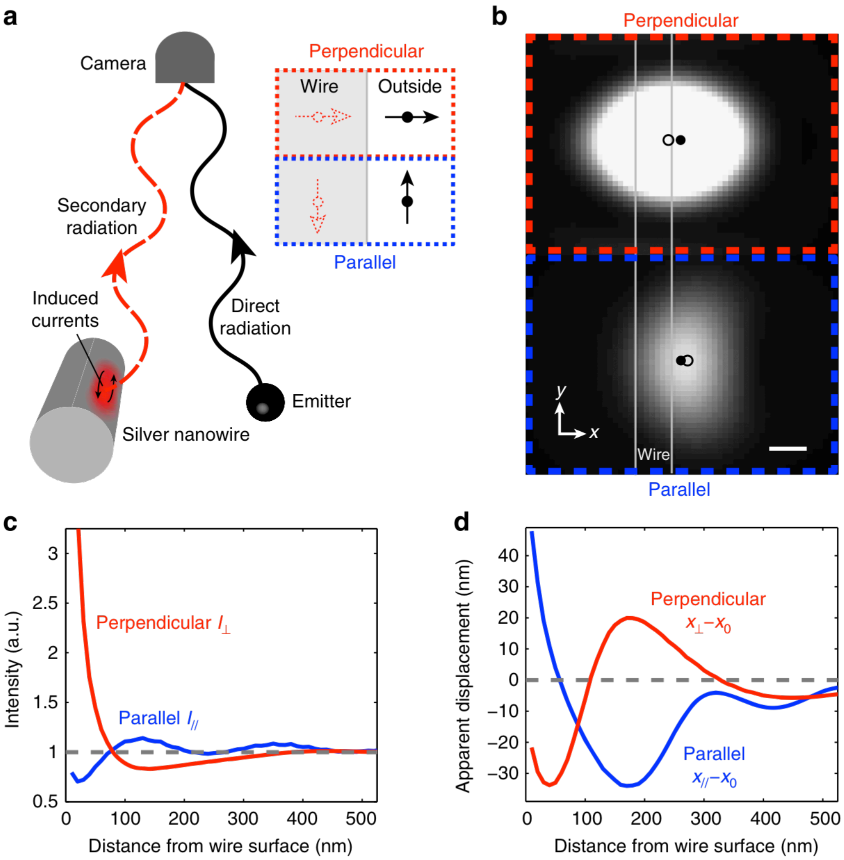

Figure 2.9. Image-dipole interference. (a) Illustration of interference between an emitter and secondary radiation from the nanowire. The emitter induces currents in the silver nanowire that radiate into the far field and interfere with the direct emitter radiation. Near the wire surface, modification to the far-field image can be described using an image-dipole model, as illustrated in the right inset, for dipoles oriented perpendicular (top) and parallel (bottom) to the surface. (b) Calculated far-field diffraction spots from an isotropic emitter located 30 nm from the wire surface (outlined in white) for emission polarized along the perpendicular (red) and parallel (blue) directions. Interference with the image dipole leads to differences in the intensities and displacement of the centroid positions (open circle) relative to the emitter position (closed circle). The coordinate system is shown at the bottom left. Scale bar, 100 nm. (c) Calculated intensity as a function of the distance of an isotropic emitter from the wire surface for the field polarized along the perpendicular (red) and parallel (blue) polarization directions. These curves have been normalized by the emitted intensity far from the wire. (d) The displacement of the diffraction spot position relative to the emitter position as a function of emitter distance from the wire surface for different emission polarizations. Figure is adapted with permission from ref. [33]

2.5.2. Probing Plasmonic Near-field with Dye Emission Intensity

There is an observable enhancement in fluorescence emission when interacting with a suitable plasmonic structure [24, 92]. Illuminated plasmonic nanostructures generating LSPR or SPP are able to squeeze the mode volume of light to deep sub-wavelength scales giving rise to large EM near-field power densities. When an emitter is placed within these enhanced fields it can experience illumination intensities many times that it would experience through plain illumination without the plasmonic structure. For emitter absorption frequency equal to plasmon resonance modes, the fluorescence emission will increase with the field strength [93, 94] assuming the emitter is not in a saturated state. For emitter emission frequency equal to plasmon resonance modes spontaneous emission causes increased fluorescence intensity with field strength (Figure 2.10). Absorption and stimulated emission can be described using the Purcell effect.[95] In this way LSPR act similarly to reflective cavities in which specific wavelengths are limited or selected by the geometry of the cavity. The emission enhancement of a fluorescent molecule is a feature of a plasmon's effect on the local density of states (LDOS) of space in its vicinity [96-98]. In this way, the emitter fluorescence intensity is a probe of the plasmonic near-field intensity. However, this process changes non-monotonically in close proximity to metallic surface.

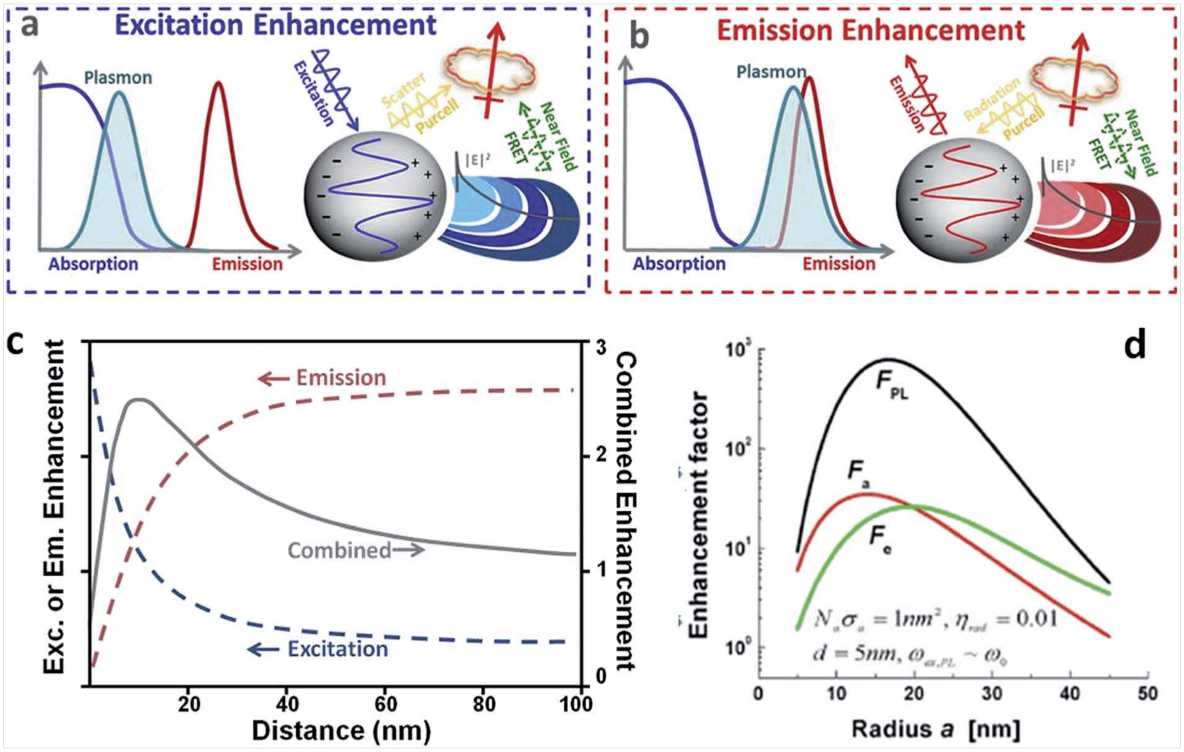

Figure 2.10. Dependence on distance and sphere radius of plasmon-enhanced fluorescence. (a) If the plasmon overlaps with the absorption of the fluorophore, and excitation enhancement is possible though the near-field and FRET or scattering. (b) If the plasmon overlaps with the emission of the fluorophore, and emission enhancement is possible through the Purcell effect or FRET. (c) The excitation enhancement (red line) falls off quickly with distance, while the emission enhancement (blue line) is quenched at short distances but increase rapidly. The combined photoluminescence enhancement, equal to the emission enhancement times the excitation enhancement, peaks around 10-30nm. (d) The optimal sphere radius for excitation (red line), emission (green line), and total photoluminescence enchancement (black line) varies with the balance between absorption and scattering. Adapted with permission from ref. [23]

When an excited emitter relaxes to the ground state via emission in free space, the photon is discharged into one of the states available to it. The number of states available is a function of the wavelength of the photon to be emitted. The number of states can be affected by the presence of a suitable plasmonic resonator. An emitter in close proximity will now have access to the plasmon modes as possible states to be utilized for emission (Figure 2.10.a and b). The increased number of states makes it easier to emit the photon, reducing the lifetime of the excited state and increasing the probability of a fluorescent emission instead of a dark transition back to the ground state. For this to be most effective the resonance of the plasmon must be close to the wavelength of the fluorescent emission. If this is the case, the fluorescent molecule's QY can be increased as more excitations result in fluorescent emission while at the same time, the molecule's fluorescence lifetime will be reduced as it spends less time in its excited state [96, 97]. Both of these effects lead to an increased number of photons collected for a fluorescent molecule imaged over a given time period as the fluorescence cycle time is reduced and more cycles are successful in generating fluorescent emission [99]. However, plasmonic structures also have non-radiative modes. Through a similar process it is possible to couple the molecules emission into these modes which will enhance the non-radiative emission of the dye. This leads to similar reduced lifetime but also reduced QY. At short distances of interaction fluorescent quenching begins to dominate [24, 96]. Quenching refers generally to any process whereby a material's fluorescence is reduced. Broadly this could be due to many things but in the case of a fluorescent materials' interaction with a metallic surface the most important factors are the non-radiative energy transfer to the structure mentioned previously and at very short ranges a direct energy transfer to the surface. We will consider the non-radiative decay rate enhancement separately leaving quenching for this system to be dominated by direct energy transfer. This happens at very short ranges through the direct transfer of excited charges to the metallic surface which stops all fluorescence. This is illustrated by Figure 2.11. The plot shows the fluorescent emission rate of a mCherry fluorescent protein. Initially fluorescent response grows with reduced separation up to a point where $z > 10$ nm, then, fluorescent rate drops sharply. Thus, fluorescent emission intensity is not a good candidate for measuring plasmon near-field intensity in close proximity to the metallic surface as the fluorescence intensity changes non-monotonically with distance from the metallic surface. In Chapter IV, an alternative method for measuring near-field intensities is discussed.

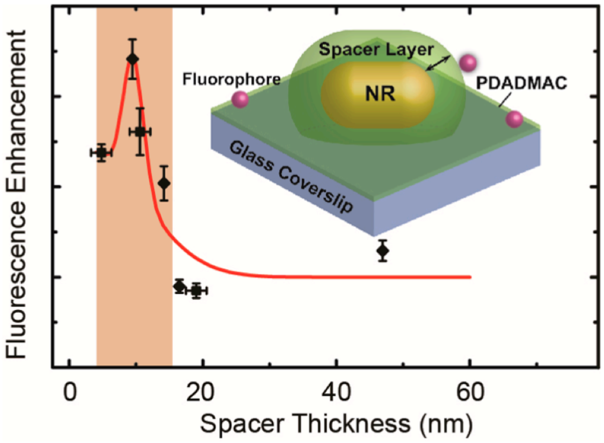

Figure 2.11. Intensity distribution of single mCherry fluorescent proteins one at a time as they adsorb on a conformal spacer layer 4.8−61.0 nm thick over a gold nanorod. The emission intensities depend non-monotonically on the spacer thickness, and an optimal spacer thickness of ~10 nm is observed for. Emission from fluorophores coupled to metal nanoparticles is affected by two competing processes: an enhanced spontaneous decay rate and quenching via nonradiative antenna modes. The inset shows a sketch of the experimental sample. This figure is adapted with permission from ref. [24]

CHAPTER III: Nearfield Numerical Methods – Nanodentures and Mechanical Electrodynamics: 3D Relative Orientation of Plasmonic Nanoarches from Absorption Spectra

3.1. Abstract

We propose a general theme, labeled mechanical electrodynamics, where the relative 3-D orientation of particles with nontrivial geometries is tracked based on the details of the absorption spectrum beyond a 1-D distance dependence. Specifically, we simulate absorption spectra of a subwavelength denture-like nanostructure with freely moving parts. The nanodentures are made of two gold nano-arches that either open and close or rotate about a single arch base (hinge rotation). We show how the absorption spectrum for the nanodentures changes depending on orientation and position. There is a ~0.1-0.2eV shift in absorbance peak frequencies as the denture closes, corresponding to an increased coupling between the two gold arches, while a hinge rotation results in a depletion of one absorbance peak (1.48eV) with the simultaneous emergence of a new absorbance peak at lower frequencies (0.88eV). The unique spectral signature of each position and orientation of the nanodentures points to a variety of applications. From this data, one could experimentally track and measure orientation and position of plasmonic-coupled nanoparticles using simple methods such as UV-Vis or IR spectral analysis. Additionally, the denture structure will tune in and out of different plasmon resonance frequencies, or turn "on and off," depending on its orientation. The simulations were performed efficiently by the recent Near-Field (NF) approach, which is a time-dependent Poisson algorithm

that shares a lot of the machinery of full-fledged Maxwell equations but allows for much larger time steps and therefore can treat large systems.

3.2. Introduction

Plasmonics on the nanoscale shows promise for chemical and biomedical sensing[100, 101], cancer treatment[102-104], and optoelectronic devices[105-108]. With control over composition, size, and shape of material, absorption in different materials can be tuned from the IR to the UV-Vis[109-111]. There has therefore been much effort to characterize and understand these plasmonic phenomena[112-119]. However, most systems are static, which gives rise to a single plasmonic spectrum. An alternative method of plasmonic tuning is to allow mobility and coordination of the nanoparticles. Thus, a system's plasmonic response depends on the orientation and distance of different plasmonic particles. We label this dependence mechanical electrodynamics.

Previous work on the electrodynamic response of dynamic systems has been limited. Most studies use the symmetry of the system to simplify the model, such as spheres[115, 120, 121] or rods[122] at different distances from one another. For example, colloid dimers shift their plasmonic resonance as they get closer or further away from one another[120, 121]. Dimers have therefore been used for tracking purposes[123], but most studies are limited to one dimensional movement, which limits the types of response that is collected. The less symmetry the nanoparticles have, the more variation is available in the spectral signature. With a more asymmetric system, such as two nano-arches studied here, there are more degrees of coordination, which results, as shown below, in multi-dimensional spectral signatures.

Predicting the spectra of these less symmetric systems increases computational time. With the recently developed Near-Field (NF) method[118, 124], computations are comparatively efficient. NF captures the electrodynamics of nanostructures at sub-wavelength scales. Below about a quarter of a wavelength, retardation effects can be ignored. This simplifies the treatment as the components of normal electric fields are neglected. Therefore, the Poisson equation is used since the time scale is not related to the inverse of the velocity of light, so a large time step can be used.

Here we use the NF approach to model the electrodynamics of a gold nanodenture structure, a system consisting of two gold nano-arches that open and close in a denture-like fashion or rotate about a hinge point (Figure 3.1). The mechanical electrodynamics of the system manifest as spectral shifts due to angle changes. Simultaneously, the spatial electric field was studied to help understand the plasmon coupling mechanism. The results show that there is rich information on 3D orientation in the spectral signatures of systems that are non-symmetric.

The chapter is organized as follows. Section II briefly reviews NF, the results of the simulations are presented in Section III, and discussions and conclusions follow in IV.

3.3. Method

NF is useful when the nanostructures are much smaller than the optical wavelength, in that retardation effects can be neglected. The longitudinal component of electric field then dominates so that the field is the gradient of an instantaneous scalar potential,

$$\boldsymbol{E} = -\boldsymbol{\nabla}\phi,$$

and fulfills the Poisson equation. The main advantage of NF is that since the method is not related to the velocity of light, the time step used for the evolution of electric field can be as high as a few atomic units, hundreds of times larger than that required in the Yee-type Maxwell finite-difference time-domain (FDTD) approach for sub-nanometer scales[125].

NF is essentially the time-dependent version of the frequency-dependent Poisson algorithm, where one solves

$$\nabla \cdot \left(\varepsilon(\mathbf{r}, \omega)\tilde{\mathbf{E}}(\mathbf{r}, \omega)\right) = 0, \tag{1}$$

where $\varepsilon(\mathbf{r}, \omega)$ is the permittivity of the material; $\tilde{\mathbf{E}}(\mathbf{r}, \omega)$ is the total electric field, made of the local longitudinal component and an external one. The difference from the usual Poisson algorithm is that NF is a time-domain method, and therefore all frequencies are solved for at once. In that respect NF is similar to the FDTD algorithm, although it uses much larger time steps. In the time-domain the electric field is

$$\mathbf{E}(\mathbf{r}, t) = -\boldsymbol{\nabla}\phi(\mathbf{r}, t) + \mathbf{E}_{\mathrm{ext}}(\mathbf{r}, t)\delta(t). \tag{2}$$

As in most FDTD descriptions, NF assumes that the dielectric permittivity of a metal is represented as a sum of Drude oscillators,

$$\varepsilon(\mathbf{r}, \omega) = \varepsilon_{\infty}(\mathbf{r}) + \varepsilon_0 \sum_{j=1}^{N} \frac{\beta_j(\mathbf{r})}{\bar{\omega}_j^2(\mathbf{r}) - i\alpha_j(\mathbf{r})\omega - \omega^2}.$$

Here, $\varepsilon_\infty(\mathbf{r})$ is the material-dependent frequency-independent term. For metals, we can assume $\varepsilon_\infty(\mathbf{r}) = \varepsilon_0$. The material-dependent Drude parameters $\alpha_j(\mathbf{r})$, $\beta_j(\mathbf{r})$, and $\bar{\omega}_j(\mathbf{r})$ are real-valued and we typically apply up to $N = 9$ oscillators to fit the permittivity over a wide frequency range, 0.6-6.7eV for gold[118].

To solve Eq. (1) in the time domain, the FDTD-type treatment in NF develops as follows. A metallic polarization and current density is defined for each for the Drude oscillators above and is evolved as $(j = 1, \dots, N)$

$$\frac{\partial \mathbf{P}_j(\mathbf{r},t)}{\partial t} = \mathbf{J}_j(\mathbf{r},t), \tag{3}$$

and

$$\frac{\partial \mathbf{J}_j(\mathbf{r},t)}{\partial t} = -\alpha_j(\mathbf{r})\mathbf{J}_j(\mathbf{r},t) - \bar{\omega}_j^2(\mathbf{r})\mathbf{P}_j(\mathbf{r},t) + \varepsilon_0\beta_j(\mathbf{r})\mathbf{E}(\mathbf{r},t). \tag{4}$$

Eqs. (3)-(4) are propagated by the leapfrog algorithm

$$\mathbf{P}_\mathrm{j}(\mathbf{r},t+dt) = \mathbf{P}_\mathrm{j}(\mathbf{r},t) + dt\,\mathbf{J}_\mathrm{j}\left(\mathbf{r},t+\frac{dt}{2}\right) \tag{5}$$

and

$$\begin{aligned}\mathbf{J}_j\left(\mathbf{r},t+\frac{dt}{2}\right) &= \frac{1-\frac{\alpha_j(\mathbf{r})}{2}dt}{1+\frac{\alpha_j(\mathbf{r})}{2}dt}\mathbf{J}_j\left(\mathbf{r},t-\frac{dt}{2}\right) \\ &\quad - \frac{dt}{1+\frac{\alpha_j(\mathbf{r})}{2}dt}\left(\bar{\omega}_j^2(\mathbf{r})\mathbf{P}_j(\mathbf{r},t) - \varepsilon_0\beta_j(\boldsymbol{r})\mathbf{E}(\mathbf{r},t)\right).\end{aligned} \tag{6}$$

To close these equations, we need the electric field. In FDTD, the electric field is propagated as an independent variable while in NF it is obtained from the overall potential, which is calculated in turn, at any time, from the polarization. Specifically, for purely metallic systems and a uniform initial external pulse, the electric fields is:

$$\mathbf{E}(\mathbf{r}, t = ndt) = \begin{cases} -\nabla\varphi(\mathbf{r}, t) & n > 0 \\ \dfrac{1}{dt}\mathbf{E}_{\text{ext}} & n = 0 \end{cases}$$

where the initial delta function in Eq. (2) is obtained (for purely metallic systems; see Ref. 25 for the extension to dielectrics) as:

$$-\nabla^2\varphi(\mathbf{r}, t) = \frac{\rho(\mathbf{r}, t)}{\varepsilon_0}, \tag{7}$$

where we defined a metallic charge density as

$$\rho = -\nabla \cdot \mathbf{P}(\mathbf{r}, t) \tag{8}$$

from the metallic polarization

$$\mathbf{P} = \sum_j \mathbf{P}_j\,. \tag{9}$$

The initial values for the propagation are

$$\mathbf{P}_j(\mathbf{r}, t = 0) = \mathbf{J}_j\left(\mathbf{r}, t = -\frac{dt}{2}\right) = 0. \tag{10}$$

To summarize this section: for purely metallic systems we start the simulation at $t = 0$ with a uniform electric field and no polarizations and currents, then propagate Eqs. (5)-(6), and at any time, step solve Eq. (7) by convolution.

The results are then Fourier transformed to yield $\mathbf{P}(\mathbf{r}, \omega)$, and the absorption spectrum is obtained from the absorption strength, defined as:

$$\alpha(\omega) = \frac{4\pi\omega}{c|\boldsymbol{E_{ext}}|^2} \int \operatorname{Im} \mathbf{P}(\mathbf{r}, \omega) \cdot \boldsymbol{E_{ext}} \, d^3\mathbf{r}, \tag{11}$$

where $\mathbf{P}(\mathbf{r}, \omega)$ is the frequency-dependent total polarization. In practice, unpolarized absorbance spectra were calculated by summing the trace of $\alpha(\omega)$ with x, y, and z polarized induced fields.

3.4. Results and Discussion:

A gold nanodenture structure was studied with dimensions shown in Figure 3.1. Our absorbance calculations were benchmarked for the open denture (Flat or θ = 180˚), half-way open (θ = 90˚), and closed (θ = 0˚) (see also supplementary Figure 3.1). Two hundred mesh grid points in each dimension were necessary for satisfactory convergence with the half-way open and closed geometry, while three hundred mesh grid points were necessary for the open denture geometry. The structure was then tested in two different cases: denture closure (Figure 3.1.b) and hinge rotation (Figure 3.1.c). For denture closure, the angle q, ranging from 180˚ to 0˚ in 45˚ increments, was generated from the nanoarches rotating out of the plane towards one another while connected at both bases at the spring line (in architecture, the spring line is the point at which the arch first begins to curve to create the arch structure). With hinge rotation, the angle j, varying between 0˚ to 180˚ in 45˚ increments, was generated from the rotation of the nanoarches connected at a single base at the spring line. The spectra were monitored as shifts in absorbance peaks with the change in geometry. Experimentally, this is the equivalent of a switchable polymer linker connecting the bases of the nanoarches and controlling the mechanics of the nanodenture system.

Initially two characteristic absorbance frequency peaks are seen from a single gold arch found at 1.37eV and 1.97eV (Figure 3.2.a). However, when another gold arch is introduced in the "flat" or θ = 180˚ denture position, the lower frequency peak is blue shifted by ~0.11eV while the higher frequency peak remains virtually unchanged. This is due to the newly introduced plasmon coupling between the two nano-arches.

As the dentures close (Figure 3.1.b), the absorbance frequency peaks are blue shifted by 0.1-0.2eV (1.48eV to 1.60eV for the low frequency peak and 1.93eV to 2.16eV for the high frequency peak) (Figure 3.2.b). This shift is explained by a stronger coupling between the two arches as the dentures close compared to the flat geometry. With more surface area and a smaller distance between the arches, there is a stronger coupling, which causes the peak shifts in the spectrum.

Interestingly, the initial 180˚ to 90˚ angle change does not shift the frequency peaks drastically compared with the last 90˚ to 0˚. This is due to the limited range of the plasmon coupling in the arches. The last 90˚ to 0˚ angles puts the surfaces of the two arches much closer to one another than the 180˚ to 90˚ angles initially do. Thus, there is a stronger interaction between the two nano-arches between 90˚ to 0˚ angle.

For the hinge rotation case (Figure 3.1.c), a drastically different effect is seen. Instead of a gradual shift in absorbance frequency peaks, there is a disappearance of a dominant absorbance peak and the emergence of another (Figure 3.3). As the arch rotates about one of the other arch's base, the absorbance frequency peak at 1.48eV decreases while the absorbance frequency peak at 0.88eV starts to emerge. By the time the nano-arch has rotated 180°, the first frequency peak (1.48eV) has fully depleted while the new frequency peak (0.88eV) has fully emerged. This happens in a fairly linear fashion, illustrated by the nearly equal intensity levels of both peaks at the 90° rotation. The frequency shift is due to a decoupling of the two nanoarches as an arch rotates away from the other arch. It is important to note the large frequency difference of 0.6eV from the two peaks. This will be useful for devices that need to be tuned in and out of a plasmonic frequency, or "on and off."

Additionally, note how different the two methods of plasmonic tuning are due to different mechanical electrodynamic properties of the system. This illustrates the versatility in which less symmetric systems can be tuned. Unlike the dual nanocolloid system, gold nano-arches have a multifaceted way of tuning themselves with different mechanical movements giving potentially very different spectral results. Furthermore, each orientation gives a unique result. This is important for tracking orientation and position via far-field methods such as UV-Vis and IR absorption, as each orientation and position has a unique spectral signature. This also gives rise to avenues of mechanically tuning and detuning plasmons through rearranging the nanostructure's orientation.

To help analyze the characteristic effects of the mechanical electrodynamics, the spatial electric field was simulated by NF for the gold nanodenture structure (Figure 3.4). For ease of visualization, the Flat (or 0°) nanostructure was chosen. The electric field response was visualized in the *z*-plane that bisects the gold nanodentures. Inside the material, the electric field response is roughly zero due to no net change in electric field. Thus the *z*-polarized light is not included in the figures. For *x*-polarized electric fields, the response is greatest along the outside rim near the spring line of the nanoarches. For *y*-polarized electric fields, the electric field is greatest between the two arches at the bases, though is not insubstantial at the tip of the arcs. This spatial information helps explain why the frequency of absorption peaks shift.

The *x*-polarized and *y*-polarized electric field images illustrate the initial coupling between the two nano-arches and thus explain the initial frequency peak shift as this coupling is initiated. It also helps explain the characteristic effect of both the denture closing case and the hinge rotation case. As the nanodenture starts to rearrange, the coupling starts to change. Since the main source of coupling is initially at the hinge point, it is not surprising that the spectrum changes as the orientation around the hinge point changes, either from the dentures closing or a hinge rotation.

With the spectra of systems and identifying coupling regions, or hot spots, it is clear that these less symmetric systems have complex properties that need to be explored.

3.5. Conclusion:

With less symmetric nanostructured systems, there is more complexity in orientation and position. This leads to interesting coupling dynamics with the plasmons, and the NF-predicted spectrum for the gold nanodentures illustrates this phenomenon well. Depending on how the system is changed, either denture closing or hinge rotation, the spectrum changes in drastically different ways. There is a unique ~0.1-0.2eV frequency peak shift for the two major peaks of the gold nano-arches as the nanodenture closes. On the other hand, there is a peak depletion at 1.48eV and a peak emergence at 0.88eV for a hinge rotation.

The versatility in the mechanical electrodynamics leads to potentially interesting applications. Due to the nature of the shifts and changes in intensity of the peaks caused by the mechanical electrodynamics, applications in tracking via far field methods such as UV-Vis and IR absorption could be envisioned. Additionally, if the orientation could be controlled via a linking molecule or polymer, the plasmon could be switched in and out of resonance with ease. This could be useful for plasmonic devices that require an “on and off” state.

In future studies, it would be interesting to extend the NF method to other frequency regimes. It would also be interesting to further study other less symmetric systems or a completely asymmetric system to see what sort of mechanical electrodynamics could be exploited for experimental purposes and to search for optimal structures in which the spectrum changes even more drastically and uniquely depending on the relative orientation.

3.6. Figures

Gold Nanodenture Geometry

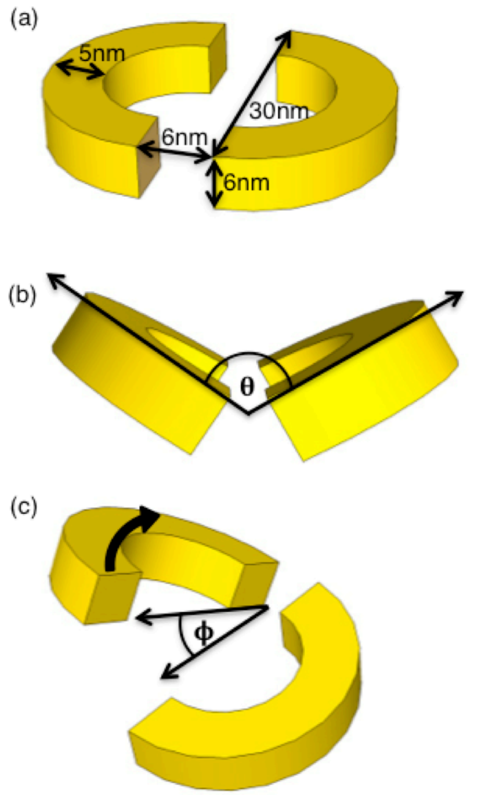

Figure 3.1. Model of the gold nanodenture system with **(a)** “flat” geometry, **(b)** closing mechanical motion, and **(c)** hinge rotation mechanical motion.

Denture Closing Absorbance Spectrum

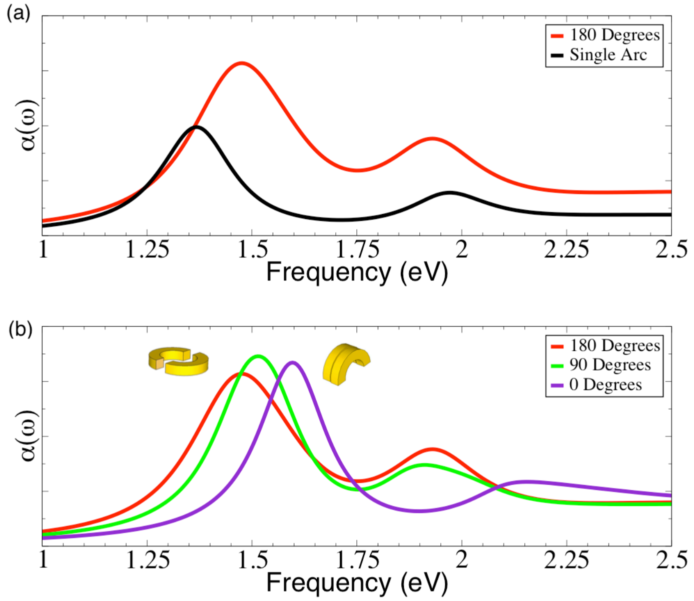

Figure 3.2. (a) The calculated absorbance spectra of a single gold nanoarch and two gold nanoarches in a denture-like geometry. The lower frequency peak blue shifts due to coupling between the two arches. **(b)** As the arches close, the frequency of absorption shifts higher. This is due to increased coupling between the two arches. Intermediate angles are shown found in Supplementary Figure 3.2.

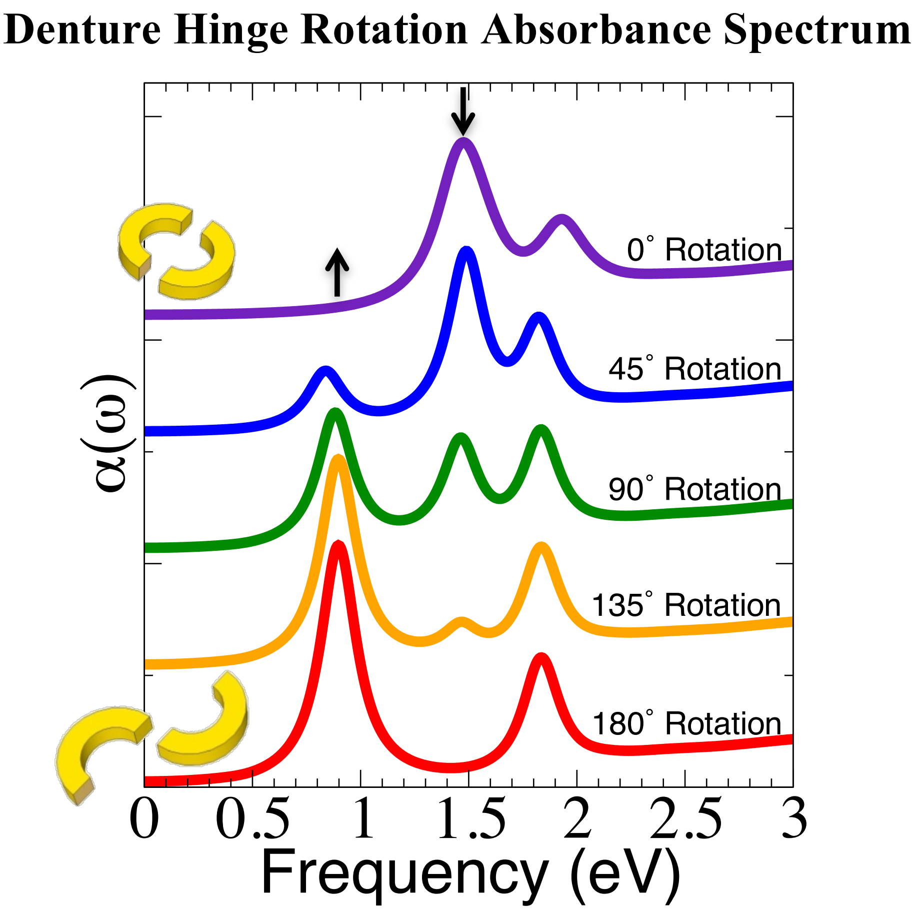

Figure 3.3. Absorption spectrum of a gold nanodenture system as the arches rotate about a single arch base at the spring line. As the arches rotate, the frequency of absorbance turns "on and off" as a major peak disappears while another emerges (indicated by the arrows). This trend is due to a decreased coupling of the nanoarches at the spring line.

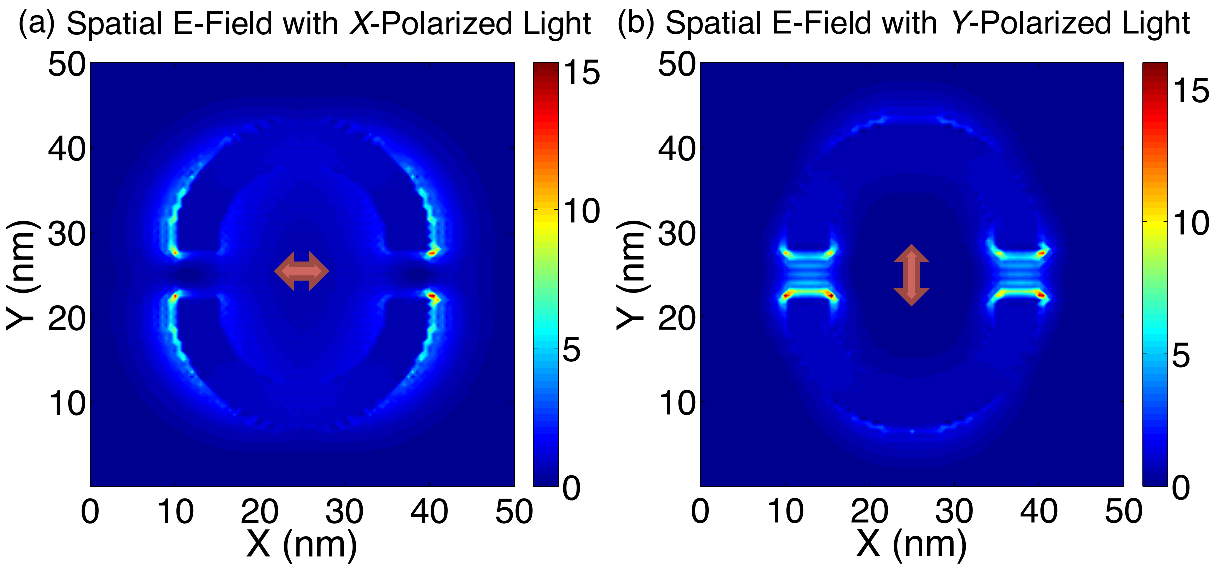

Figure 3.4. Spatial energy distribution of the gold nanodenture system for **(a)** *x*-polarized light and **(b)** *y*-polarized light. The local hotspots can be seen near the hinge points of the nanodenture system. The double arrows illustrate the direction of polarization.

3.7. Supplementary Information

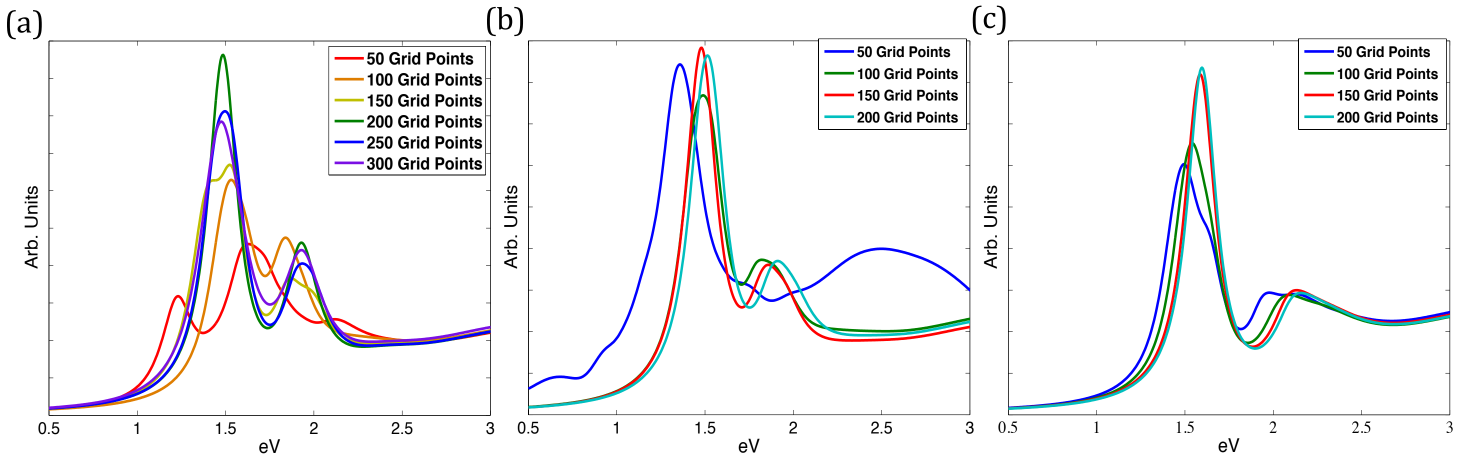

Supplementary Figure 3.1. Convergence test for **(a)** θ = 180˚, **(b)** θ = 90˚, and **(c)** θ = 0˚. For θ = 180˚, 300 mesh grid points was necessary for convergence of θ = 180˚ while 200 mesh grid points was necessary for θ = 90˚ and θ = 0˚.

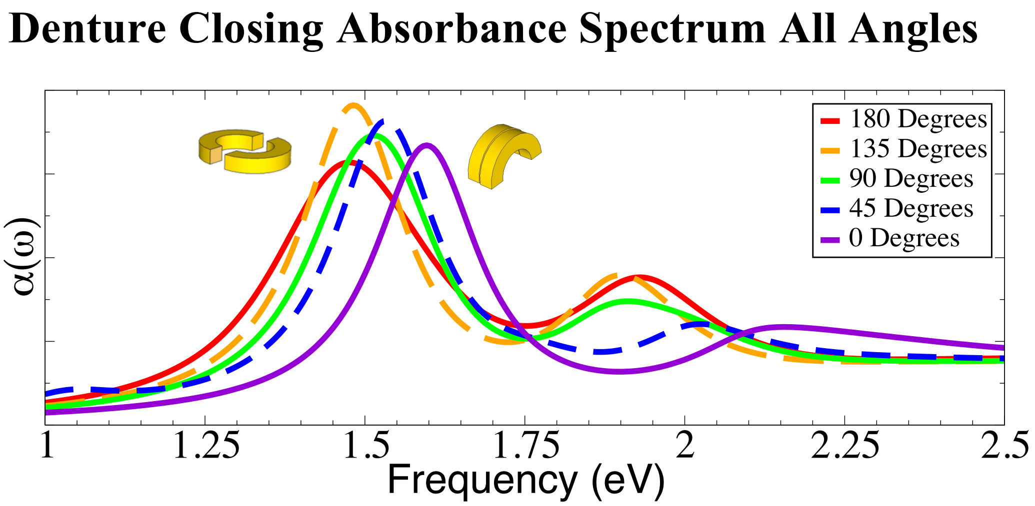

Supplementary Figure 3.2. The calculated absorbance spectra of the nanodentures. As the arches close, the frequency of absorption shifts higher: θ = 180˚, 135˚, 90˚, 45˚, and 0˚ geometry. This is explained by increased coupling between the two arches.

Chapter IV: Far-field Superresolution Detection of Plasmonic Near-fields

4.1. Abstract

We demonstrate a far-field single molecule superresolution method that maps plasmonic near-fields. The method is largely invariant to fluorescence quenching (arising from probe proximity to a metal), has reduced point-spread-function distortion compared to fluorescent dyes (arising from strong coupling to nanoscopic metallic features), and has a large dynamic range (of two orders of magnitudes) allowing mapping of plasmonic field-enhancements regions. The method takes advantage of the sensitivity of quantum dots (QDs) stochastic blinking to plasmonic near-fields. The modulation of the blinking characteristics thus provides an indirect measure of the local field strength. Since QDs blinking can be monitored in the far-field, the method can measure localized plasmonic near-fields at high throughput using a simple far-field optical set-up. Using this method, propagation lengths and penetration depths were mapped-out for silver nanowires of different diameters and for different dielectric environments, with a spatial accuracy of ~15 nm. We initially use sparse sampling to ensure single molecule localization for accurate characterization of the plasmonic near-field with plans to increase density of emitters in further studies. The measured propagation lengths and penetration depths values agree well with Maxwell finite-difference time-domain (FDTD) calculations and with published literature values. This method offers advantages such as low-cost, high-throughput, and superresolved mapping of localized plasmonic fields at high sensitivity and fidelity.

4.2. Introduction

Surface plasmon polaritons (SPP), the coupling of photons to charges at metal interfaces, improves the efficiency of sensing,[2, 3] energy transfer,[12, 126, 127] and catalysis.[128] There has been much effort to optimize plasmonic systems and exploit their field enhancement property. However, the system structure, resonance frequencies, and field enhancement, are all coupled – making characterization difficult.[129] Thus, with the development of plasmonics-based devices and circuits, there is a growing need for detecting and characterizing plasmonic effects in large systems. While Maxwell Finite-Domain Time-Difference (FDTD) simulations can handle ideal systems, measurement and characterization of realistic (imperfect) experimental systems is desired. The common approach for measuring plasmonic fields is near-field scanning optical microscope (NSOM),[25, 28, 31] which is slow due to a feedback loop. Alternates, such as two-photon luminescence imaging,[34] electron energy loss spectroscopy,[35, 36] photoemission electron microscopy,[37] cathode-luminescence spectroscopy,[38] and bleach-image plasmon propagation (BlIPP),[39, 126, 129] are still diffraction limited, costly, or have low throughput.

Single-molecule superresolution methods, such as PALM and STORM, have better resolution than conventional optical microscopy.[40-42] The simplest superresolution approach for measuring plasmonic fields uses a polymer layer doped with fluorescent molecules close to a planar metal layer.[24, 43, 44] Such emitters could be localized at high precision and their emission intensity should be measured (assuming that it is proportional to the plasmonic excitation field). However, characterization of plasmonic near-fields using an emitter's fluorescent intensity has many complications. Fluorescence enhancement and quenching effects cause the fluorescence intensity to vary non-monotonically as function of the probe distance less than 30 nm from the metal.[24, 45] Additionally, the point-spread function (PSF) of an emitter placed within 100 nm of a metallic surface is distorted due to strong electromagnetic coupling of the emitter's dipole to the nearby metallic structure. The superposition of scattered light PSF from the metal surface and dipole emitter PSF causes an erroneous localization of the far-field PSF away from the true location of the probe.[20, 33, 46, 47] When within several nanometers of a metallic structure, a distance of particular interests for nanoparticle plasmonics, the underlying structure can completely distort an emitter's PSF to non-Gaussian shapes making localization difficult without knowing the underlying structure.[46] Lastly, the relation between excitation and emission is non-linear at strong fields due to saturation.

Here, stochastic quantum dot (QD) blinking[130-133] is proposed and demonstrated as an approach for sensing plasmonic near-fields. Previous studies have already demonstrated that QD blinking is relatively invariant to enhancement and quenching effects.[134] Additionally, spherical QDs have a degenerate in-plane dipole and therefore weaker electromagnetic coupling to metallic antenna structures.[33, 135, 136] The weaker coupling creates less distortion in the QD PSF and should allow more accurate localization compared to a conventional fluorescent dye.[33] Using these attributes, we show that blinking QDs are good reporters of plasmonic (near) field strength. Moreover, QDs' blinking can be monitored using wide-field, far-field optics at high throughput and high localization accuracy.

A direct demonstration of the spatial and field intensity sensitivity of blinking QD reporters is done here on silver nanowires (Ag NWs). Ag NW waveguides have an inhomogeneous (decaying) field distribution both in the SPP propagation direction (along the long direction of the wire) and penetration depth direction (perpendicular to the long direction of the wire).[64] QDs were spin-coated on top of Ag NWs having different dimensions and dielectric environments. The wires were over-coated with either two different types of dielectric layers: SiO_2 or poly(methyl methacrylate) (PMMA). The wires were then sparsely labeled with QDs ~30nm from the Ag NW surface to ensure accurate single molecule localization and extraction of the plasmonic near-field strength. These experiments allowed us to test the dependence of the SPP propagation decay length and penetration depth on the wire diameter and on the environment's dielectric constant. The fitted experimental results for propagation length and penetration depth were favorably compared to FDTD simulations and to values reported in published literature.

4.3. Results and Discussion

4.3.1. Field Intensity Sensitivity of QDs

Optical field intensities affect the stochastic switching of QDs between an 'on'-state with a high photon emission rate and an 'off' low emission state. Stochastic switching, also known as 'intermittency', or 'blinking',[130-133] has been studied extensively, both experimentally and theoretically.[130, 133, 137-139] Auger recombination is commonly invoked to explain blinking,[140-142] but other processes, such as surface and heterointerface charge trapping have also been shown to contribute to the switching.[143, 144] Auger recombination is a three-particle process that results in a nonradiative transition due to the absorption of energy from an exciton by a spectator particle, leaving the QD charged, and in a ‘dark’, or ‘off’ state. Only once the charged QD is neutralized does the emissive ‘on’ state resume.

Blinking in QDs is inherently stochastic and independent of other nearby QD emitters. Traditionally, emission from a single QD is recorded in time bins to analyze the blinking phenomena. A threshold is used to discern ‘on’ and ‘off’ time periods in the telegraph noise-like time trajectory and histograms are constructed for the ‘on’ and ‘off’ periods. At low excitation power, the histograms exhibit a near perfect power law distribution for both the ‘on (+)’ and ‘off (-)’ states, described by $P_{+/-}(t) = t^{-m}$. For higher excitation energies, the ‘on’ time distribution starts to bend at long ‘on’ times ($P_{+} = t^{-m}e^{-\Gamma t}$ where Γ is the intensity bending parameter)[130-133]. Here, m is the slope of the on/off-time probability distribution in a log-log plot. Thus the stronger the excitation intensity, the shorter the ‘on’ periods and the more likely the QD will be to enter an ‘off’ state. The bending parameter, Γ, yields information on the excitation field *via* the blinking statistics of individual QDs.

To further establish the relationship between Γ and the excitation field strength, blinking experiments were performed similarly to previously published works. However, since typical analysis of on/off time histograms can lead to a 15-30% bias in extraction of parameters (depending on background noise and binning of photons[139]), we instead utilized autocorrelation functions (ACFs) for the analysis. ACFs are mostly insensitive to binning and thresholding artifacts and therefore provide a more reliable and robust analysis,[145, 146] The bending parameter Γ was analyzed as a function of increased excitation intensity. Following Verberk and Orrit [147], the Laplace transform of the normalized ACF can be written as:

$$g(s) = \frac{1}{s}\left[1 - \frac{1}{sT_+} \times \frac{(1-p_+)(1-p_-)}{1-p_+p_-}\right] \quad (4.1)$$

where $p_+(s)$ and $p_-(s)$are the Laplace transforms of the on/off-time probability distributions, $P_+(t) \propto t^{-m}e^{-\Gamma t}$ and $P_-(t) \propto t^{-m}$ respectively, and where T_+ is the average on-time. Simplifying with the assumption that the minimum capture window will be much smaller than the total time trajectory collected, such that $s \rightarrow 0$, and transforming back with an inverse Laplace transform, we get:

$$1 - G(\tau) = \beta(m)\theta^{m-1}\Gamma^{2-m}\tau^{2-m} \quad (4.2)$$

where θ is the minimum capture window and $\beta(m)$ is a numerical function (product of Gamma-functions) of m. The parameter θ is known from the experimental minimum capture time (10 msec in our case). A full derivation of equations (4.2) is given in the Supplementary Information (SI).

Benchmark studies of Γ as a function of excitation power were performed on 30 individual CdSe/ZnS core-shell QDs with emission centered at 800 nm. Figure 1a shows typical intensity trajectories from a single CdSe/ZnS core-shell QDs at different excitation powers, excited at 642 nm with a continuous wave (CW) laser (Coherent, Wilsonville, OR). The 800 nm emission from the QDs was filtered from the excitation wavelength using a 750 nm long band-pass filter (ThorLabs, Newton, NJ) and intensity measured in wide-field with an EMCCD camera (Andor, Waltham, MA). As the excitation power increases, the normalized ACF decays more rapidly due to shortened ‘on’ times (Figure 4.1b). For a single QD, the autocorrelation function at different excitation powers were fit to Eq. (4.2), keeping m a global variable between excitation power and Γ a local variable. This procedure was repeated for all 30 QDs (average ACFs in Figure 4.1c). The resulting fit of m for each QD gives $m = 1.40 \pm 0.03$, in good agreement with previously reported values of $m \approx 1.5 \pm 0.2$.[137] When fitting the intensity parameter Γ as a function of excitation power, a linear trend is observed over two orders of magnitude of intensity. When the data is fit we obtain a direct relationship between $\Gamma^{2-\mathrm{m}}$ and excitation power:

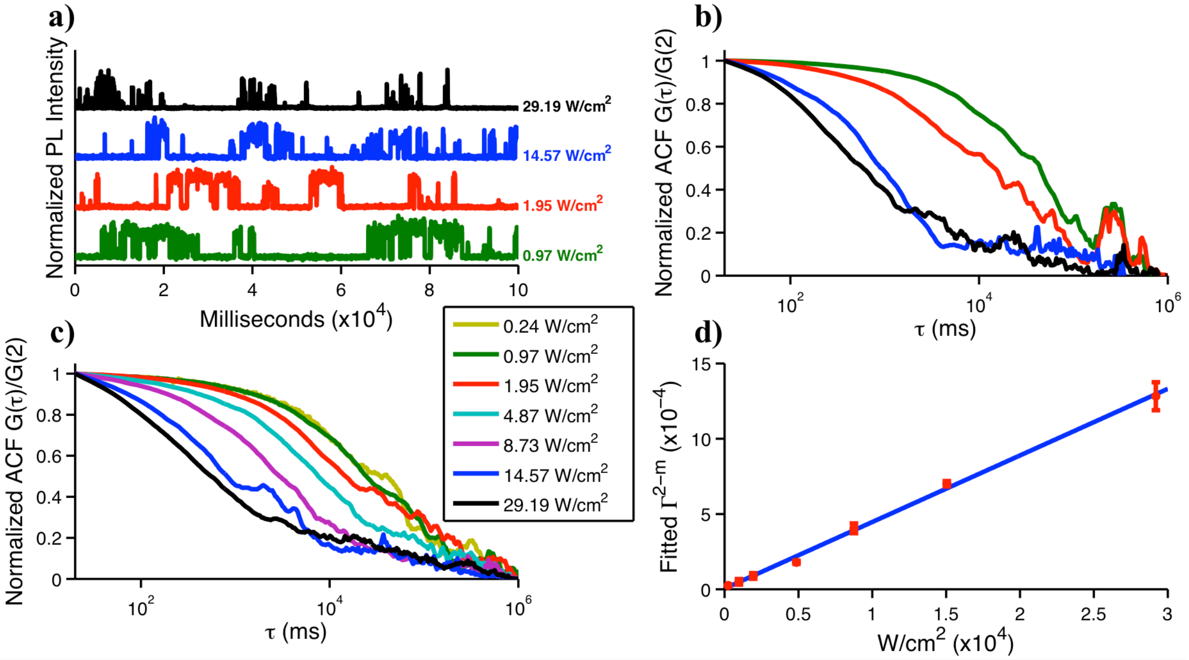

Figure 4.1 | QD excitation intensity sensitivity. (a) Typical intensity trajectories of a single QD under a 642nm CW laser excitation for varying excitation powers. **(b)** Corresponding normalized ACFs of a single QD at different excitation powers. **(c)** Averaged normalized ACFs from 30 individual QDs at various excitation powers. A clear trend of a faster decaying ACF is seen at higher powers due to shorter ‘on’ lifetimes. **(d)** A plot and a fit to Γ^{2-m} as function of excitation power density (according to Eq. 2). The results show a clear linear trend within the tested dynamic range of power densities. The fitting yields: $\Gamma^{2-m} = 4.4\times10^{-8} W/cm^2 \times P + 4.3\times10^{-6}$, where P is excitation power in W/cm^2.

$$\Gamma^{2-m} = 4.4\times10^{-8}[cm^2W^{-1}s^{-1}]\times P + 4.3\times10^{-6}[s^{-1}] \qquad (4.3)$$

where P is excitation power (Wcm^{-2}) (Fig. 4.1d). These results follow a similar trend to previously reported values extracted using different analysis methods.[145, 148] Fig. 4.1 therefore represents a calibration method for determining the excitation intensity from the blinking behavior of individual QDs. We dub this approach as COFIBINS (**C**haracterizing **O**ptical **F**ield **I**ntensity by **B**l**I**nking **N**anoparticle**S**).

4.3.2. Extracting the plasmonic field intensity by localized blinking QDs

A direct application of COFIBINS to the characterization of plasmonic waveguide (*i.e.* extraction of propagation length and penetration depth) by localized blinking QDs is demonstrated next.

Three different NW waveguides with mean diameters of 160, 290, and 400 nm were prepared in order to test the variation of SPP propagation lengths and penetration depths as a

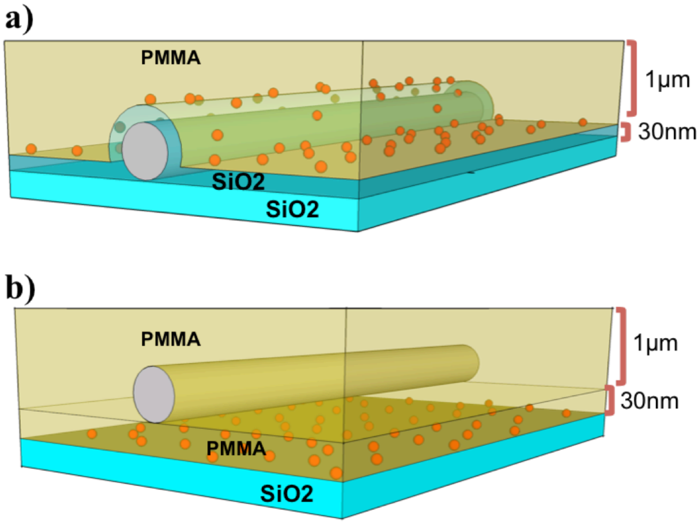

Figure 4.2 | Sample schematics. Samples structures and dimensions of silver nanowire surrounded by **(a)** silicon dioxide and **(b)** PMMA. Notice that QDs (red dots) are at the SiO_2-PMMA interface for both samples.

function of Ag NW diameter. Additionally, the Ag NWs were over-coated with either a 30 nm thick SiO_2 layer or a 30 nm thick PMMA layer in order to compare differences in propagation lengths and penetration depths as a function of the refractive index of the two environments. The prepared system dimensions are shown in Figure 4.2. Additional experimental details are given in the SI.

The dielectric dependence studies were designed to create two different dielectric environments for the Ag NWs (SiO_2 or PMMA) while keeping QDs in a constant environment (PMMA-SiO_2 interface, see Fig. 4.2) since QD blinking has been shown to be sensitive to the immediate dielectric environment.[148] The QDs were spin-coated with an areal density of ~1.8 QDs/μm^2 (to ensure single particle localization conditions). Upon localized excitation at one end of the silver nanowire, the plasmonic field intensity exponentially decays along (and perpendicular to) the wire. The 2-D mapping of the plasmonic field is accomplished by localizing each QD PSF centroid relative to the Ag NW and extracting the local field intensities of each QD from their blinking time intensity trajectories. Figure 3b shows a single frame from a movie that recorded the emission from QDs dispersed over the SPP waveguide. The location of each QD was localized (by 2D Gaussian fitting) with a spatial accuracy of ~15nm. Accuracy was determined from fitting experimental data with a known background plus the calculated error due to the dipole-SPP coupling as modeled below (see Supplementary Information for more details). The calculated error in localization is represented by the error bars in Figure 4.4 (b) and (c).

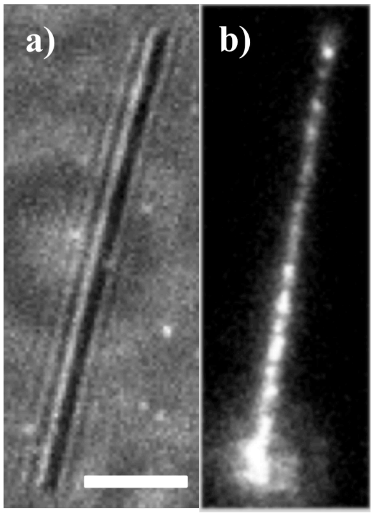

Figure 4.3 | SPP propagation image. Silver nanowire with dimensions 0.2μm x 20 μm **(a)** under bright field illumination and **(b)** wide-field fluorescence image of blinking QDs on top of the wire. A diffraction-limited focused laser excitation excites the silver wire at its bottom end. of the silver wire. The plasmon propagation is visualized by the evanescent field exciting the QDs on the wire. Scale bar is 4 μm.

The physical location of the metal wire relative to the QD was determined by drawing a straight line between two Gaussian fits to the scattered light emanating at the downstream end of the wire, as the SPP were alternatively excited at each end (see SI Fig-2 for more details). The extracted radial distance (perpendicular to the long axis of the wire's center), longitudinal distance from the wire's end, and intensity dependent Γ factor were then extracted for each QD. The origin of the 2D plane is defined as the locally excited Ag NW end found by fitting a 2D Gaussian to scattered light at the end. We define the x-axis as the propagating field along the long axis of the wire and y-axis the field penetration into the local media orthogonal to the Ag NW. For simplicity, the y-axis was mirrored such that $y = -y$. Figure 4 plots the near-field intensity extracted from the Γ value of each QD, using equation (4.3), and plotted against the fitted x and y PSF location. The near-field intensity data was broken into two groups to make the data more palatable: propagation length and penetration depth. The extracted normalized QD intensity data was initially fit to the function $I(x, y) = N \times \exp(-x/P_l) \times \exp(-y/P_d)$, where N is the amplitude, P_l is the SPP propagation length, P_d is the SPP penetration depth, x is the distance along the wire, and y is the distance perpendicular to the wire. The fit values of P_l and P_d are then graphed in Figure 4. 4 (b) and (c) as $I(x)/N = \exp(-x/P_l)$ and $I(y)/N = \exp(-y/P_d)$

respectively. The extracted normalized individual QDs intensities are separated into propagation length and penetration depth plots as $I(x) = I(x, y)/Nexp(-y/P_d)$ and $I(y) = I(x, y)/Nexp(-x/P_l)$, illustrating QD's sensitivity to position along- and perpendicular to- the Ag NW. The exponential decays along- and perpendicular to- the Ag NW are evident. We measured 8 individual Ag NWs for each combination of dielectric environment (SiO_2 and PMMA) and Ag NW diameters (160 nm, 290 nm, and 400 nm) for a total of 48 samples. The extracted SPP propagation length and penetration depth are compared to theoretical FDTD predictions in Table 4.1 and Figure 4.5.

4.3.3. Comparing analytical and FDTD predictions

Ag NW waveguides were modeled using Maxwell finite-difference time-domain (FDTD) method. Simulation parameters matched the experiments. Experimentally determined NW diameters (SI Fig-4.2) and literature values for SiO_2 (n = 1.542) and PMMA (n = 1.488) refractive indexes were used. For the complex dielectric function of Ag, the tabulated values by Johnson and Christy were used.[149] The complex refractive index used in simulations was fit using 9 drude oscillators derived in a previous work.[150] Ag NW waveguides were excited in the simulation at one end with a focused 642 nm CW laser beam (with a PSF of 321 nm FWHM) at the wire's end. See SI for detailed information on the simulations. Fig. 4.5 shows the theoretical dependencies of the propagation length and penetration depth parameters on the wire diameter and on the surrounding refractive index. Oddly, the PMMA sample penetration depth increases as a function of nanowire diameter. This result is due to the geometry of our sample and is explained in detail in the SI (and SI Fig-4.4).

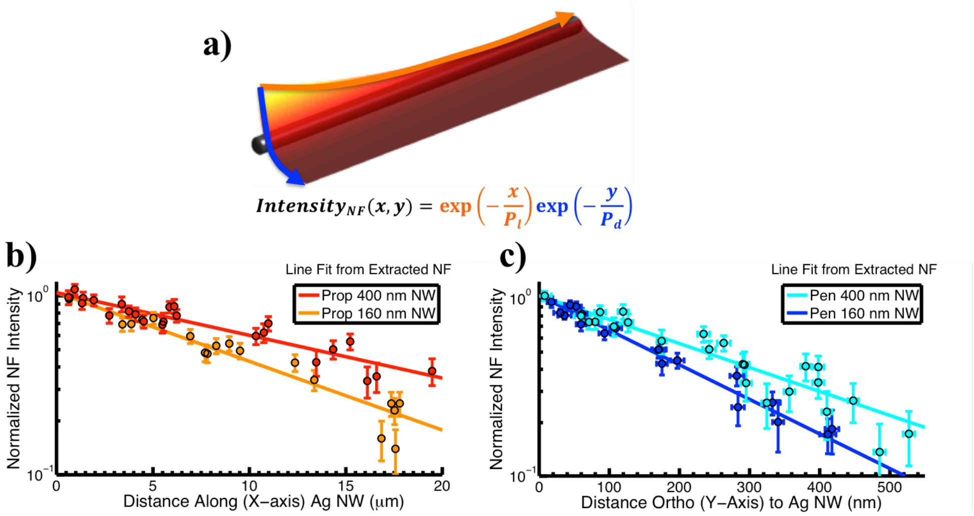

Figure 4.4 | Near-field intensity as a function of QD position. (a) Near-field intensity as a function of distance from excitation point along an Ag NW. **(b)** and **(c)** Extracted near-field intensity (normalized) values from ~20 QDs as function of their x, y fitted coordinates on a 160 nm and 400 nm Ag NW in PMMA. To illustrate the propagation length and penetration depth, the extracted normalized individual QDs intensities are separated and plotted as $I(x) = I(x,y)/Nexp(-y/P_d)$ and $I(y) = I(x,y)/Nexp(-x/P_l)$ for **(b)** and **(c)** respectively.. From these fits, SPP propagation length and penetration depth are determined. The x-error bars are from calculated error in PSF fitting. The y-error is determined from uncertainties in our calibration curve (Figure 4.1c). The data point size in **(b)** is larger than the x-error and thus omitted.

The predicted mean and standard deviation of the SPP propagation length and penetration depth where calculated by applying the measured diameter distributions of the Ag NWs (SI Fig-1) to the theoretical diameter dependent propagation/penetration depth functions (Fig 4.5a). Overall, experimentally derived values and theory-derived values agree quite well, as noted in Table I and Figure 4.5. The deviation between theory and experiment is greater for larger wire diameters due to the pentagonal cross-section of the thicker experimental wires vs. the circular wires used in the simulations. Additionally, the spread in SiO_2 penetration depth measurements was due to non-ideality of our sample. The SiO_2 was deposited by vapor deposition leading to surface roughness

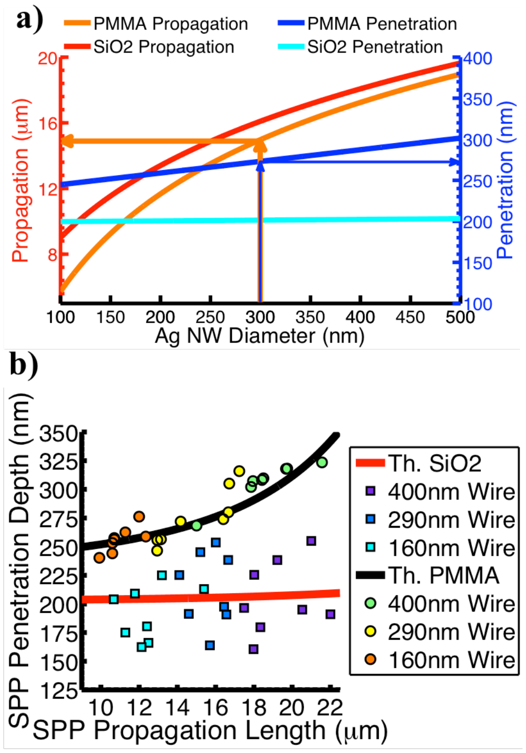

Figure 4.5 | Theoretical and experimental near-field intensity. **(a)** Theoretical calculations of propagation lengths (left y-axis) and penetration depths (right y-axis) as a function of the nanowire diameter. The arrows (orange and blue) give an example for reading the penetration depth and propagation length for a 300 nm Ag NW covered in PMMA. The change in PMMA penetration depth as a function of NW radius is explained in the SI [and SI Figure-4]. **(b)** Comparison of experimental and theoretical penetration depth vs. propagation length values for various wire diameters. The distribution of measured Ag NWs in SiO_2 (square) and PMMA (circle) compare favorably to the theoretical expected values (black and red lines). Additionally, the different sized Ag NWs group together and show the expected trend of increased SPP propagation length and penetration depth for larger wire diameters.

and thickness variations, as well as oxidation of the Ag NWs' surfaces. Regardless, the experimental data shows close agreement to theoretical results.

The experiments clearly demonstrate increase in SPP propagation length for larger wire diameters and for larger refractive index of the surrounding. They also demonstrate increase in the penetration depth as a function of the NW diameter. This latter observation is attributed to the geometries of our samples, as explained in details in SI Fig-4. The larger diameter wire could act as a larger antenna that radiates further into the local environment.

FDTD calculations were used to estimate the error in localizing the QDs (dipole) emitters when in close proximity to NWs. Due to antenna effects, the QD's far-field emission is a superposition of its direct emission plus it scattering off the wire antenna (its mirror charge dipole on the metal surface also radiates into the far-field). The superposition of the direct dipole emission with the scattering from the metallic wire leads to an erroneous PSF localization in the far field. Near-field to far-field scattering simulations were conducted to determine the strength of the electromagnetic coupling of a dipole to a wire antenna and localization errors were quantified (SI Fig-4.5). The near-field to far-field conversion is similar to that used for determining radar cross-sections.[151] The errors associated with this scattering effect were added into the overall localization error bars of Fig. 4.4. (See SI for more details).

Interestingly, our calculated localization error for a QD placed near an Ag NW is smaller than the error calculated (and reported) for a linear dipole.[20] There are two possible reasons for this discrepancy. First, the long Ag NW (as compared to the metallic structures in ref. 23) acts as a waveguide that propagates the coupled QD radiation away from the QD (and hence reduces the scattering component). Second, the in-plane degeneracy of the QD's emission dipole[135, 136] can also reduce scattering (to be further studied in a future work).

4.4. Conclusions

We have characterized the dependence of QDs' stochastic blinking on optical field strength and have shown that the bending parameter Γ can be used to measure SPP field strength. This allowed us to study the dependencies of Ag NWs propagation length and penetration depth on wire diameter and refractive index of the wire's surrounding. FDTD simulations were used to compare theoretical propagation lengths and penetration depth with experimentally derived values. Our theoretical predictions correlate well with the experiments and with known literature values.

COFIBINS offers an exciting sensitive method for detecting plasmonic near-fields using far-field optics. Since QDs blinking can be monitored in the far-field, the method enables the measurement of localized plasmonic near-fields at high throughput using a simple far-field optical set-up. QDs blinking statistics is largely invariant to enhancement and quenching effects, and QDs localization errors are < 15 nm. QDs blinking is therefore an attractive probe that could be utilized for the characterization of plasmonic circuits, nanocatalysts, and solar concentrators.

In future studies we plan to further enhance the resolution of COFIBINS by utilizing polarization to partly decouple the QD dipole from the metallic structures. This will reduce the overall scattering component and will lead to an even higher localization accuracy. Additionally, to completely map the plasmonic near-field with this developed methods requires dense labeling with QD emitters. Superresolution methods that already implement autocorrelation functions of QD emitters, such as SOFI, offer an exciting avenue to achieve this goal. In future studies we plan to incorporate COFIBINS with SOFI to allow complete plasmonic near-field mapping with densely labeled QD plasmonic systems.

4.5. Methods/Experimental

4.5.1. Sample Preparation

First, silver nanowires (Ag NWs) were synthesized using a modified polyol method described previously [152] or bought. The NWs lengths and widths were determined by scanning electron microscopy (SEM). The Ag NWs were measured to have average dimensions of 30 ± 10 μm long with an average diameter of 160 ± 20 nm, 290 ± 30 nm, and 400 ± 50 nm respectively (SI Fig-4.1).

The PMMA NW samples were created according to the following steps: (i) coverslip slides were cleaned by washing with a series of solutions (1.0M KOH, DI-Water, Ethanol, and Acetone) followed by an oxygen plasma cleaning (PDC-32G, Harrick Plasma, Ithica, NY) for 5min; (ii) water-soluble CdSe/ZnS QDs were spincoated in water onto the coverslips to ensure even coverage. The sample was then put on a 100˚C hotplate for 3 min to dry; (iii) a 1wt% solution of poly(methyl methacrylate) (PMMA) in Toluene (an orthogonal solvent to water) was spincoated onto the QD coated coverslip at 8000RPM for 1 min to ensure a dry even 30nm coating of PMMA on the surface. The film thickness of PMMA polymer was measured by scratching the polymer film and imaging the scratch using profilometry (Dektak 150, Veeco, Edina, MN). Samples were further dried on a 100˚C hotplate for 3 min to ensure removal of solvent; (iv) silver nanowires suspended in ethanol were then dried on a PDMS stamp and stamped onto the PMMA surface. Stamping (dry deposition) of the NWs ensures minimal disruption to the PMMA covered QDs; (v) finally, a 3wt% solution of PMMA in toluene was spun at 3000RPM to embed the silver NWs in a well-defined dielectric environment.

The SiO_2 covered NW samples were created according to the following steps: (i) coverslip slides were cleaned in the same fashion as above; (ii) Ag NWs suspended in ethanol were spincoated at 3000RPM for 1 min onto the cleaned coverslip surfaces; (iii) samples (in a container) were rapidly moved into the cleanroom and a 30 nm layer of SiO_2 was deposited *via* electron beam evaporator (CHA solution, Freemont, CA); (iv) during SiO_2 deposition, water soluble QDs were spincoated onto a PDMS stamp and allowed to dry; (v) once SiO_2 deposition was completed, QDs were immediately stamped onto the SiO_2 surface. Stamping of QDs minimized disruptions and provided a uniform QDs coverage on the surface; (vi) finally, a 3wt% solution of PMMA in toluene (an orthogonal solution to the water soluble QDs) was spincoated on the surface to provide the same environment for the QDs in both samples.

4.5.2. Optical measurements

Optical measurements were acquired using a 642 nm continuous wave solid-state laser (Part Number 1150205/AD, Coherent, Wilsonville, OR) for excitation, an XY automated stage (MS-2000, Applied Scientific Instrumentation, Eugene, OR), an inverted microscope (Axiovert S100 TV, Zeiss, Thornwood, NY), a 100x magnification 1.4 NA objective (MPLAPON100XO, Olympus, Waltham, MA), and an EMCCD camera (Model Number DU-897E-CS0-#BV, Andor, Concord, MA). QD fluorescence (at 800 nm) was collected through a 750 nm long pass filter (ThorLabs Inc., Newton, NJ). Movies were recorded with the EMCCD camera. Integration time of 10 ms per frame and total acquisition time of 17 min (100000 frames) were used. Excitation power was determined at the back aperture of the objective using an optical power meter (Model 1830-C, Newport, Irvine, CA).

For the QD field intensity measurements, a lens was added before the side port of the microscope to expand the collimated laser and allow wide-field illumination of the sample. An iris was placed in front of the expanded beam to allow a known area size (625 μm^2) to be illuminated.

For SPP measurements on Ag NW, the laser was focused to a Gaussian spot (FWHM ≈ 500 nm) on one end of the wire. Laser PSF size was determined by focused laser excitation of high density labeled QDs on a glass coverslip and fitting the summed image of the QD emission on the EMCCD camera to a Gaussian. Power was reduced to a minimal level that still allowed QDs excitation (and detectable emission) at the far-end of the Ag NW (typically ~100 W/cm^2).

4.5.3. FDTD Simulations

Electromagnetic simulations were carried out using the finite difference time domain (FDTD) method.[150] The surface plasmon polariton propagation was simulated on Ag NWs of length 20 μm and a diameter varying between 100 nm to 440 nm. The silver NWs were modeled as round cylinders with flat ends: cylindrical NW with a circular cross-section. This assumption is reasonable since the true pentagonal cross-sections have corner modes that hybridize into a symmetric fundamental SPP mode, which is similar to the $m = 0$ mode supported by a cylindrical NW. To model the PMMA coated Ag NWs, the model considered an infinite large dielectric surface with refractive index of $n = 1.542$ for the glass cover slip followed by a 30 nm thick dielectric layer of infinite length and width with refractive index of $n = 1.488$ for the spincoated layer of PMMA. The Ag NWs were positioned on top of this 30 nm PMMA layer. A final infinitely large dielectric layer with refractive index $n = 1.488$ fills in the rest of the modeled box, representing the final layer of PMMA on top of the Ag NW. Similar to the experiment, SPP excitation was done by a 642 nm focused laser beam with spatial FWHM of 321 nm exciting one end of the NW. For the complex dielectric function of Ag, Drude oscillators were used, with response adjusted to the tabulated values of Johnson and Christy.[149] The emitted energy, which leaks from the NW into the surroundings, was analyzed in the plane where the QDs are experimentally: the plane at the SiO_2-PMMA interface, 30 nm below the Ag NW for this sample.

Similarly, to model the SiO_2 coated Ag NWs, again the model considered an infinite large dielectric surface with refractive index of n = 1.542 for the glass cover slip. However, the Ag NW is then directly placed on the glass surface and a 30 nm thick dielectric layer with index of refraction n = 1. 542, representing the deposited SiO_2, surrounds the Ag NW and coats the surface, similar to the experimental geometry. Finally, an infinitely large dielectric layer with refractive index n = 1.488 fills in the rest of the modeled box, representing the final layer of PMMA on top of the SiO_2 covered Ag NW. Again, the plane of the PMMA-SiO_2 interface is monitored. However, this plane is 30 nm above the coverslip, which lies tangent to the Ag NW surface.

Scattering effects were calculated using a near-field to far-field conversion *via* conventional radar cross-sections methods.[151] These results were solely used to calculate the accuracy of localizing a QD near an Ag NW surface. The calculated error in localization is added as error bars to Figure 4. No corrections are made to the experimentally fit localization. See SI for more information.

4.6. Table

		160 nm Ag NW		290 nm Ag NW		400 nm Ag NW	
Dielectric		**Propagation (µm)**	**Penetration (nm)**	**Propagation (µm)**	**Penetration (nm)**	**Propagation (µm)**	**Penetration (nm)**
PMMA	**Experiment**	11.02 ± 0.81	254.8 ± 11.30	15.03 ± 1.90	275.68 ± 24.30	18.59 ± 1.90	306.87 ± 17.08
	Theory	10.37 ± 1.20	252.72 ± 3.15	15.19 ± 0.93	270.45 ± 4.45	17.39 ± 1.07	286.07 ± 8.26
SiO2	**Experiment**	11.92 ± 2.13	198.09 ± 33.48	15.66 ± 0.95	210.74 ± 36.69	20.35 ± 2.78	216.05 ± 49.15
	Theory	11.98 ± 0.89	200±0.29	15.94 ± 0.83	201±0.35	18.01 ± 1.04	203±0.42

Table 4.1. Experimentally extracted values and theoretical values for penetration depths and propagation lengths of different diameter NWs embedded in different dielectric environments (PMMA or SiO_2).

4.7. Supplementary Information

4.7.1 Chemicals/Supplies

Potassium Hydroxide and Poly(methyl methacrylate) (110,000 MW) were purchased from Sigma Aldrich, St. Louis, MO.

Ethanol, Acetone, Toluene, coverslip slides, and water-soluble CdSe/ZnS QDs (Ref Q11071MP Lot# 1454539) were purchased from Thermo Fisher Scientific, Carlsbad, CA.

Silver Nanowire with average diameter 400 nm were purchashed from ACS Materials LLC, Riverside, CA (Product No. AgNw400Eth-0.5g, Lot# 171U14)

4.7.2. Sample Preparation

First, silver nanowires (Ag NWs) were synthesized using a modified polyol method described previously[152] or bought. The NWs lengths and widths were determined by scanning electron microscopy (SEM). The Ag NWs were measured to have average dimensions of 30 ± 10 μm long with an average diameter of 160 ± 20 nm, 290 ± 30 nm, and 400 ± 50 nm respectively (SI Fig-1).

The PMMA NW samples were created according to the following steps: (i) coverslip slides were cleaned by washing with a series of solutions (1.0M KOH, DI-Water, Ethanol, and Acetone) followed by an oxygen plasma cleaning (PDC-32G, Harrick Plasma, Ithica, NY) for 5min; (ii) water-soluble CdSe/ZnS QDs were spincoated in water onto the coverslips to ensure even coverage. The sample was then put on a 100˚C hotplate for 3 min to dry; (iii) a 1wt%

solution of poly(methyl methacrylate) (PMMA) in Toluene (an orthogonal solvent to water) was spincoated onto the QD coated coverslip at 8000RPM for 1 min to ensure a dry even 30nm coating of PMMA on the surface. The film thickness of PMMA polymer was measured by scratching the polymer film and imaging the scratch using profilometry (Dektak 150, Veeco, Edina, MN). Samples were further dried on a 100˚C hotplate for 3 min to ensure removal of solvent; (iv) silver nanowires suspended in ethanol were then dried on a PDMS stamp and stamped onto the PMMA surface. Stamping (dry deposition) of the NWs ensures minimal disruption to the PMMA covered QDs; (v) finally, a 3wt% solution of PMMA in toluene was spun at 3000RPM to embed the silver NWs in a well-defined dielectric environment.

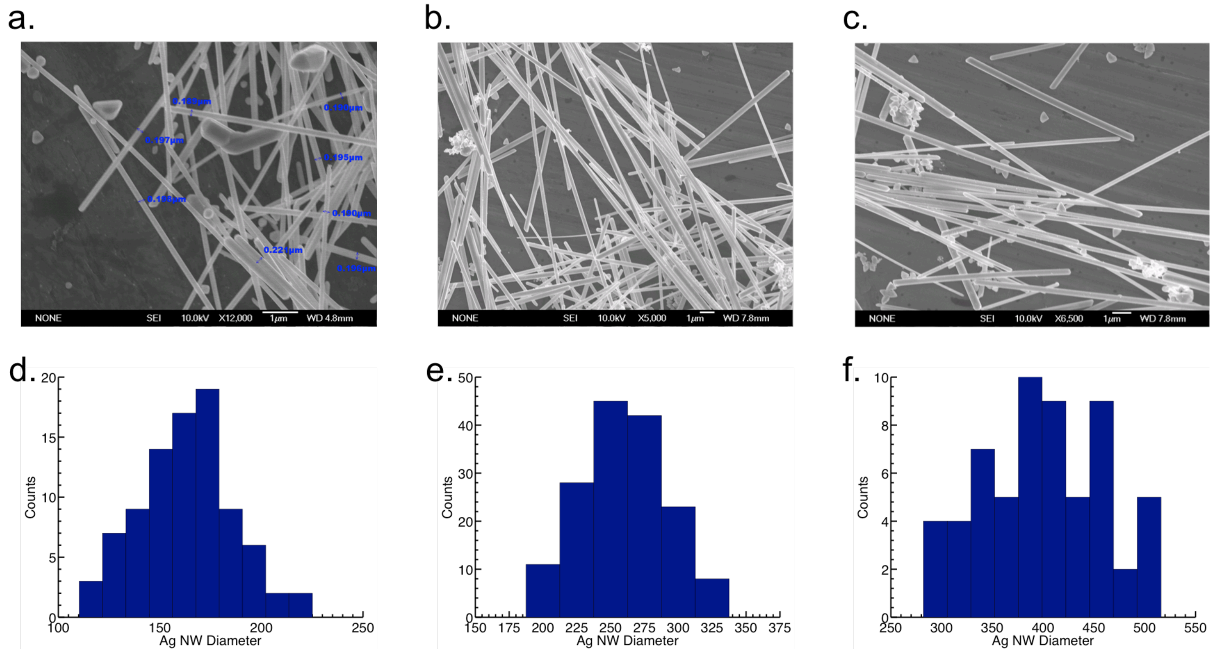

SI Fig-1. (a-c) SEM images of Ag NWs of average diameter 160 nm, 290 nm, and 400 nm

The SiO_2 covered NW samples were created according to the following steps: (i) coverslip slides were cleaned in the same fashion as above; (ii) Ag NWs suspended in ethanol were spincoated at 3000RPM for 1 min onto the cleaned coverslip surfaces; (iii) samples (in a container) were rapidly moved into the cleanroom and a 30 nm layer of SiO_2 was deposited *via* electron beam evaporator (CHA solution, Freemont, CA); (iv) during SiO_2 deposition, water soluble QDs were spincoated onto a PDMS stamp and allowed to dry; (v) once SiO_2 deposition was completed, QDs were immediately stamped onto the SiO_2 surface. Stamping of QDs minimized disruptions and provided a uniform QDs coverage on the surface; (vi) finally, a 3wt% solution of PMMA in toluene (an orthogonal solution to the water soluble QDs) was spincoated on the surface to provide the same environment for the QDs in both samples.

4.7.3. Optical measurements

Optical measurements were acquired using a 642 nm continuous wave solid-state laser (Part Number 1150205/AD, Coherent, Wilsonville, OR) for excitation, an XY automated stage (MS-2000, Applied Scientific Instrumentation, Eugene, OR), an inverted microscope (Axiovert S100 TV, Zeiss, Thornwood, NY), a 100x magnification 1.4 NA objective (MPLAPON100XO, Olympus, Waltham, MA), and an EMCCD camera (Model Number DU-897E-CS0-#BV, Andor, Concord, MA). QD fluorescence (at 800 nm) was collected through a 750 nm long pass filter (ThorLabs Inc., Newton, NJ). Movies were recorded with the EMCCD camera. Integration time of 10 ms per frame and total acquisition time of 17 min (100000 frames) were used. Excitation power was determined at the back aperture of the objective using an optical power meter (Model 1830-C, Newport, Irvine, CA).

For the QD field intensity measurements, a lens was added before the side port of the microscope to expand the collimated laser and allow wide-field illumination of the sample. An iris was placed in front of the expanded beam to allow a known area size (625 μm^2) to be illuminated.

For SPP measurements on Ag NW, the laser was focused to a Gaussian spot (FWHM ≈ 500 nm) on one end of the wire. Laser PSF size was determined by focused laser excitation of high density labeled QDs on a glass coverslip and fitting the summed image of the QD emission on the EMCCD camera to a Gaussian. Power was reduced to a minimal level that still allowed QDs excitation (and detectable emission) at the far-end of the Ag NW (typically ~100 W/cm^2).

4.7.4. Derivation of ACF

Following Verberk and Orrit,[147] we start with the equation for the Laplace transform of the correlation function for a telegraph noise signal from a given probability distribution of on-/off-times (typical of QDs):

$$g(s) = \frac{1}{s}\left[1 - \frac{\epsilon_+}{sT_+} \times \frac{(1-p_+)(1-p_-)}{1-(1-\epsilon_+)p_+ - (1-\epsilon_-)p_- + (1-\epsilon_+-\epsilon_-)p_+p_-}\right] \quad (4.31)$$

where ϵ is the probability of an on/off time to be followed by an off/on time (in our case for alternating on- and off-times, $\epsilon_+ = \epsilon_- = 1$), T_+ is the average on-times, and $p_{+/-}$ is the Laplace transform of the on-/off-time probability distribution function (PDF):

$$L\{f(t)\}(s) = \int_0^\infty f(t)e^{-st}dt \tag{4.32}$$

$$L\{P_{+/-}(t)\} = p_{+/-}(s) \tag{4.33}$$

At low power excitation, the probability that a QD stays in an on/off state follows a perfect power law PDF ($P_{+/-}(t) = t^{-m}$, where t is time in an on/off state and m is the slope of the power law). For the derivation we will add a bending parameter to the on-time to capture the shorter on-times in high power:

$$P_{+}(t) = At^{-m}e^{-\gamma t} \tag{4.34}$$

where A is the normalization constant and γ is dubbed the excitation intensity bending parameter. The off-times have shown to not vary under high intensity excitation and we define it as:

$$P_{-}(t) = Bt^{-m} \tag{4.35}$$

where B is the normalization constant. The power law slope, m, is assumed to be equal for both on-time and off-time PDF.

Solving for p_{+} and p_{-} using equation (4.2) and (4.3) we find:

$$L\{P_{+}(t)\} = p_{+}(s) = \int_0^\infty At^{-m}e^{-\gamma t}e^{-st}dt \tag{4.36}$$

$$L\{P_{-}(t)\} = p_{-}(s) = \int_0^\infty Bt^{-m}e^{-st}dt \tag{37}$$

Here we make assumptions, similar to Verberk and Orrit, that the Laplace transform will be limited by experimental limitations:

1.) The longest possible time in the on or off state is limited by the length of the intensity trajectory (Φ). Thus on/off times greater than Φ is irrelevant.
2.) The shortest possible time in the on or off state is limited by the acquisition of the camera (θ). Thus times shorter than the acquisition time will not be recorded and are thus irrelevant to the correlation function
3.) $\theta \ll \Phi$

Thus the Laplace transform of the probability function, equation (4.6) and (4.7), becomes:

$$p_+(s) = \int_\theta^\Phi At^{-m}e^{-\gamma t}e^{-st}dt \tag{4.38}$$

$$p_-(s) = \int_\theta^\Phi Bt^{-m}e^{-st}dt \tag{4.39}$$

To make equation (4.8) and (4.9) integrable, we consider that the scale of times involved is very broad. Thus we can replace the exponential in the integral by 0 for $t > 1/s$ and 1 for $t < 1/s$ (1/(s + γ) for the on-times):

$$p_+(s) = \int_\theta^{\frac{1}{\gamma+s}} At^{-m}dt = A\left(\frac{(\gamma+s)^{m-1} - \theta^{1-m}}{1-m}\right) \tag{4.40}$$

$$p_{-}(s) = \int_{\theta}^{\frac{1}{s}} Bt^{-m}dt = B\left(\frac{s^{m-1} - \theta^{1-m}}{1-m}\right) \tag{4.41}$$

Now we find the normalization constants A and B. For A:

$$A = \frac{1}{\int_{\theta}^{\Phi} t^{-m}e^{-\gamma t}dt} = \theta^{m-1}\frac{1}{E_m(\gamma\theta)} \tag{4.42}$$

where $E_m(\gamma\theta)$ is the exponential integral:

$$E_m(x) = \int_{1}^{\infty}\frac{e^{-xt}}{t^m}dt \tag{4.43}$$

Assuming $(\gamma\theta)$ is small, due to high acquisition rate of camera and γ varying slowly with excitation intensity, this converges to: $\frac{1}{m-1}$

Thus:

$$A = \theta^{m-1}(m-1) \tag{4.44}$$

For B:

$$B = \frac{1}{\int_{\theta}^{\Phi} t^{-m}dt} = \theta^{m-1}(m-1) \tag{4.45}$$

Combining equation (4.10) and (4.11) with (4.14) and (4.15) we get:

$$p_{+}(s) = 1 - \left((\gamma + s)\theta\right)^{m-1} \tag{4.46}$$

$$p_-(s) = 1 - (\theta s)^{m-1} \tag{4.47}$$

Plugging equation (4.16) and (4.17) into (4.1) we get:

$$g(s) = \frac{1}{s}\left[1 - \frac{1}{sT_+} \times \frac{\left((\gamma + s)\theta\right)^{m-1}(\theta s)^{m-1}}{1 - \left(1 - \left((\gamma + s)\theta\right)^{m-1}\right)(1 - (\theta s)^{m-1})}\right] \tag{4.48}$$

Which simplifies down to:

$$g(s) = \frac{1}{s}\left[1 - \frac{1}{sT_+} \times \frac{1}{\left((\gamma + s)\theta\right)^{1-m} + (\theta s)^{1-m} - 1}\right] \tag{4.49}$$

When inverting the Laplace transform, it is important to determine what term dominates in the denominator. As $t \to \infty$, $s \to 0$. Thus, when $m > 1$, such as with power law, the $(\theta s)^{1-m}$ dominates the function.

Thus we can simplify equation (4.19) to:

$$g(s) = \frac{1}{s}\left[1 - \frac{1}{sT_+} \times \frac{1}{(\theta s)^{1-m}}\right] \tag{4.50}$$

and the inverse Laplace transform of equation (4.20) is:

$$G(\tau) = 1 - \frac{1}{T_+} \frac{\theta^{m-1}}{\Gamma(3 - m)} \tau^{2-m} \tag{51}$$

where $\Gamma(x)$ is a gamma function. To complete the autocorrelation function we calculate T_+, the average on-time. We define the average on-time as:

$$T_+ = \int_0^{\infty} tP_+(t)dt \tag{4.52}$$

Combining equation (4.22) with (4.4), we find:

$$T_+ = \gamma^{m-2}\Gamma(2-m) \tag{4.53}$$

Finally, combining equation (4.23) with (4.21) we derive the autocorrelation function for QD telegraph noise:

$$\boldsymbol{G(\tau) = 1 - \frac{\gamma^{2-m}}{\Gamma(2-m)}\frac{\theta^{m-1}}{\Gamma(3-m)}\tau^{2-m}} \tag{4.54}$$

We simplify this equation in the text and define our autocorrelation function as:

$$1 - G(\tau) = \beta(m)\theta^{m-1}\Gamma^{2-m}\tau^{2-m} \tag{4.55}$$

Where $\beta(m)$ is a numerical function (product of Gamma-functions).

4.7.5. Localization: fitting PSFs with a Gaussian function

Localization of QDs within the captured movie was done in multiple steps. First, all frames in a movie were summed to generate one image. From this summed image, each QD was analyzed in 5x5 pixels and location fit to a 2D Gaussian. Each QD time trace was additionally analyzed to determine if multiple QDs resided within the 5x5 pixel area. Typically the time intensity blinking process is a two state process leading to distributions of high intensity ("on-state") and low intensity ("off-state"). Any time intensity trajectory that showed three distributions of intensity was rejected, as it is most likely two QDs nearby. Future studies will investigate methods to deconvolute QDs at high density.

The precision of determining the centroid location (x_0, y_0) of the PSF was calculated using equation (4.26), derived by Thompson *et al.*[153]

$$Pre_i = \left(\frac{\sigma_i^2}{N} + \frac{a^2}{12N} + \frac{8\pi\sigma_i^4 b^2}{a^2N^2}\right)^{1/2} \tag{4.56}$$

where Pre_i $(i = x \text{ or } y)$ is the x- or y-directional precision of the center position of the PSF, σ_i $(i = x \text{ or } y)$ is the standard deviation from the 2D Gaussian fit, N is the number of photons detected, a is the pixel size of the image (in nm), and b is the standard deviation of the background (in photons).

N, the number of detected photons, is calculated from the summed signal counts over all the pixels falling under the 2D Gaussian fit (in our case 5x5 pixels) in the EMCCD camera using the following equation:

$$E_v = \left(\frac{cts}{g}\right)\left(\frac{S}{QE}\right)(3.65) \qquad 4.(57)$$

where E_v is the total energy of photons per pixel, cts is the number of counts (per pixel) detected, g is the amount of electron multiplying gain applied, S is the CCD sensitivity, QE is the quantum efficiency of the camera at the average QD emission wavelength (800nm), and 3.65 is a physical constant for electron creation in silicon.[154]

The image pixel size, a, was calibrated by imaging a micrometer *via* white light wide field illumination.

4.7.6. Determining Perpendicular Distance from Ag NW

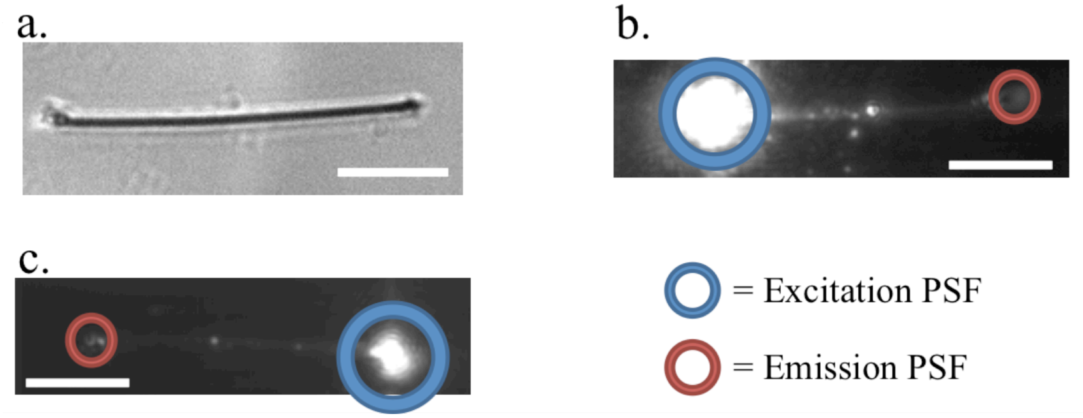

SI Fig-2. The location of the Ag NW relative to the QDs was determined by exciting either end of the Ag NW with a 642nm CW laser. The emitted scattered light PSF at either end of the Ag NW was then fitted with a 2D Gaussian. The wire center is then assumed to be the straight line between the centroid of the fitted Gaussians. An example is given with the Ag NW above. Ag NW in **(a)** bright field, **(b)** excited on the left, **(c)** excited on the right. All scale bars are 7μm.

4.7.7. FDTD Simulations

Electromagnetic simulations were carried out using the finite difference time domain (FDTD) method.[150] The surface plasmon polariton propagation was simulated on Ag NWs of length 20 μm and a diameter varying between 100 nm to 440 nm. The silver NWs were modeled as round cylinders with flat ends: cylindrical NW with a circular cross-section. This assumption is reasonable since the true pentagonal cross-sections have corner modes that hybridize into a symmetric fundamental SPP mode, which is similar to the $m = 0$ mode supported by a cylindrical NW. To model the PMMA coated Ag NWs, the model considered an infinite large dielectric surface with refractive index of $n = 1.542$ for the glass cover slip followed by a 30 nm thick dielectric layer of infinite length and width with refractive index of $n = 1.488$ for the spincoated layer of PMMA. The Ag NWs were positioned on top of this 30 nm PMMA layer. A final infinitely large dielectric layer with refractive index *n* = 1.488 fills in the rest of the modeled box, representing the final layer of PMMA on top of the Ag NW. Similar to the experiment, SPP excitation was done by a 642 nm focused laser beam with spatial FWHM of 321 nm exciting one end of the NW. For the complex dielectric function of Ag, Drude oscillators were used, with response adjusted to the tabulated values of Johnson and Christy.[149] The emitted energy, which leaks from the NW into the surroundings, was analyzed in the plane where the QDs are

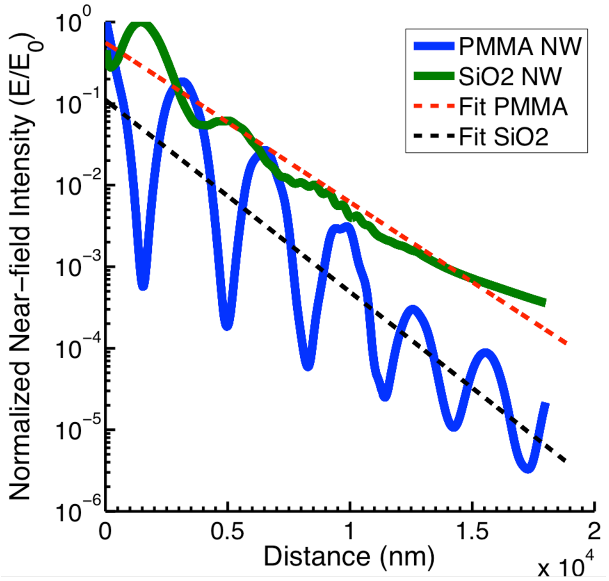

SI Figure-3. Example propagation FDTD simulations for a 400 nm diameter Ag NW excited by a focused 642 nm CW laser in either SiO_2 or PMMA (see text for full dimensions of simulation). The length of the NW was 20 μm. The first 1.0 μm is not shown because the intensity is dominated by the excitation Gaussian. The fit propagation length was determined to be 17.39 μm experimentally: the plane at the SiO_2-PMMA interface, 30 nm below the Ag NW for this sample.

Similarly, to model the SiO_2 coated Ag NWs, again the model considered an infinite large dielectric surface with refractive index of *n* = 1.542 for the glass cover slip. However, the Ag NW is then directly placed on the glass surface and a 30 nm thick dielectric layer with index of refraction *n* = 1. 542, representing the deposited SiO_2, surrounds the Ag NW and coats the surface, similar to the experimental geometry. Finally, an infinitely large dielectric layer with refractive index *n* = 1.488 fills in the rest of the modeled box, representing the final layer of PMMA on top of the SiO_2 covered Ag NW. Again, the plane of the PMMA-SiO_2 interface is monitored. However, this plane is 30 nm above the coverslip, which lies tangent to the Ag NW surface. SI Fig-3 and SI Fig-4 show example propagation length calculations and penetration depth calculations respectively.

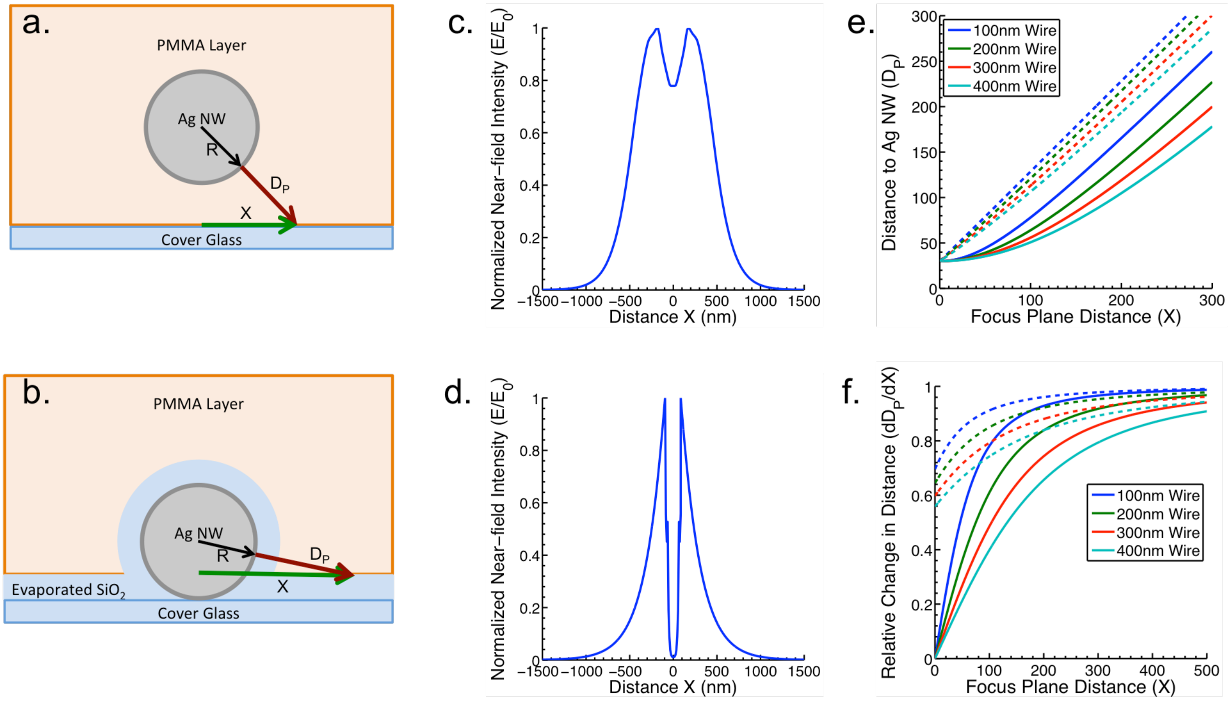

SI Figure-4. (a-b) Geometric representation of distance perpendicular to the Ag NW in the focal plane (X) *versus* the actual distance (D_P). R is radius of the Ag NW. **(c-d)** FDTD simulations of the evanescent wave penetrating into the surrounding media. The dip in the middle in **(c)** is due to total reflection (similar to TIRF). At a large incident angle (90˚ to surface normal), the evanescent SPP field is likely to be transmitted through the PMMA-SiO_2 boundary. At smaller angles, the evanescent wave can reflect off the SiO_2-PMMA interface, increasing the effective field strength. **(e)** Conversion of perceived distance *versus* actual distance for PMMA samples (solid lines) and SiO_2 samples (dashed lines). PMMA samples vary slowly compared to the SiO_2 counterpart. **(f)** The relative change in distance as a function of position-X (dD_P/dX) for PMMA samples (solid lines) and SiO_2 samples (dashed lines). SiO_2 samples converge rapidly to a 1:1 ratio dD_P to dX compared to the PMMA sample.

Since the geometry between the samples are different, due to sample preparation, the propagation length and penetration depth should differ. The main text talks about the results, e.g. larger propagation length and smaller penetration depth for the SiO_2 coated Ag NW and opposite for the PMMA coated Ag NW. However, the peculiarity of the penetration depth changing as a function of Ag NW size for PMMA coated Ag NWs is further detailed here. The penetration depth is related to the electric field perpendicular to the surface of the Ag NW. Traditionally, this is defined as $k_i = \frac{\omega}{c}\sqrt{\frac{\epsilon_1^2}{\epsilon_1+\epsilon_2}}$. Since ϵ_1 and ϵ_2 do not change, this should be constant. However, the perceived distance perpendicular to the Ag NW is not the actual distance. To correct for this, a simple geometric conversion is needed (SI Figure-4). The conversion shows the actual distance from the Ag NW (D_p in SI Fig-4a) varies more slowly than the perceived distance from the Ag NW (X in SI Fig-4a) for PMMA covered NWs. SiO_2 covered NWs vary drastically less. Additionally, as the radius of the NW increases, this effect becomes more pronounced. This explains the perceived increase in penetration depth as a function of Ag NW radius.

Scattering effects were calculated using a near-field to far-field conversion *via* conventional radar cross-sections methods.[151] The results are summarized in SI Figure-5. These results were solely used to calculate the accuracy of localizing a QD near an Ag NW surface. No corrections are made to the experimentally fit localization. An Ag NW of length 6 μm and radius 100 nm was modeled with air as the surrounding medium (n = 1.0). A dipole source of varying polarities ($x, y,$ or z) was placed at varying distances between 10-100 nm away from the Ag NW surface (radial direction) at the center, at a quarter length of the wire, or at the edge of the wire to test how the presence of the metallic surface affects the far-field PSF fitted position (SI Figure-5a). The dipole oscillates at a frequency corresponding to 800 nm with a wavelength FWHM of 10 nm. The generated far-field radiation was then collected and analyzed similar to microscopy methods. When an emitter radiates into the far-field, not all photons can be collected from a microscope objective. Airy disks appear in the image as a result of the missing photons. Limitations such as objective distance from the emitter and size of the objective lens is taken into account in modeling to reproduce the Airy disks. The specs of a 100x Olympus 1.4 NA objective are working distance of 0.12 mm and lens diameter of 6.6 mm. Thus the Olympus objective can only receive photons emitted from the focal plane within an angle of 87.9˚ perpendicular to the surface. Example generated images are shown in SI Figure-5b-d. The modeled PSF was then fit with a 2-D Gaussian to acquire the theoretical perceived location of the QD.

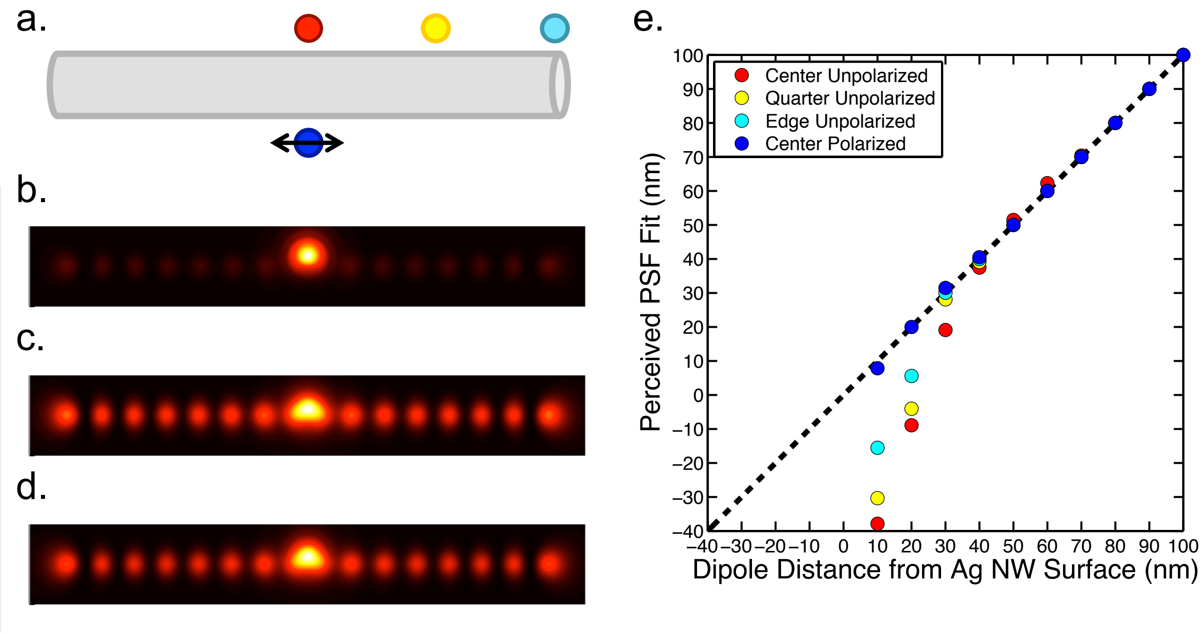

SI Figure-5. (a) Cartoon representation of QD location at the center (red), quarter (yellow), and edge (teal) of the Ag NW. The QDs at these locations are simulated as isotropic dipoles, meaning the scattered image from an x-polarized, y-polarize, and z-polarized dipole are summed. The center polarized dipole (blue) is polarized parallel (x-polarized) to the long axis of the Ag NW. Scattered image of an **(b)** x-polarized, **(c)** y-polarized, and **(d)** isotropic dipole coupling with an Ag NW 30 nm from the surface. The length of the simulation box is 7 µm x 1 µm and Ag NW 6 µm x 100 nm. **(e)** Compiled data for QDs at varying distance from the Ag NW surface at different locations. The black dashed line shows $x = y$ (no mislocalization) curve. We see clear mislocalization for unpolarized QDs within 40 nm of the metallic surface, the largest error attributed to a QD placed at the center of the wire. Surprisingly, if the QD dipole emission is polarized along the long axis of the Ag NW, the error in localization is significantly reduced. All experimental QDs are at least 30 nm away from the Ag NW due to a buffer layer of PMMA or SiO$_2$, leading to a maximum error of 10 nm in localization due to scattering effects.

Chapter V: Overcoming Emitter Misslocalization due to Plasmon Scattering

5.1. Introduction

Superresolution imaging of emitters on a plasmonic system has been tried before. For example, Stranahan and Willets studied surface enhanced Raman spectroscopy hot spots [155]. However, resolving densely packed emitters near a metal surface with superresolution techniques is difficult, as mentioned above [20, 156]. Typically, the resulting mirror charge generated by a dipole can scatter from the metallic structure. The measured far-field PSF that originates from the direct emission of the probe plus its scattering from a near-by metallic structure could give rise to localization errors of few tens of nanometers [20].

One of the more exciting uses of QDs is to potentially overcome or at least alleviate the distorted PSF of the emitters due to their dipole coupling into nearby metallic structures. There have been attempts to deconvolute the direct emission and near-field scattering contributions using *a priori* knowledge of the plasmonic system [156], but current attempts fail at capturing the full scattering effect leading to inaccuracies.

Here, instead, we propose to modulate the emitter coupling to the metallic structure, so a more accurate PSF will be back-calculated and a more precise localization will be achieved. Using polarization modulation, it should be possible to modulate the coupling between the QDs and the plasmon dipole moments and hence reduce or enhance their coupling. In addition, quantum confinement can be used to tune the QD absorption and emission away from the plasmon resonance, allowing for further reduction in their coupling, and therefore reduction in the scattered field.

Specifically, the effect of polarization is theoretically demonstrated in Fig. 6.1. Here we calculate with FDTD a dipole 10 to 100 nm away from a 100 nm diameter by 6 μm length silver nanowire. Only the E_y dipole couples into the nanostructure from the QD next to a metallic wire oriented in the x-direction. The E_x and E_z dipole show little to no coupling and can be accurately localized when the dipole emits into the far-field. Thus a two-step measurement is proposed: a measurement to index the apparent location of QDs together with extraction of local near-field intensity, followed by localization measurements with a modulated linearly polarized light (at several different polarization angles). By measuring the shifts in the localization coordinates as function of the excitation polarization angle, we will be able to estimate the accurate coordinates by separating emission and scattering contributions.

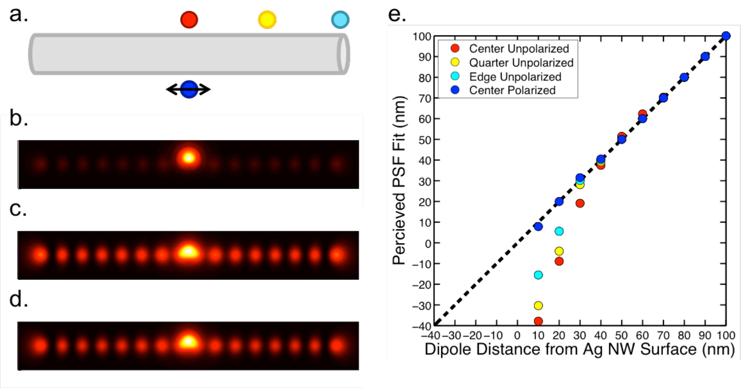

Fig. 5.1: **(a)** Schematic QD location at the center (red), quarter (yellow), and edge (teal) of an Ag NW. The QDs are simulated as isotropic dipoles, while the center polarized dipole (blue) is x-polarized, parallel to the long axis of the Ag NW. Scattered image simulate an **(b)** x-polarized, **(c)** y-polarized, and **(d)** isotropic dipole coupling with an Ag NW 30 nm from the surface. **(e)** Compiled data for QDs at varying distance from the Ag NW surface at different locations. The $x = y$ dashed line is for no mislocalization. Clear mislocalization is seen for unpolarized QDs within 40 nm of the metallic surface, especially for a QD near the wire center. In an **x**-polarized QD, localization error is significantly reduced.

Polarization experiments will study the electromagnetic coupling strength of the plasmonic nanostructure and the QD. Generally, a QD has a degenerate in-plane dipole so it has no preferred direction. Only when the QD is placed in a strong electric field, such as a plasmonic field, will the dipole partially polarize with the field [157]. Thus a QD can be excited indiscriminately at any excitation polarization angle. The same phenomenon is not true for the plasmonic systems which are generally not spherical. Depending on the underlying nanostructure, different resonances appear upon polarization excitation. The "hotspots", i.e., areas of large near-field intensity, are polarization dependent and can therefore be selectively excited.

By changing the polarization, the hotspots will move or change in intensity. Depending on the location of the QD and the angle of its distance vector from the metallic structure relative to the polarization, the QD will be polarized to a lesser or greater extent, and therefore the PSF distortion will change (and be minimal when the distance vector and polarization are perpendicular). We will therefore calculate PSF trajectory maps which indicate the changing position and intensity of the PSF, from which we will aim to backtrack the true coordinates. One of the main goals of the proposed research will be to find out how accurate this backtracking is.

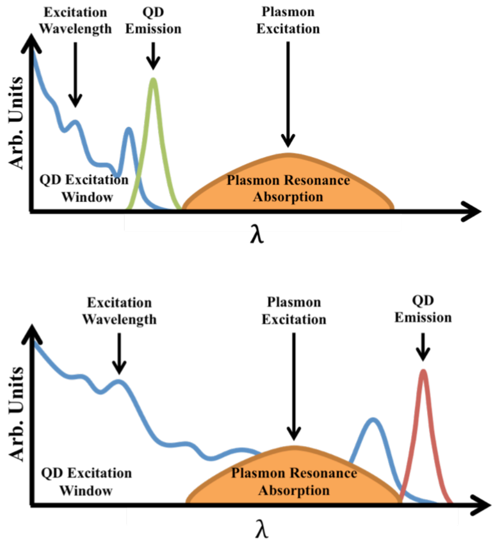

Fig. 5.2: Representative spectra of QD excitation/emission and plasmon absorption. **(Top)** QD excitation and emission below the plasmon absorption, compared to **(Bottom)** QD excitation below the plasmon absorption but with QD emission in the far-red emission.

Experimental characterization of the PSF distortion as a function of polarization will be carried out on intelligently designed plasmonic systems. "Ideal" initial systems, such as 50 nm width and 500 nm length ‘L’-shaped and crescent moon silver nanostructures, will be lithographically constructed into an array. QDs will be randomly distributed through spincoat methods at low densities. Wide-field illumination of changing linearly polarized light will then excite the sample and the PSF localization values histogrammed to get a distribution. Experimental variables such as structures features, plasmon resonance frequency, and QD-surface distance will all be characterized.

Another method to modulate the electromagnetic coupling of QD to metallic surfaces is to separately excite the QDs and the plasmons. Due to the tunability of QDs emission by quantum confinement and due to their wide, semi-continuous absorption spectrum, it is possible to separately excite the plasmons in the red part of the spectrum and the QDs in the blue part of the spectrum, and minimize the scattering of quantum dot emission from metallic structures. We will fix the plasmon resonance (fixed diameter silver nanowire or sphere) and use QDs of various sizes and tunable excitation to explore the scattering effect on the localization accuracy and field sensitivity. In particular, two bands will be selected to separately excite blue/green QDs with a blue band excitation and plasmons with red light. Alternatively far-red QDs will be excited with blue light and both QDs and plasmons with red light. Fig. 6.2 shows the absorption and emission spectra of the QDs, the plasmon resonance, and the two excitation bands for either case.

The shift in PSF localization will be studied as a function of QD excitation and emission and the plasmon resonance. We will also fabricate arrays of nautilus-esque shell metallic structures with varying plasmon resonances. By varying the width of the plasmonic structure as a function of distance, different resonances should occur. Thus, by tuning the plasmon excitation frequency, the PSF localization will shift.

The preliminary results led to the exciting prospect of using QDs as far-field superresolution detectors of plasmonic near-fields. However, our method requires rigorous validation. The experiments detailed above, as well as theoretical studies explained next, will validate the approach.

5.2. Polarization/Spectral Modulation

In order to quantify the aberrant localization of an emitter in close proximity to a metallic structure, we are developing three approaches to modulate and analyze their coupling: (i) use QDs with emission that is on- or off- the plasmon resonance; (ii) modulate the polarization of the excitation laser; (iii) analyze the polarization of the emission + scattering of the combined emitter/metallic structure system in the far-field. Quantification of the emitter's PSF distortion by the metallic structure requires a well-defined system with ideal properties: clear plasmon resonance peaks and polarization dependent resonances in the visible spectrum. Extensive Finite domain time difference (FDTD) calculations were performed in search for an ideal structure shape and material for the electromagnetic coupling studies. We have identified an L-shaped gold nanostructure with 200 nm arms lengths and 50 nm width as the optimal structure. Such structures are currently being fabricated using e-beam lithography.

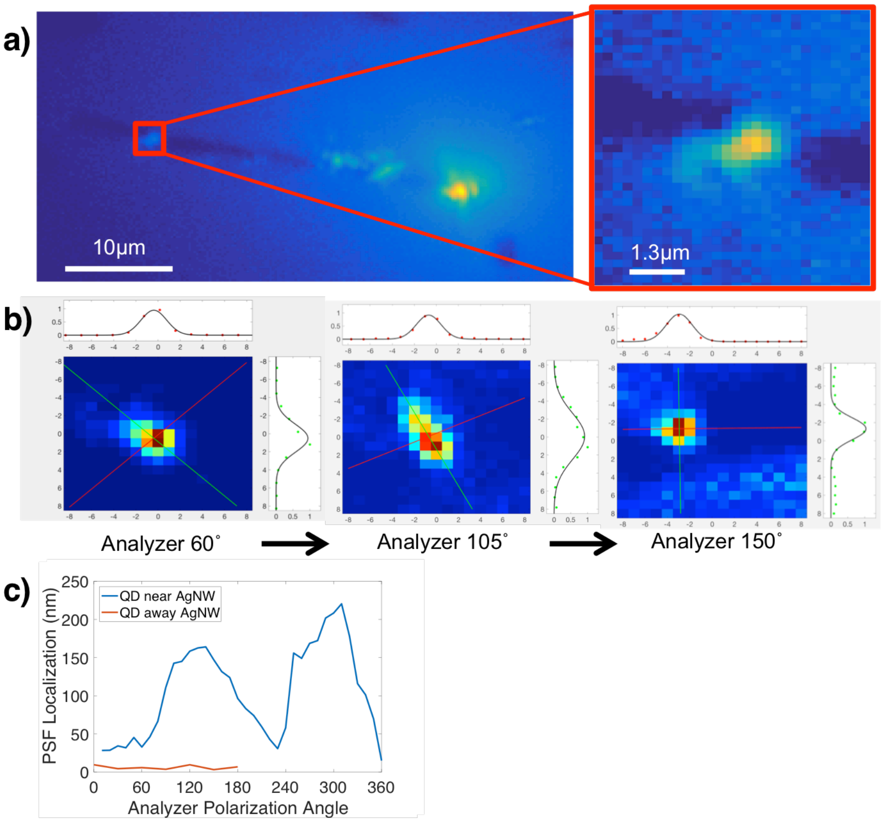

Fig. 5.3: Polarization effects on PSF localization. (a) Plasmon polaritons were excited in a AgNW by a 642nm CW laser at its right end (right bright spot in left panel). Emission from a single QD near (<50nm) the AgNW (red box in left panel and zoom-in in right panel) was imaged onto an EMCCD camera. **(b)** The QD's emission was analyzed with a polarization analyzer while localizing its PSF (3 angles shown). The localization changes with polarization as the analyzer is able to discriminate plasmon-coupled and plasmon-uncoupled emissions. **(c)** A full 360^{o} polarization modulation shows a periodicity in localization (blue curve). PSF localization 2D Gaussian fitting is referenced to an arbitrary point - the center of the zoomed-in FOV). A QD located far (>1μm) from the AgNW (red curve) shows no modulation in localization.

We have started with approach (iii) first. The plasmon-distorted PSF was analyzed by a polarized analyzer. Previous published works and our own simulations show that PSF distortion depends on the emitter's dipole orientation. An emitter that interacts strongly with the metallic structure has a larger PSF distortion, while a weak interaction leads to minimal distortion. When an emitter dipole is perpendicular to a metallic surface, the coupling is strong, leading to strong scattering. When the emitter dipole is parallel to the surface, the coupling is weak, leading to weak scattering. To test this, we have introduced a polarization analyzer in the emission path and are able to see change in PSF localization as a function of polarization. Due to QD's dipole degeneracy in the plane of excitation, we can discriminate between different dipole orientations via the rotation of the analyzer angle in the emission path. (see Fig. 5.3 for more details). Extensive FDTD simulations have also been used to simulate emitter PSF close to metallic systems to further verify and quantify this effect (Fig. 5.4).

We also plan to discriminate between different excitation dipole orientations via polarization modulation of the excitation beam (approach (ii)). We have recently introduced zero-order half waveplate and polarization beam splitter into the excitation beam and are currently acquiring such data.

For approach (i), we intend to select different-size QDs to match/mismatch the plasmon resonance of our ‘L-shape’ metallic structures (200 nm) (Fig. 6.4). We also plan to use dual emission QDs with one emission on-resonance and one emission off-resonance. We acquired Mn^+ doped CdS QDs that obey this requirement for the ‘L-Shaped’ structures. These measurements are currently ongoing.

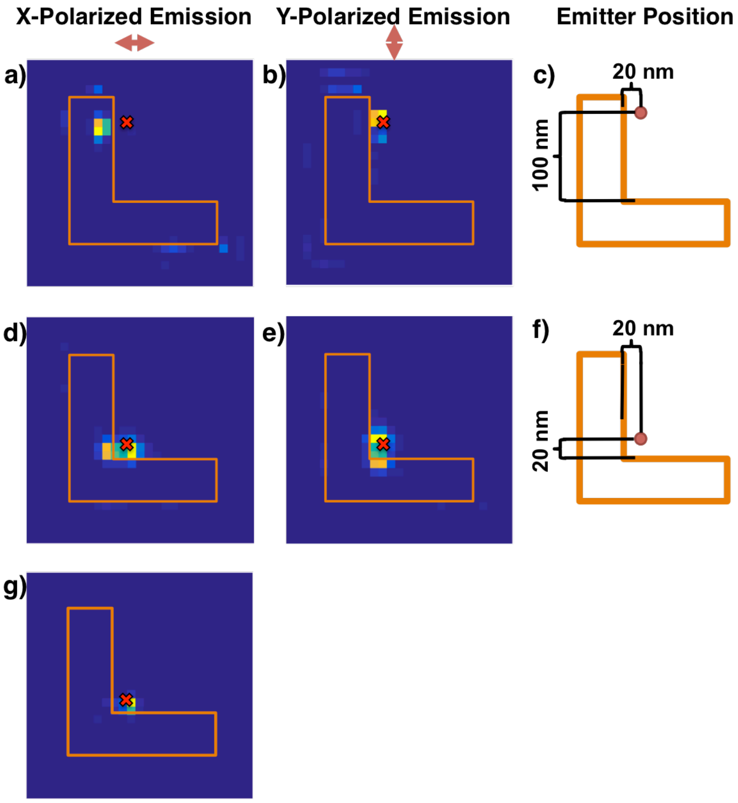

Fig. 5.4 FDTD Simulations of Optimized Lithographic Sample. Dipole emitters close to a “L-shaped” metallic nanostructure (200nm arms with 50nm width) was modeled using FDTD simulations. A (very) small subset of calculations are shown to illustrate PSF distortion with x-polarized emission **(a,d,g)** and y-polarization emission **(b,e)** at different locations of the “L-shaped” nanostructure. The image is scaled to highlight the most probable emission localization. On-resonance emission **(a,b,d,e)** and off-resonance emission **(g)** is also investigated. Modeled emitter location is noted with a small red “X” and with the models on the right **(c, f)**.

CHAPTER VI: Superresolution Techniques

6.1 Introduction

Stochastic QDs switching between ‘on’ (high emission rate) and ‘off’ (low emission) is also known as ‘intermittency’, or ‘blinking’ [130-133]. It is well-studied [130, 133, 137, 138, 146, 158-160]. Auger recombination is commonly invoked [140-142], but surface and heterointerface charge trapping also contribute to switching [143, 144, 161].

In detecting switching, Emission from a single QD is recorded in time bins; histograms are constructed for the ‘on’ and ‘off’ periods. At low excitations, the histograms exhibit nearly a perfect power law distribution for both the ‘on (+)’ and ‘off (-)’ periods, $P_{+/-}(t) = t^{-m}$ [130, 131]. At higher excitations, the ‘on’ time distribution bends at long ‘on’ times, $P_{+} = t^{-m}e^{-\Gamma t}$; Γ is the intensity bending parameter which is linear in the excitation intensity (Fig. 1) and we therefore propose to use Γ for field mapping.

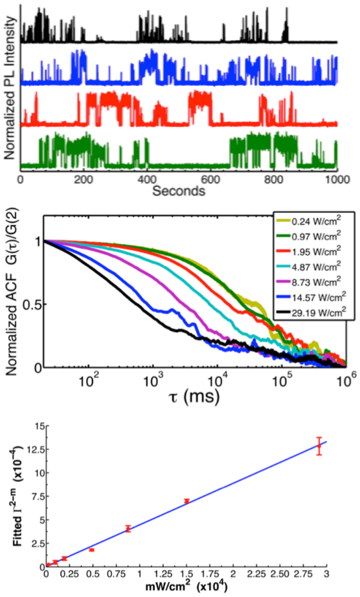

Fig. 6.1: (Top) Intensity vs.power for single quantum dot under a 642nm CW laser. **(Center)** Averaged normalized ACF, decaying faster at higher powers due to shorter on lifetimes. **(Bottom)** Lifetime bending parameter Γ from $1 - G(\tau) = \beta(m)\theta^{m-1}\Gamma^{2-m}\tau^{2-m}$.

We propose to position multiple QDs in close proximity to metallic structures that constitute a plasmonic device and record with an EMCCD camera their far-field emission time-trajectories using conventional diffraction-limited wide-field optics. Initially, sparse isolated QDs will characterize the perturbation of a QD’s PSF in close proximity to a metallic surface.

Next, a high emitters' density will be used for superresolution (sub-diffraction) maps of plasmonic fields.

A variant of superresolution optical fluctuation imaging (SOFI) methodology [162-164] will be used (using higher areal density of QDs, > 30 QDs per mm^2 and pixel-based cumulant analysis rather than localization based analysis). In SOFI, high order cumulants are calculated for each pixel in field-of-view (FOV). An image constructed from fitted bending parameters for each pixel's cumulate could map the localized electric field and superresolve the underlying features of the plasmonic circuit (see below).

Initially we repeated others' blinking experiments but instead of histogramming on/off times, we autocorrelated the time trajectory of each QD, as histogramming can lead to a 15-30% bias in the interpretation of data depending on background noise and binning of photons [139]. The 'bending parameter' Γ was analyzed as a function of excitation intensity [147]. An analysis analogous to Refs. [147, 165] shows that the normalized autocorrelation function (ACF) is: $1 - G(\tau) = \beta(m)\theta^{m-1}\Gamma^{2-m}\tau^{2-m}$ where m is the slope of the on/off-time probability distribution, known to be ≈ 1.4, and θ is the minimum capture window, 10 msec here; $\beta(m)$ is a numerical function of m. Thus, we only need to fit Γ.

Fig. 6.1 shows compiled results from 30 CdSe/ZnS core-shell QDs, excited at 642 nm with a continuous wave (CW) laser and measured at 800 nm. The average normalized ACF, compiled from the ACF of individual QDs decays faster at high powers due to shortened 'on' times. Γ is linear in the intensity as previously reported using different methods [148, 166]. Fig. 6.1 therefore presents a calibration method for determining the excitation intensity from the blinking behavior of individual QDs.

We mapped out the propagation lengths and penetration depths of plasmonic waveguides for silver nanowires of different diameters (160, 290, 400nm), and various lengths (~20-40μm). Wires were over-coated with either a 30nm thick SiO_2 or poly(methyl methacrylate) (PMMA) layer to test the dependence on the environment's dielectric constant.

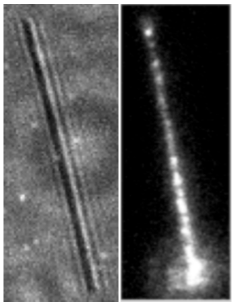

Fig. 6.2: Silver nanowires, 0.2μm x 20 μm , coated in QD under (**Left**) bright field illumination and (**Right**) confocal excitation at the bottom.

Initially a low density of QDs was used (~1.8 QDs/mm^2). When excited at one end of the silver nanowire, the plasmonic field should exponentially decay along (propagation) and away from (penetration) the wire (Fig. 6.2). The location of each QD is extracted with spatial accuracy of ~20 nm by fitting a 2D Gaussian to the PSF. Accuracy was determined from fitting experimental data with a known background plus calculated maximum error due to scattering from a dipole near the Ag NW surface (modeled with FDTD). We dub this approach as COFIBINS (**C**haracterizing **O**ptical **F**ield **I**ntensity by **B**l**i**nking **N**anoparticle**S**)

We propose to increase the QDs density, thereby increasing throughput and achieving true superresolution imaging of plasmonic fields. Below we discuss plans to automate this algorithm to handle a large number of blinking QDs in a wide FOV. Our proposed method will enable the study of plasmonic features well below diffraction limit. To be competitive with other methods, we need to improve our spatial resolution. We will use our established superresolution tool SOFI [162, 164] to localize/map high density of QDs. This superresolution technique already uses QD-blinking to spatially resolve features at high density (larger than commonly used in localization microscopies). We recently developed a method to extract photo-physical properties of QDs at high labeling densities, a crucial development for the proposed work.

In SOFI, the temporal autocorrelation amplitude of pixels with signal contribution from both QDs is lower than the autocorrelation amplitude of pixels with signal contribution from only one of the two QDs, yielding an image with a dip between the two QDs. In applying SOFI to our method, a new type of SOFI will emerge, coined moca-SOFI for **m**ulti-**o**rder **c**umulant **a**nalysis-SOFI. This version will allow us to calculate Γ, and hence the plasmon intensity, at each pixel. This method is outlined in Fig 6.3a. Briefly, the fluctuation signal within a given pixel will depend on the emitter PSF, emitter brightness, and its fluctuation profile, which contains an “on-”/”off-time” ratio. By combining the information from different orders of cumulants, one can construct a system of equations to relate “on-time” ratio to Γ

$$\frac{\mathit{average\ on\ time}}{\mathit{average\ off\ time} + \mathit{average\ on\ time}} = \frac{\int_\theta^\infty tP_+(t)dt}{\int_\theta^\infty tP_-(t)dt + \int_\theta^\infty tP_+(t)dt} = \frac{\Gamma^{2-m}\beta}{\frac{\theta^{2-m}}{2-m} + \Gamma^{2-m}\beta}$$

We will use moca-SOFI implementations such as auto-correlation SOFI, nearest (pixel) neighbor cross-correlation SOFI [163], and high order SOFI and explore their performance for accurate plasmonic field mapping and the achievable resolution at high QDs density.

For eventually applying superresolution methods for accurate localization of densely distribution of QDs, we will need to optimize the QD deposition procedure and investigate the limits of moca-SOFI. Higher densities of QDs for superresolution applications have an inherent Goldilocks region: greater density leads to better mapping but too high a density leads to breakdown of superresolution methods. Thus optimal density conditions will be sought. Methods such as increasing concentration of QDs during spincoating and chemically functionalized QDs binding will be explored. We will optimize a protocol to allow selective placement of QDs directly on a metallic surface using molecular recognition and covalent chemistries (such as DNA hybridization, thiol-based and click chemistries, etc.). Selective placement of QDs would allow better localization due to a lower background caused by nonspecific binding of the QDs. This would give a more dependable way of depositing QDs

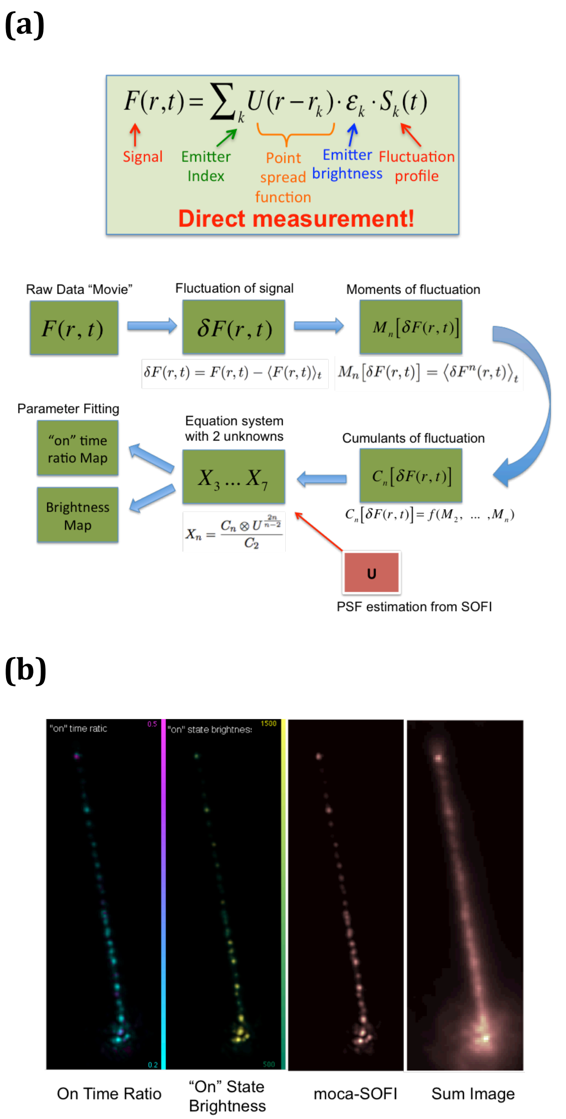

Fig 6.3: (a) Roadmap of extracting emitter parameters (on time ratio and emitter brightness) from raw movie. **(b)** Preliminary test of a sparsely labeled silver nanowire illuminated at the bottom by a confocal laser (same as Fig. 3). We see clear localization of the individual QDs compared to the sum image. Brightness and "on time" ratio shows expected trends as a function of distance along the nanowire.

on the surface rather than a random distribution as in spin-coating. The obvious downsides would be a stronger interaction of the probe with the plasmon field thereby altering it, and larger difficulty in removing the QDs (if further processing or analysis is needed).

Our initial implementation of moca-SOFI shows promise for simultaneous field intensity extraction with the $1/\sqrt{n}$ spatial resolution enhancement factor; n is the SOFI order, typical of SOFI analysis[162]. However, we need to investigate our method's limitations such as large electromagnetic field gradient, time resolution, and dynamic range. Optimization will be made by simple simulation of fake QD emitters with generated intensity trajectories and using known blinking profiles, spread along a plasmonic system of simulation. FDTD simulations will dictate the fields experienced by these fake QDs, and therefore their intensity trajectories and PSF profile. The emission profile, generated as a movie, will be analyzed by moca-SOFI and the errors in the output compared with the preassigned locations will yield a measure of the method's accuracy. We will use this information to optimize under what conditions moca-SOFI best performs. The optimized conditions will guide our experimental protocol and what we learn from our experimental measurements will help optimize our theoretical simulations and moca-SOFI analysis.

6.2 SOFI Integration Results

To achieve true superresolution images of plasmonic near-fields, we need to utilize a method that can extract the Γ-parameter at high emitter density. The initial method [167] used sparse QDs labeling along the plasmonic wires. Each QD was spaced far apart so an isolated time-intensity trajectory could be accurately fit to the derived autocorrelation function. From these autocorrelation functions the Γ-parameter (and hence on/off ratios) were extracted. More recently, we have implemented a modified version of our superresolution optical fluctuation imaging (SOFI, MOCA, Yi et al., under preparation) to extract the Γ-parameter of high QDs density. These results are illustrated in Figure 6.4 and Figure 6.5. We drop-casted a concentrated solution of QDs onto an AgNW. Upon confocal excitation of the SPPs at one end of the wire (642nm CW laser), the QDs excite and emit (800nm) downstream due to the SPP's evanescent field. Figure 3a shows the average (sum image) of 10k acquired frames. If we extract

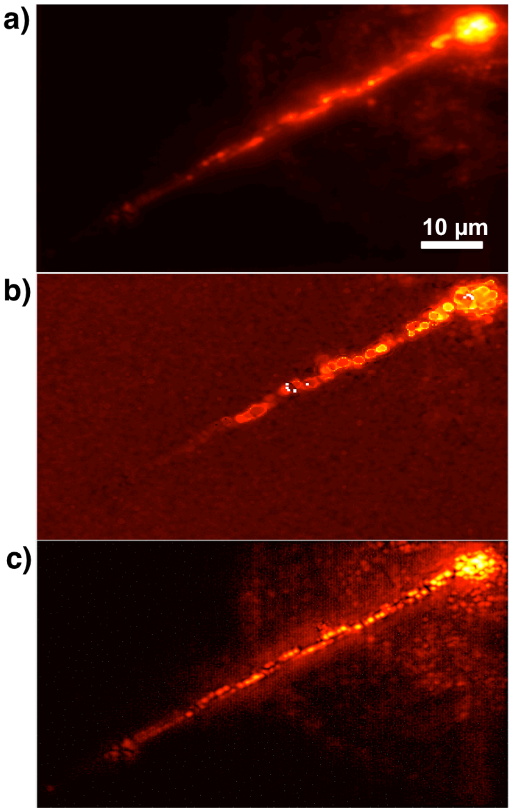

Fig. 6.4: Dense QD labeling of AgNW. QDs were drop-casted on glass converslip containing randomly oriented AgNWs. SPPs were excited with a confocal 642nm CW laser at one end of AgNWs (top right of each image). The SPPs evanescent field excites the QDs downstream the wire. **(a)** Average pixel intensity. **(b)** Pixel-by-Pixel extraction of QD on-off ratio from autocorrelation function (Γ-parameter) via COFIBINS. **(c)** QD on-off ratio extraction via MOCA-COFIBINS. All heat-maps are log scale (to allow visualization of the plasmon propagation exponential decay).

the on-off times pixel-by-pixel, similar to the COFIBINS method (when performed on isolated emitters), we get qualitatively a correct "smear", but we lose spatial resolution (Figure 3b). QDs with overlapping PSF can contribute to the same pixel, leading to this expected result. If, however, we use SOFI in combination with Multi-Order Cumulant Analysis (MOCA, Yi et al., under preparation), the contributions of multiple emitters to a single pixel can be separated out using information from higher orders cumulants (Figure 5). We dub this combination method MOCA-COFIBINS.

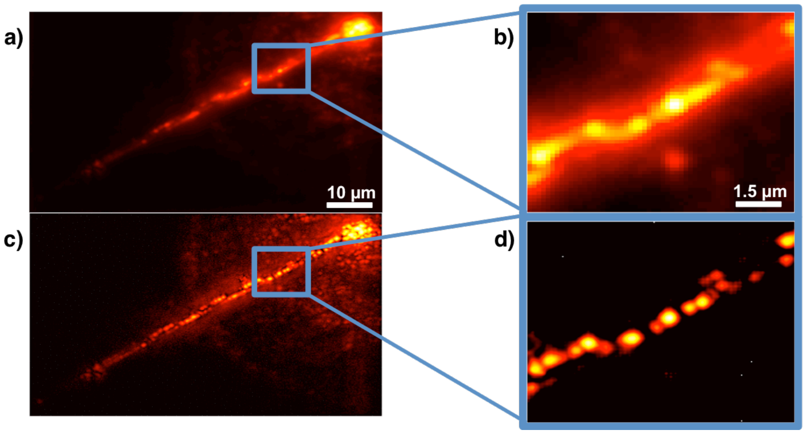

Fig. 6.5: Superresolution imaging of plasmonic near-field. (a) Average pixel intensity **(b)** Zoom-in to boxed area in (a). **(c)** Superresolved image of plasmonic near-field of AgNW using MOCA-COFIBINS. **(d)** Zoom-in to boxed area in (c).

These initial results are very exciting, but call for further investigations. We will need to: (1) characterize how fast this method converges. Due to SOFI's stochastic nature, it is important to understand when statistical significance is reached; (2) What is the maximum density of emitters that still provides reliable parameter extraction? (3) How well can SOFI-based MOCA-COFIBINS handle non-Gaussian PSFs? As with most superresolution techniques, this method currently assumes a Gaussian PSF. Unfortunately, emitters PSFs are not Gaussian due to the scattering distortion mentioned above.

References

1. Yonzon, C. R.; Jeoung, E.; Zou, S.; Schatz, G. C.; Mrksich, M.; Van Duyne, R. P., A Comparative Analysis of Localized and Propagating Surface Plasmon Resonance Sensors: The Binding of Concanavalin A to a Monosaccharide Functionalized Self-Assembled Monolayer. *Journal of the American Chemical Society* **2004,** *126* (39), 12669-12676.

2. Elghanian, R.; Storhoff, J. J.; Mucic, R. C.; Letsinger, R. L.; Mirkin, C. A., Selective Colorimetric Detection of Polynucleotides Based on the Distance-Dependent Optical Properties of Gold Nanoparticles. *Science* **1997,** *277* (5329), 1078-1081.

3. Kneipp, K.; Wang, Y.; Kneipp, H.; Perelman, L. T.; Itzkan, I.; Dasari, R. R.; Feld, M. S., Single Molecule Detection Using Surface-Enhanced Raman Scattering (SERS). *Physical Review Letters* **1997,** *78* (9), 1667-1670.

4. Das, A.; Zhao, J.; Schatz, G. C.; Sligar, S. G.; Van Duyne, R. P., Screening of Type I and II Drug Binding to Human Cytochrome P450-3A4 in Nanodiscs by Localized Surface Plasmon Resonance Spectroscopy. *Analytical Chemistry* **2009,** *81* (10), 3754-3759.

5. Tam, F.; Goodrich, G. P.; Johnson, B. R.; Halas, N. J., Plasmonic Enhancement of Molecular Fluorescence. *Nano Letters* **2007,** *7* (2), 496-501.

6. Kinkhabwala, A.; Yu, Z.; Fan, S.; Avlasevich, Y.; Mullen, K.; Moerner, W. E., Large single-molecule fluorescence enhancements produced by a bowtie nanoantenna. *Nat Photon* **2009,** *3* (11), 654-657.

7. Acuna, G. P.; Möller, F. M.; Holzmeister, P.; Beater, S.; Lalkens, B.; Tinnefeld, P., Fluorescence Enhancement at Docking Sites of DNA-Directed Self-Assembled Nanoantennas. *Science* **2012,** *338* (6106), 506-510.

8. Jackson, J. B.; Halas, N. J., Surface-enhanced Raman scattering on tunable plasmonic nanoparticle substrates. *Proceedings of the National Academy of Sciences* **2004,** *101* (52), 17930-17935.

9. Hu, M.; Ou, F. S.; Wu, W.; Naumov, I.; Li, X.; Bratkovsky, A. M.; Williams, R. S.; Li, Z., Gold Nanofingers for Molecule Trapping and Detection. *Journal of the American Chemical Society* **2010,** *132* (37), 12820-12822.

10. Qin, L.; Zou, S.; Xue, C.; Atkinson, A.; Schatz, G. C.; Mirkin, C. A., Designing, fabricating, and imaging Raman hot spots. *Proceedings of the National Academy of Sciences* **2006,** *103* (36), 13300-13303.

11. Nitzan, A.; Brus, L. E., Theoretical model for enhanced photochemistry on rough surfaces. *The Journal of Chemical Physics* **1981,** *75* (5), 2205-2214.

12. Barnes, W. L.; Dereux, A.; Ebbesen, T. W., Surface plasmon subwavelength optics. *Nature* **2003,** *424* (6950), 824-830.

13. Oulton, R. F.; Sorger, V. J.; Genov, D. A.; Pile, D. F. P.; Zhang, X., A hybrid plasmonic waveguide for subwavelength confinement and long-range propagation. *Nat Photon* **2008,** *2* (8), 496-500.

14. Steinberger, B.; Hohenau, A.; Ditlbacher, H.; Aussenegg, F. R.; Leitner, A.; Krenn, J. R., Dielectric stripes on gold as surface plasmon waveguides: Bends and directional couplers. *Applied Physics Letters* **2007,** *91* (8), 094104.

15. Engheta, N.; Salandrino, A.; Alù, A., Circuit Elements at Optical Frequencies: Nanoinductors, Nanocapacitors, and Nanoresistors. *Physical Review Letters* **2005,** *95* (9), 095504.

16. Guo, X.; Qiu, M.; Bao, J.; Wiley, B. J.; Yang, Q.; Zhang, X.; Ma, Y.; Yu, H.; Tong, L., Direct Coupling of Plasmonic and Photonic Nanowires for Hybrid Nanophotonic Components and Circuits. *Nano Letters* **2009,** *9* (12), 4515-4519.

17. Krasavin, A. V.; Randhawa, S.; Bouillard, J.-S.; Renger, J.; Quidant, R.; Zayats, A. V., Optically-programmable nonlinear photonic component for dielectric-loaded plasmonic circuitry. *Optics Express* **2011,** *19* (25), 25222-25229.

18. Maier, S. A., *Plasmonics: fundamentals and applications*. Springer Science & Business Media: 2007.

19. Wiley, B. J.; Chen, Y.; McLellan, J. M.; Xiong, Y.; Li, Z.-Y.; Ginger, D.; Xia, Y., Synthesis and optical properties of silver nanobars and nanorice. *Nano letters* **2007,** *7* (4), 1032-1036.

20. Wertz, E.; Isaacoff, B. P.; Flynn, J. D.; Biteen, J. S., Single-molecule super-resolution microscopy reveals how light couples to a plasmonic nanoantenna on the nanometer scale. *Nano letters* **2015,** *15* (4), 2662-2670.

21. Kittel, C., *Introduction to solid state physics*. Wiley: 2005.

22. Haes, A. J.; Haynes, C. L.; McFarland, A. D.; Schatz, G. C.; Van Duyne, R. P.; Zou, S., Plasmonic materials for surface-enhanced sensing and spectroscopy. *MRS bulletin* **2005,** *30* (5), 368-375.

23. Li, M.; Cushing, S. K.; Wu, N., Plasmon-enhanced optical sensors: a review. *Analyst* **2015,** *140* (2), 386-406.

24. Fu, B.; Flynn, J. D.; Isaacoff, B. P.; Rowland, D. J.; Biteen, J. S., Super-resolving the distance-dependent plasmon-enhanced fluorescence of single dye and fluorescent protein molecules. *The Journal of Physical Chemistry C* **2015,** *119* (33), 19350-19358.

25. BETZIG, E.; TRAUTMAN, J. K.; HARRIS, T. D.; WEINER, J. S.; KOSTELAK, R. L., Breaking the Diffraction Barrier: Optical Microscopy on a Nanometric Scale. *Science* **1991,** *251* (5000), 1468-1470.

26. Lewis, A.; Lieberman, K.; Ben-Ami, N.; Fish, G.; Khachatryan, E.; Ben-Ami, U.; Shalom, S., New design and imaging concepts in NSOM. *Ultramicroscopy* **1995,** *61* (1–4), 215-220.

27. Formanek, F.; De Wilde, Y.; Aigouy, L., Imaging subwavelength holes using an apertureless near-field scanning optical microscope. *Journal of Applied Physics* **2003,** *93* (12), 9548-9552.

28. Onishi, S.; Matsuishi, K.; Oi, J.; Harada, T.; Kusaba, M.; Hirosawa, K.; Kannari, F., Spatiotemporal control of femtosecond plasmon using plasmon response functions measured by near-field scanning optical microscopy (NSOM). *Optics Express* **2013,** *21* (22), 26631-26641.

29. Ye, Z.; Zhang, S.; Wang, Y.; Park, Y.-S.; Zentgraf, T.; Bartal, G.; Yin, X.; Zhang, X., Mapping the near-field dynamics in plasmon-induced transparency. *Physical Review B* **2012,** *86* (15), 155148.

30. Harris, C. M., Product review: shedding light on NSOM. *Analytical chemistry* **2003,** *75* (9), 223 A-228 A.

31. Kim, J.; Song, K.-B., Recent progress of nano-technology with NSOM. *Micron* **2007,** *38* (4), 409-426.

32. Zhang, S.; Xu, H., Optimizing substrate-mediated plasmon coupling toward high-performance plasmonic nanowire waveguides. *Acs Nano* **2012,** *6* (9), 8128-8135.

33. Ropp, C.; Cummins, Z.; Nah, S.; Fourkas, J. T.; Shapiro, B.; Waks, E., Nanoscale probing of image-dipole interactions in a metallic nanostructure. *Nat Commun* **2015,** *6*.

34. Yashunin, D.; Ilin, N.; Stepanov, A.; Smirnov, A., Two-photon luminescence imaging by scanning near-field optical microscopy for characterization of gold nanoparticles. *Journal of Physics D: Applied Physics* **2014,** *47* (30), 305102.

35. Bosman, M.; Keast, V. J.; Watanabe, M.; Maaroof, A. I.; Cortie, M. B., Mapping surface plasmons at the nanometre scale with an electron beam. *Nanotechnology* **2007,** *18* (16), 165505.

36. Nelayah, J.; Kociak, M.; Stephan, O.; Garcia de Abajo, F. J.; Tence, M.; Henrard, L.; Taverna, D.; Pastoriza-Santos, I.; Liz-Marzan, L. M.; Colliex, C., Mapping surface plasmons on a single metallic nanoparticle. *Nat Phys* **2007,** *3* (5), 348-353.

37. Douillard, L.; Charra, F.; Korczak, Z.; Bachelot, R.; Kostcheev, S.; Lerondel, G.; Adam, P.-M.; Royer, P., Short Range Plasmon Resonators Probed by Photoemission Electron Microscopy. *Nano Letters* **2008,** *8* (3), 935-940.

38. Vesseur, E. J. R.; de Waele, R.; Kuttge, M.; Polman, A., Direct Observation of Plasmonic Modes in Au Nanowires Using High-Resolution Cathodoluminescence Spectroscopy. *Nano Letters* **2007,** *7* (9), 2843-2846.

39. Solis, D.; Chang, W.-S.; Khanal, B. P.; Bao, K.; Nordlander, P.; Zubarev, E. R.; Link, S., Bleach-Imaged Plasmon Propagation (BlIPP) in Single Gold Nanowires. *Nano Letters* **2010,** *10* (9), 3482-3485.

40. Betzig, E., Nobel Lecture: Single molecules, cells, and super-resolution optics*. *Reviews of Modern Physics* **2015,** *87* (4), 1153-1168.

41. Moerner, W. E., Nobel Lecture: Single-molecule spectroscopy, imaging, and photocontrol: Foundations for super-resolution microscopy*. *Reviews of Modern Physics* **2015,** *87* (4), 1183-1212.

42. Hell, S. W., Nobel Lecture: Nanoscopy with freely propagating light*. *Reviews of Modern Physics* **2015,** *87* (4), 1169-1181.

43. Lin, H.; Centeno, S. P.; Su, L.; Kenens, B.; Rocha, S.; Sliwa, M.; Hofkens, J.; Uji-i, H., Mapping of Surface-Enhanced Fluorescence on Metal Nanoparticles using Super-Resolution Photoactivation Localization Microscopy. *ChemPhysChem* **2012,** *13* (4), 973-981.

44. Willets, K. A., Super-resolution imaging of interactions between molecules and plasmonic nanostructures. *Physical Chemistry Chemical Physics* **2013,** *15* (15), 5345-5354.

45. Walhorn, V.; Paskarbeit, J.; Frey, H. G.; Harder, A.; Anselmetti, D., Distance dependence of near-field fluorescence enhancement and quenching of single quantum dots. *Beilstein Journal of Nanotechnology* **2011,** *2*, 645-652.

46. Su, L.; Lu, G.; Kenens, B.; Rocha, S.; Fron, E.; Yuan, H.; Chen, C.; Van Dorpe, P.; Roeffaers, M. B. J.; Mizuno, H.; Hofkens, J.; Hutchison, J. A.; Uji-i, H., Visualization of molecular fluorescence point spread functions via remote excitation switching fluorescence microscopy. *Nat Commun* **2015,** *6*.

47. Su, L.; Yuan, H.; Lu, G.; Rocha, S.; Orrit, M.; Hofkens, J.; Uji-i, H., Super-resolution Localization and Defocused Fluorescence Microscopy on Resonantly Coupled Single-Molecule, Single-Nanorod Hybrids. *ACS Nano* **2016,** *10* (2), 2455-2466.

48. Hofer, F.; Schmidt, F.; Grogger, W.; Kothleitner, G. In *Fundamentals of electron energy-loss spectroscopy*, IOP Conference Series: Materials Science and Engineering, IOP Publishing: 2016; p 012007.

49. Bozhevolnyi, S. I. In *Plasmonic nano-guides and circuits*, Plasmonics and Metamaterials, Optical Society of America: 2008; p MWD3.

50. Knight, M. W.; King, N. S.; Liu, L.; Everitt, H. O.; Nordlander, P.; Halas, N. J., Aluminum for plasmonics. *ACS nano* **2013,** *8* (1), 834-840.

51. Chan, G. H.; Zhao, J.; Hicks, E. M.; Schatz, G. C.; Van Duyne, R. P., Plasmonic properties of copper nanoparticles fabricated by nanosphere lithography. *Nano Letters* **2007,** *7* (7), 1947-1952.

52. West, P. R.; Ishii, S.; Naik, G. V.; Emani, N. K.; Shalaev, V. M.; Boltasseva, A., Searching for better plasmonic materials. *Laser & Photonics Reviews* **2010,** *4* (6), 795-808.

53. Buonsanti, R.; Llordes, A.; Aloni, S.; Helms, B. A.; Milliron, D. J., Tunable infrared absorption and visible transparency of colloidal aluminum-doped zinc oxide nanocrystals. *Nano letters* **2011,** *11* (11), 4706-4710.

54. Lounis, S. D.; Runnerstrom, E. L.; Bergerud, A.; Nordlund, D.; Milliron, D. J., Influence of dopant distribution on the plasmonic properties of indium tin oxide nanocrystals. *Journal of the American Chemical Society* **2014,** *136* (19), 7110-7116.

55. Naik, G. V.; Shalaev, V. M.; Boltasseva, A., Alternative plasmonic materials: beyond gold and silver. *Advanced Materials* **2013,** *25* (24), 3264-3294.

56. Lounis, S. D.; Runnerstrom, E. L.; Llordés, A.; Milliron, D. J., Defect chemistry and plasmon physics of colloidal metal oxide nanocrystals. *The journal of physical chemistry letters* **2014,** *5* (9), 1564-1574.

57. Willets, K. A.; Van Duyne, R. P., Localized surface plasmon resonance spectroscopy and sensing. *Annu. Rev. Phys. Chem.* **2007,** *58*, 267-297.

58. Hao, E.; Schatz, G. C., Electromagnetic fields around silver nanoparticles and dimers. *The Journal of chemical physics* **2004,** *120* (1), 357-366.

59. Zuloaga, J.; Prodan, E.; Nordlander, P., Quantum description of the plasmon resonances of a nanoparticle dimer. *Nano letters* **2009,** *9* (2), 887-891.

60. Nordlander, P.; Le, F., Plasmonic structure and electromagnetic field enhancements in the metallic nanoparticle-film system. *Applied Physics B: Lasers and Optics* **2006,** *84* (1), 35-41.

61. Homola, J., Surface plasmon resonance sensors for detection of chemical and biological species. *Chemical reviews* **2008,** *108* (2), 462-493.

62. Kauranen, M.; Zayats, A. V., Nonlinear plasmonics. *Nature Photonics* **2012,** *6* (11), 737-748.

63. Tame, M. S.; McEnery, K.; Özdemir, S. K.; Lee, J.; Maier, S.; Kim, M., Quantum plasmonics. *arXiv preprint arXiv:1312.6806* **2013**.

64. Maier, S. A., *Plasmonics: Fundamentals and Applications*. 1 ed.; Springer US: 2007; p XXVI, 224.

65. Yee, K., Numerical solution of initial boundary value problems involving Maxwell's equations in isotropic media. *IEEE Transactions on antennas and propagation* **1966,** *14* (3), 302-307.

66. Ehrenberg, M., The Nobel Prize in Chemistry 2014 (Press Release). Stockholm: 2014.

67. Berro, A. J.; Berglund, A. J.; Carmichael, P. T.; Kim, J. S.; Liddle, J. A., Super-resolution optical measurement of nanoscale photoacid distribution in lithographic materials. *ACS nano* **2012,** *6* (11), 9496-9502.

68. Urban, B. E.; Dong, B.; Nguyen, T.-Q.; Backman, V.; Sun, C.; Zhang, H. F., Subsurface super-resolution imaging of unstained polymer nanostructures. *Scientific reports* **2016,** *6*.

69. Gramlich, M.; Bae, J.; Hayward, R.; Ross, J., Fluorescence imaging of nanoscale domains in polymer blends using stochastic optical reconstruction microscopy (STORM). *Optics express* **2014,** *22* (7), 8438-8450.

70. Bolinger, J. C.; Traub, M. C.; Adachi, T.; Barbara, P. F., Ultralong-range polaron-induced quenching of excitons in isolated conjugated polymers. *Science* **2011,** *331* (6017), 565-567.

71. Kisley, L.; Brunetti, R.; Tauzin, L. J.; Shuang, B.; Yi, X.; Kirkeminde, A. W.; Higgins, D. A.; Weiss, S.; Landes, C. F., Characterization of porous materials by fluorescence correlation spectroscopy super-resolution optical fluctuation imaging. *ACS nano* **2015,** *9* (9), 9158-9166.

72. Sambur, J. B.; Chen, T.-Y.; Choudhary, E.; Chen, G.; Nissen, E. J.; Thomas, E. M.; Zou, N.; Chen, P., Sub-particle reaction and photocurrent mapping to optimize catalyst-modified photoanodes. *Nature* **2016,** *530* (7588), 77-80.

73. Xu, W.; Shen, H.; Kim, Y. J.; Zhou, X.; Liu, G.; Park, J.; Chen, P., Single-molecule electrocatalysis by single-walled carbon nanotubes. *Nano letters* **2009,** *9* (12), 3968-3973.

74. Chen, P.; Zhou, X.; Andoy, N. M.; Han, K.-S.; Choudhary, E.; Zou, N.; Chen, G.; Shen, H., Spatiotemporal catalytic dynamics within single nanocatalysts revealed by single-molecule microscopy. *Chemical Society Reviews* **2014,** *43* (4), 1107-1117.

75. Mayer, K. M.; Hafner, J. H., Localized surface plasmon resonance sensors. *Chemical reviews* **2011,** *111* (6), 3828-3857.

76. Anker, J. N.; Hall, W. P.; Lyandres, O.; Shah, N. C.; Zhao, J.; Van Duyne, R. P., Biosensing with plasmonic nanosensors. *Nature materials* **2008,** *7* (6), 442-453.

77. Huang, B.; Bates, M.; Zhuang, X., Super-resolution fluorescence microscopy. *Annual review of biochemistry* **2009,** *78*, 993-1016.

78. Schermelleh, L.; Heintzmann, R.; Leonhardt, H., A guide to super-resolution fluorescence microscopy. *The Journal of cell biology* **2010,** *190* (2), 165-175.

79. Sahl, S. J.; Hell, S. W.; Jakobs, S., Fluorescence nanoscopy in cell biology. *Nature reviews. Molecular cell biology* **2017**.

80. Hell, S. W., Far-field optical nanoscopy. *science* **2007,** *316* (5828), 1153-1158.

81. Patterson, G.; Davidson, M.; Manley, S.; Lippincott-Schwartz, J., Superresolution imaging using single-molecule localization. *Annual review of physical chemistry* **2010,** *61*, 345-367.

82. Betzig, E.; Lewis, A.; Harootunian, A.; Isaacson, M.; Kratschmer, E., Near field scanning optical microscopy (NSOM): development and biophysical applications. *Biophysical Journal* **1986,** *49* (1), 269-279.

83. Willig, K. I.; Rizzoli, S. O.; Westphal, V.; Jahn, R.; Hell, S. W., STED microscopy reveals that synaptotagmin remains clustered after synaptic vesicle exocytosis. *Nature* **2006,** *440* (7086), 935.

84. Lereu, A.; Passian, A.; Dumas, P., Near field optical microscopy: a brief review. *International Journal of Nanotechnology* **2012,** *9* (3-7), 488-501.

85. Leung, B. O.; Chou, K. C., Review of super-resolution fluorescence microscopy for biology. *Applied spectroscopy* **2011,** *65* (9), 967-980.

86. Rust, M. J.; Bates, M.; Zhuang, X., Sub-diffraction-limit imaging by stochastic optical reconstruction microscopy (STORM). *Nature methods* **2006,** *3* (10), 793-796.

87. Betzig, E.; Patterson, G. H.; Sougrat, R.; Lindwasser, O. W.; Olenych, S.; Bonifacino, J. S.; Davidson, M. W.; Lippincott-Schwartz, J.; Hess, H. F., Imaging intracellular fluorescent proteins at nanometer resolution. *Science* **2006,** *313* (5793), 1642-1645.

88. Shegai, T.; Li, Z.; Dadosh, T.; Zhang, Z.; Xu, H.; Haran, G., Managing light polarization via plasmon–molecule interactions within an asymmetric metal nanoparticle trimer. *Proceedings of the National Academy of Sciences* **2008,** *105* (43), 16448-16453.

89. Su, L.; Lu, G.; Kenens, B.; Rocha, S.; Fron, E.; Yuan, H.; Chen, C.; Van Dorpe, P.; Roeffaers, M. B.; Mizuno, H., Visualization of molecular fluorescence point spread functions via remote excitation switching fluorescence microscopy. *Nature communications* **2015,** *6.*

90. Chhabra, R.; Sharma, J.; Wang, H.; Zou, S.; Lin, S.; Yan, H.; Lindsay, S.; Liu, Y., Distance-dependent interactions between gold nanoparticles and fluorescent molecules with DNA as tunable spacers. *Nanotechnology* **2009,** *20* (48), 485201.

91. Blythe, K. L.; Mayer, K. M.; Weber, M. L.; Willets, K. A., Ground state depletion microscopy for imaging interactions between gold nanowires and fluorophore-labeled ligands. *Physical Chemistry Chemical Physics* **2013,** *15* (12), 4136-4145.

92. Darvill, D.; Centeno, A.; Xie, F., Plasmonic fluorescence enhancement by metal nanostructures: shaping the future of bionanotechnology. *Physical Chemistry Chemical Physics* **2013,** *15* (38), 15709-15726.

93. Kinkhabwala, A.; Yu, Z.; Fan, S.; Avlasevich, Y.; Müllen, K.; Moerner, W., Large single-molecule fluorescence enhancements produced by a bowtie nanoantenna. *Nature Photonics* **2009,** *3* (11), 654-657.

94. Bakker, R. M.; Drachev, V. P.; Liu, Z.; Yuan, H.-K.; Pedersen, R. H.; Boltasseva, A.; Chen, J.; Irudayaraj, J.; Kildishev, A. V.; Shalaev, V. M., Nanoantenna array-induced fluorescence enhancement and reduced lifetimes. *New Journal of Physics* **2008,** *10* (12), 125022.

95. Purcell, E. M.; Torrey, H. C.; Pound, R. V., Resonance absorption by nuclear magnetic moments in a solid. *Physical review* **1946,** *69* (1-2), 37.

96. Anger, P.; Bharadwaj, P.; Novotny, L., Enhancement and quenching of single-molecule fluorescence. *Physical review letters* **2006,** *96* (11), 113002.

97. Gutmann, J.; Zappe, H.; Goldschmidt, J. C., Quantitative modeling of fluorescent emission in photonic crystals. *Physical Review B* **2013,** *88* (20), 205118.

98. Giannini, V.; Fernández-Domínguez, A. I.; Heck, S. C.; Maier, S. A., Plasmonic nanoantennas: fundamentals and their use in controlling the radiative properties of nanoemitters. *Chemical reviews* **2011,** *111* (6), 3888-3912.

99. Muskens, O.; Giannini, V.; Sanchez-Gil, J.; Gomez Rivas, J., Strong enhancement of the radiative decay rate of emitters by single plasmonic nanoantennas. *Nano letters* **2007,** *7* (9), 2871-2875.

100. Matsubara, K.; Kawata, S.; Minami, S., Optical chemical sensor based on surface plasmon measurement. *Applied Optics* **1988,** *27* (6), 1160-1163.

101. Khlebtsov, N. G.; Dykman, L. A., Optical properties and biomedical applications of plasmonic nanoparticles. *J. Quant. Spectrosc. Radiat. Transf.* **2010,** *111* (1), 1-35.

102. Chen, J.; Glaus, C.; Laforest, R.; Zhang, Q.; Yang, M.; Gidding, M.; Welch, M. J.; Xia, Y., Gold Nanocages as Photothermal Transducers for Cancer Treatment. *Small* **2010,** *6* (7), 811-817.

103. Hühn, D.; Govorov, A.; Gil, P. R.; Parak, W. J., Photostimulated Au Nanoheaters in Polymer and Biological Media: Characterization of Mechanical Destruction and Boiling. *Advanced Functional Materials* **2012,** *22* (2), 294-303.

104. Richardson, H. H.; Carlson, M. T.; Tandler, P. J.; Hernandez, P.; Govorov, A. O., Experimental and Theoretical Studies of Light-to-Heat Conversion and Collective Heating Effects in Metal Nanoparticle Solutions. *Nano Letters* **2009,** *9* (3), 1139-1146.

105. Garcia, G.; Buonsanti, R.; Runnerstrom, E. L.; Mendelsberg, R. J.; Llordes, A.; Anders, A.; Richardson, T. J.; Milliron, D. J., Dynamically Modulating the Surface Plasmon Resonance of Doped Semiconductor Nanocrystals. *Nano Letters* **2011,** *11* (10), 4415-4420.

106. Atwater, H. A.; Polman, A., Plasmonics for improved photovoltaic devices. *Nature materials* **2010,** *9* (3), 205-213.

107. Chang, D. E.; Sørensen, A. S.; Demler, E. A.; Lukin, M. D., A single-photon transistor using nanoscale surface plasmons. *Nature Physics* **2007,** *3* (11), 807-812.

108. Neuhauser, D.; Lopata, K., Molecular nanopolaritonics: Cross manipulation of near-field plasmons and molecules. I. Theory and application to junction control. *The Journal of chemical physics* **2007,** *127*, 154715.

109. Biteen, J. S.; Lewis, N. S.; Atwater, H. A.; Mertens, H.; Polman, A., Spectral tuning of plasmon-enhanced silicon quantum dot luminescence. *Applied physics letters* **2006,** *88* (13), 131109-131109-3.

110. Halas, N., Playing with plasmons: Tuning the optical resonant properties of metallic nanoshells. *Mrs Bulletin* **2005,** *30* (05), 362-367.

111. Yelk, J.; Sukharev, M.; Seideman, T., Optimal design of nanoplasmonic materials using genetic algorithms as a multi-parameter optimization tool. *arXiv preprint arXiv:0802.2899* **2008**.

112. Esteban, R.; Borisov, A. G.; Nordlander, P.; Aizpurua, J., Bridging quantum and classical plasmonics with a quantum-corrected model. *Nature Communications* **2012,** *3*, 825.

113. Halas, N. J.; Lal, S.; Chang, W.-S.; Link, S.; Nordlander, P., Plasmons in Strongly Coupled Metallic Nanostructures. *Chemical Reviews* **2011,** *111* (6), 3913-3961.

114. Morton, S. M.; Silverstein, D. W.; Jensen, L., Theoretical Studies of Plasmonics using Electronic Structure Methods. *Chemical Reviews* **2011,** *111* (6), 3962-3994.

115. McMahon, J.; Henry, A.-I.; Wustholz, K.; Natan, M.; Freeman, R.; Van Duyne, R.; Schatz, G., Gold nanoparticle dimer plasmonics: finite element method calculations of the electromagnetic enhancement to surface-enhanced Raman spectroscopy. *Analytical and Bioanalytical Chemistry* **2009,** *394* (7), 1819-1825.

116. Arntsen, C.; Lopata, K.; Wall, M. R.; Bartell, L.; Neuhauser, D., Modeling molecular effects on plasmon transport: Silver nanoparticles with tartrazine. *The Journal of chemical physics* **2011,** *134* (8), 084101-084101-7.

117. Lopata, K.; Neuhauser, D., Nonlinear nanopolaritonics: Finite-difference time-domain Maxwell‚ÄìSchr√∂dinger simulation of molecule-assisted plasmon transfer. *The Journal of chemical physics* **2009,** *131*, 014701.

118. Coomar, A.; Arntsen, C.; Lopata, K. A.; Pistinner, S.; Neuhauser, D., Near-field: A finite-difference time-dependent method for simulation of electrodynamics on small scales. *The Journal of chemical physics* **2011,** *135*, 084121.

119. Lopata, K.; Neuhauser, D.; Baer, R., Curve crossing and negative refraction in simulations of near-field coupled metallic nanoparticle arrays. *The Journal of chemical physics* **2007,** *127*, 154714.

120. Nordlander, P.; Oubre, C.; Prodan, E.; Li, K.; Stockman, M. I., Plasmon Hybridization in Nanoparticle Dimers. *Nano Letters* **2004,** *4* (5), 899-903.

121. Yang, S.-C.; Kobori, H.; He, C.-L.; Lin, M.-H.; Chen, H.-Y.; Li, C.; Kanehara, M.; Teranishi, T.; Gwo, S., Plasmon Hybridization in Individual Gold Nanocrystal Dimers: Direct Observation of Bright and Dark Modes. *Nano Letters* **2010,** *10* (2), 632-637.

122. Funston, A. M.; Novo, C.; Davis, T. J.; Mulvaney, P., Plasmon coupling of gold nanorods at short distances and in different geometries. *Nano Lett* **2009,** *9* (4), 1651-1658.

123. Rong, G.; Wang, H.; Skewis, L. R.; Reinhard, B. M., Resolving sub-diffraction limit encounters in nanoparticle tracking using live cell plasmon coupling microscopy. *Nano Letters* **2008,** *8* (10), 3386-3393.

124. Li, S.; Gao, Y.; Neuhauser, D., Near-field for electrodynamics at sub-wavelength scales: Generalizing to an arbitrary number of dielectrics. *The Journal of chemical physics* **2012,** *136*, 234104.

125. Taflov, A.; Hagness, S., *Computational Electrodynamics: The Finite-Difference Time-Domain Method*. 2nd ed.; Artech House: Boston, MA, 2000.

126. Solis, D.; Paul, A.; Olson, J.; Slaughter, L. S.; Swanglap, P.; Chang, W.-S.; Link, S., Turning the Corner: Efficient Energy Transfer in Bent Plasmonic Nanoparticle Chain Waveguides. *Nano Letters* **2013,** *13* (10), 4779-4784.

127. Paul, A.; Zhen, Y.-R.; Wang, Y.; Chang, W.-S.; Xia, Y.; Nordlander, P.; Link, S., Dye-Assisted Gain of Strongly Confined Surface Plasmon Polaritons in Silver Nanowires. *Nano Letters* **2014,** *14* (6), 3628-3633.

128. Christopher, P.; Xin, H.; Linic, S., Visible-light-enhanced catalytic oxidation reactions on plasmonic silver nanostructures. *Nat Chem* **2011,** *3* (6), 467-472.

129. Nauert, S.; Paul, A.; Zhen, Y.-R.; Solis, D.; Vigderman, L.; Chang, W.-S.; Zubarev, E. R.; Nordlander, P.; Link, S., Influence of Cross Sectional Geometry on Surface Plasmon Polariton Propagation in Gold Nanowires. *ACS Nano* **2014,** *8* (1), 572-580.

130. Nirmal, M.; Dabbousi, B. O.; Bawendi, M. G.; Macklin, J. J.; Trautman, J. K.; Harris, T. D.; Brus, L. E., Fluorescence intermittency in single cadmium selenide nanocrystals. *Nature* **1996,** *383* (6603), 802-804.

131. Kuno, M.; Fromm, D. P.; Hamann, H. F.; Gallagher, A.; Nesbitt, D. J., Nonexponential “blinking” kinetics of single CdSe quantum dots: A universal power law behavior. *The Journal of Chemical Physics* **2000,** *112* (7), 3117-3120.

132. Kuno, M.; Fromm, D. P.; Hamann, H. F.; Gallagher, A.; Nesbitt, D. J., “On”/“off” fluorescence intermittency of single semiconductor quantum dots. *The Journal of Chemical Physics* **2001,** *115* (2), 1028-1040.

133. Shimizu, K. T.; Neuhauser, R. G.; Leatherdale, C. A.; Empedocles, S. A.; Woo, W. K.; Bawendi, M. G., Blinking statistics in single semiconductor nanocrystal quantum dots. *Physical Review B* **2001,** *63* (20), 205316.

134. Bharadwaj, P.; Novotny, L., Robustness of Quantum Dot Power-Law Blinking. *Nano Letters* **2011,** *11* (5), 2137-2141.

135. Mertens, H.; Biteen, J. S.; Atwater, H. A.; Polman, A., Polarization-Selective Plasmon-Enhanced Silicon Quantum-Dot Luminescence. *Nano Letters* **2006,** *6* (11), 2622-2625.

136. Cheng, M.-T.; Liu, S.-D.; Wang, Q.-Q., Modulating emission polarization of semiconductor quantum dots through surface plasmon of metal nanorod. *Applied Physics Letters* **2008,** *92* (16), 162107.

137. Tang, J.; Marcus, R. A., Mechanisms of fluorescence blinking in semiconductor nanocrystal quantum dots. *The Journal of Chemical Physics* **2005,** *123* (5), 054704.

138. Frantsuzov, P.; Kuno, M.; Janko, B.; Marcus, R. A., Universal emission intermittency in quantum dots, nanorods and nanowires. *Nat Phys* **2008,** *4* (5), 519-522.

139. Crouch, C. H.; Sauter, O.; Wu, X.; Purcell, R.; Querner, C.; Drndic, M.; Pelton, M., Facts and Artifacts in the Blinking Statistics of Semiconductor Nanocrystals. *Nano Letters* **2010,** *10* (5), 1692-1698.

140. Park, Y.-S.; Bae, W. K.; Padilha, L. A.; Pietryga, J. M.; Klimov, V. I., Effect of the Core/Shell Interface on Auger Recombination Evaluated by Single-Quantum-Dot Spectroscopy. *Nano Letters* **2014,** *14* (2), 396-402.

141. Bae, W. K.; Park, Y.-S.; Lim, J.; Lee, D.; Padilha, L. A.; McDaniel, H.; Robel, I.; Lee, C.; Pietryga, J. M.; Klimov, V. I., Controlling the influence of Auger recombination on the performance of quantum-dot light-emitting diodes. *Nat Commun* **2013,** *4*.

142. Peterson, J. J.; Nesbitt, D. J., Modified Power Law Behavior in Quantum Dot Blinking: A Novel Role for Biexcitons and Auger Ionization. *Nano Letters* **2008,** *9* (1), 338-345.

143. Tyagi, P.; Kambhampati, P., False multiple exciton recombination and multiple exciton generation signals in semiconductor quantum dots arise from surface charge trapping. *The Journal of Chemical Physics* **2011,** *134* (9), 094706.

144. Park, S.-J.; Link, S.; Miller, W. L.; Gesquiere, A.; Barbara, P. F., Effect of electric field on the photoluminescence intensity of single CdSe nanocrystals. *Chemical Physics* **2007,** *341* (1–3), 169-174.

145. Houel, J.; Doan, Q. T.; Cajgfinger, T.; Ledoux, G.; Amans, D.; Aubret, A.; Dominjon, A.; Ferriol, S.; Barbier, R.; Nasilowski, M.; Lhuillier, E.; Dubertret, B.; Dujardin, C.; Kulzer, F., Autocorrelation Analysis for the Unbiased Determination of Power-Law Exponents in Single-Quantum-Dot Blinking. *ACS Nano* **2015,** *9* (1), 886-893.

146. Pelton, M.; Smith, G.; Scherer, N. F.; Marcus, R. A., Evidence for a diffusion-controlled mechanism for fluorescence blinking of colloidal quantum dots. *Proceedings of the National Academy of Sciences* **2007,** *104* (36), 14249-14254.

147. Verberk, R.; Orrit, M., Photon statistics in the fluorescence of single molecules and nanocrystals: Correlation functions versus distributions of on- and off-times. *The Journal of Chemical Physics* **2003,** *119* (4), 2214-2222.

148. Lee, D.-H.; Yuan, C.-T.; Tachiya, M.; Tang, J., Influence of bin time and excitation intensity on fluorescence lifetime distribution and blinking statistics of single quantum dots. *Applied Physics Letters* **2009,** *95* (16), 163101.

149. Johnson, P. B.; Christy, R. W., Optical Constants of the Noble Metals. *Physical Review B* **1972,** *6* (12), 4370-4379.

150. Coomar, A.; Arntsen, C.; Lopata, K. A.; Pistinner, S.; Neuhauser, D., Near-field: A finite-difference time-dependent method for simulation of electrodynamics on small scales. *The Journal of Chemical Physics* **2011,** *135* (8), 084121.

151. Brown, J.; Jull, E. V., The prediction of aerial radiation patterns from near-field measurements. *Proceedings of the IEE - Part B: Electronic and Communication Engineering* **1961,** *108* (42), 635-644.

152. Sun, Y.; Xia, Y., Large-Scale Synthesis of Uniform Silver Nanowires Through a Soft, Self-Seeding, Polyol Process. *Advanced Materials* **2002,** *14* (11), 833-837.

153. Thompson, R. E.; Larson, D. R.; Webb, W. W., Precise nanometer localization analysis for individual fluorescent probes. *Biophysical Journal* **2002,** *82* (5), 2775-2783.

154. Mazziotta, M. N., Electron–hole pair creation energy and Fano factor temperature dependence in silicon. *Nuclear Instruments and Methods in Physics Research Section A: Accelerators, Spectrometers, Detectors and Associated Equipment* **2008,** *584* (2–3), 436-439.

155. Stranahan, S. M.; Willets, K. A., Super-resolution Optical Imaging of Single-Molecule SERS Hot Spots. *Nano Letters* **2010,** *10* (9), 3777-3784.

156. Blythe, K. L.; Titus, E. J.; Willets, K. A., Comparing the Accuracy of Reconstructed Image Size in Super-Resolution Imaging of Fluorophore-Labeled Gold Nanorods Using Different Fit Models. *The Journal of Physical Chemistry C* **2015,** *119* (33), 19333-19343.

157. Tighineanu, P.; Andersen, M. L.; Sørensen, A. S.; Stobbe, S.; Lodahl, P., Probing Electric and Magnetic Vacuum Fluctuations with Quantum Dots. *Physical Review Letters* **2014,** *113* (4), 043601.

158. Galland, C.; Ghosh, Y.; Steinbrück, A.; Hollingsworth, J. A.; Htoon, H.; Klimov, V. I., Lifetime blinking in nonblinking nanocrystal quantum dots. *Nat Commun* **2012,** *3*, 908.

159. Galland, C.; Ghosh, Y.; Steinbruck, A.; Sykora, M.; Hollingsworth, J. A.; Klimov, V. I.; Htoon, H., Two types of luminescence blinking revealed by spectroelectrochemistry of single quantum dots. *Nature* **2011,** *479* (7372), 203-207.

160. Mahler, B.; Spinicelli, P.; Buil, S.; Quelin, X.; Hermier, J.-P.; Dubertret, B., Towards non-blinking colloidal quantum dots. *Nat Mater* **2008,** *7* (8), 659-664.

161. Bakulin, A. A.; Neutzner, S.; Bakker, H. J.; Ottaviani, L.; Barakel, D.; Chen, Z., Charge Trapping Dynamics in PbS Colloidal Quantum Dot Photovoltaic Devices. *ACS Nano* **2013,** *7* (10), 8771-8779.

162. Dertinger, T.; Colyer, R.; Iyer, G.; Weiss, S.; Enderlein, J., Fast, background-free, 3D super-resolution optical fluctuation imaging (SOFI). *Proceedings of the National Academy of Sciences* **2009,** *106* (52), 22287-22292.

163. Dertinger, T.; Colyer, R.; Vogel, R.; Enderlein, J.; Weiss, S., Achieving increased resolution and more pixels with Superresolution Optical Fluctuation Imaging (SOFI). *Optics Express* **2010,** *18* (18), 18875-18885.

164. Geissbuehler, S.; Bocchio, N.; Dellagiacoma, C.; Berclaz, C.; Leutenegger, M.; Lasser, T., Mapping molecular statistics with balanced super-resolution optical fluctuation imaging (bSOFI). *Optical Nanoscopy* **2012,** *1* (1), 4.

165. Margolin, G.; Barkai, E., Aging correlation functions for blinking nanocrystals, and other on–off stochastic processes. *The Journal of Chemical Physics* **2004,** *121* (3), 1566-1577.

166. Wang, S.; Querner, C.; Emmons, T.; Drndic, M.; Crouch, C. H., Fluorescence Blinking Statistics from CdSe Core and Core/Shell Nanorods. *The Journal of Physical Chemistry B* **2006,** *110* (46), 23221-23227.

167. Boutelle, R. C.; Neuhauser, D.; Weiss, S., Far-Field Super-resolution Detection of Plasmonic Near-Fields. *ACS nano* **2016,** *10* (8), 7955-7962.